FABRICATION OF INTERDIGITATED BACK-CONTACT (IBC) SOLAR CELLS WITH SCREEN-PRINTED BORON DOPED EMITTERS

A THESIS SUBMITTED TO
THE GRADUATE SCHOOL OF NATURAL AND APPLIED SCIENCES
OF
MIDDLE EAST TECHNICAL UNIVERSITY

BY
ATEŞCAN ALİEFENDİOĞLU

IN PARTIAL FULFILLMENT OF THE REQUIREMENTS
FOR
THE DEGREE OF MASTER OF SCIENCE
IN
DEPARTMENT OF PHYSICS

JANUARY 2020

Approval of the thesis:

FABRICATION OF INTERDIGITATED BACK-CONTACT (IBC) SOLAR CELLS WITH SCREEN-PRINTED BORON DOPED EMITTERS

submitted by **ATEŞCAN ALİEFENDİOĞLU** in partial fulfilment of the requirements for the degree of **Master of Science in Department of Physics, Middle East Technical University** by,

Prof. Dr Halil Kalıpçılar
Dean, Graduate School of **Natural and Applied Sciences** _____

Prof. Dr Altuğ Özpineci
Head of Department, **Physics** _____

Prof. Dr Raşit Turan
Supervisor, **Department of Physics, METU** _____

Examining Committee Members:

Prof. Dr Çiğdem Erçelebi
Department of Physics, METU _____

Prof. Dr Raşit Turan
Department of Physics, METU _____

Prof. Dr Mehmet Parlak
Department of Physics, METU _____

Prof. Dr H. Emrah Ünalan
Dept. of Metal and Mat. Eng, METU _____

Assist. Prof. Dr Gülsen Baytemir
Department of EE Eng., Maltepe University _____

Date: 17.01.2020

I hereby declare that all information in this document has been obtained and presented in accordance with academic rules and ethical conduct. I also declare that, as required by these rules and conduct, I have fully cited and referenced all material and results that are not original to this work.

Name, Surname: Ateşcan ALİEFENDİOĞLU

Signature:

ABSTRACT

FABRICATION OF INTERDIGITATED BACK-CONTACT (IBC) SOLAR CELLS WITH SCREEN-PRINTED BORON DOPED EMITTERS

Aliefendioğlu, Ateşcan
Master of Science, Physics
Supervisor: Prof. Dr Raşit Turan

January 2020, 100 Pages

Interdigitated back-contact (IBC) solar cells with their unique structure, having both n and p doped regions as well all as contacts at the rear side, have the potential to achieve high-efficiency values. The record efficiency value at industrial scale have reached 25.2% for mono-crystalline silicon. This thesis focuses on the development of IBC cell structure which is one of the best performing cell structures. The scope of this thesis requires the full understanding of controlling the boron doping on an n-type wafer for decent process optimisation using Boron doping paste. The thesis also aims for the study of the necessary characterisation techniques, i.e. sheet resistance measurements, and electrochemical capacitance-voltage (ECV) profiling. Corresponding cell fabrication is based on screen-printing of Boron doping paste, annealing, and following metallisation steps. The bifacial structure is also demonstrated as a secondary proof-of-concept. The produced cells have been characterised and analysed with 8.70% efficiency on IBC and 7.43% efficiency on bifacial structures.

Keywords: Boron Doping Optimisation, Interdigitated Back-Contact (IBC), Bifacial, Doping and Cell Characterisation.

ÖZ

SERİGRAFİ İLE BOR KATKILANMIŞ ARKA KONTAK ARKA EKLEMLİ (IBC) GÜNEŞ HÜCRESI ÜRETİMİ

Aliefendioğlu, Ateşcan
Yüksek Lisans, Fizik
Tez Danışmanı: Prof. Dr. Raşit TURAN

Ocak 2020, 100 Sayfa

Arka kontak arka eklemli (IBC) güneş hücrelerinin, n ve p katkılı bölgeleri ve bütün bağlantılarının arka yüzeyde olması nedeniyle, yüksek verim potansiyeli olan hücre yapılarıdır. Bu konudaki rekor verim değeri endüstriyel boyutlarda tek kristal yapılı silisyum hücrelerde %25,2 seviyesine ulaşmıştır. Bu tezin odak noktası yüksek etkinlikli güneş hücrelerinin bir türü olarak görülen IBC tipi güneş hücrelerinin geliştirilmesidir. Çalışmalar kapsamında n-tipi Silisyum (Si) dilimlerin ekran baskı yöntemi ile Bor (B) içerikli pasta ile katkılanması hedeflenmektedir. Bu tez ayrıca gerekli olan çözümleme yöntemlerinin, yüzey direnci ve katkılama eğiliminin, ölçüm ve çözümlemesini de hedeflemektedir. İlgili hücre üretimi ekran baskı ile Bor pastası basımı, tavlama ve takiben metalizasyon adımlarından meydana gelmektedir. İkincil bir teorik kanıtlama amacıyla çift taraflı örnekler de üretilmiştir. Üretilen IBC ve çift yüzlü örneklerin ölçümleri ve çözümlemeleri yapılmış, IBC hücrelerde %8.70 ve çift taraflı örneklerde %7.43 verim elde edilmiştir.

Anahtar Kelimeler: Bor Katkılama İyileştirmesi, Arka kontak arka eklemli (IBC), Çift Taraflı, Katkılama ve Hücre Ölçüm ve Çözümlemesi.

To my dearest Grandmother, and my family…

ACKNOWLEDGEMENTS

I would like to thank my mentor Prof. Dr Raşit TURAN for two main things among many. First, I would like to thank him for accepting me to his GÜNAM family. And secondly, I would like to thank him for introducing me to one of the most dedicated people I have ever met. E. Hande ÇİFTPINAR is the most dedicated, caring and friendly person I have the chance to meet. It is an absolute delight to work with her. I am forever grateful for her unending support and patience with me. I am very lucky to call her my friend even though she might rupture my eardrums with her 90-dB sneeze. Thank you for your amazing friendship.

I will always remember how Ergi DÖNERÇARK messed with Hande about transferring me to his team when I start my doctorate studies. I would just sit back, say nothing and watch things unfold. His sharp wit is something to admire for. I also would like to thank him for his guidance and PL measurements. Salar HABİBPUR SEDANİ is such a person that whenever you need it, he would give you his undivided attention. He would take his time and way to come to your aid.

I would like to thank Gamze KÖKBUDAK, Dr Bülent ARIKAN and Dr Makbule TERLEMEZOĞLU for training me for various measurement and analysis tools. Without their proper training, some crucial parts of this thesis would not be possible. I also would like to thank Samet ÖZDEMİR helping me with cell processes so that I could spend more time on my thesis.

Along the way close to the end I have met Dr H. Serra ALTINOLUK. Never in my life have I met with such a positive person. She is an absolute delight to talk to and her humour is unparalleled. Thank you for being a friend.

Although Dr Gülsen BAYTEMİR and I became friends recently she is one of those people that adds beauty to your life. I also would like to congratulate her new position.

Throughout my undergraduate and graduate studies, Gülşen ÖZDEMİR PARLAK was and still is the first person I would go and ask for help. With her guidance, patience and care complicated things would become mere nuances. I will always cherish the fun and crazy talks Buket GÖKBAKAN and I had. Thank you both for making things easier and at times bearable.

A huge thanks go to my friends; Selen YÜKSEL, Cansu EMİR and Hazal DOĞAROĞLU for listening to me, giving me suggestions and helping me with my shenanigans. I also would like to thank Tuğba HACIEFENDİOĞLU, Özge DEMİRTAŞ, Merve DEMİR and Fırat İDİKUT for their delightful friendship.

Finally, I would like to give the biggest thanks to my parents. Without their everlasting support, love and faith in me, none of this would be even possible.

I acknowledge the financial support made available to me during my thesis work from the Scientific and Technological Research Council of Turkey (TÜBİTAK) with the grant 217M203.

Thank you

TABLE OF CONTENTS

LIST OF TABLES

TABLES

LIST OF FIGURES

FIGURES

LIST OF ABBREVIATIONS

ABBREVIATIONS

4PP	Four Point Probe
AM	Air Mass
APCVD	Atmospheric Pressure Chemical Vapour Deposition
ARC	Anti-Reflective Coating
BSE	Back-Scattered Electron
BSG	Boron Silicate Glass
CIGSS	Copper Indium Gallium Selenide Sulphide
CVD	Chemical Vapour Deposition
DC	Direct Current
ECV	Electrochemical Capacitance-Voltage
EDX	Energy-Dispersive X-ray
EQE	External Quantum Efficiency
EWT	Emitter Wrap Through
FFE	Front Floating Emitter
FSF	Front Surface Field
FT	Fire-Through
HIT	Heterojunction with Intrinsic Thin layer
IBC	Interdigitated Back Contact
IPA	Isopropyl Alcohol
IQE	Internal Quantum Efficiency

J-V	Current Density-Voltage
LED	Light Emitting Diode
LPCVD	Low-Pressure Chemical Vapour Deposition
MOCVD	Metal-Organic Chemical Vapour Deposition
MWT	Metal Wrap Through
PECVD	Plasma Enhanced Chemical Vapour Deposition
PERC	Passivated Emitter and Rear Contact/Cell
PERL	Passivated Emitter and Rear Locally diffused
PERT	Passivated Emitter and Rear Totally diffused
PL	Photoluminescence
PSG	Phosphorous Silicate Glass
R/T	Reflection/Transmission
RCA	Radio Corporation of America
SDE	Saw-Damage Etched
SE	Secondary Electron
SEM	Scanning Electron Microscopy
SIMS	Secondary Ion Mass Spectroscopy
SQ	Shockley-Queisser
SRH	Shockley-Read-Hall
TCO	Transparent Conductive Oxide
THE	Thermodynamic Heat Engine
TLM	Transfer Length Method
TMAH	Tetramethylammonium Hydroxide

LIST OF SYMBOLS

SYMBOLS

A	Area
D_n	Einstein Coefficient
E	Energy
E_C	Band-Edge Energy of the Conduction Band
E_F	Fermi Energy
E_g	Bandgap
E_V	Band-Edge Energy of the Valence Band
$\vec{E}$	Applied Electrical Field
FF	Fill Factor
G	Illumination Power
iV_{oc}	Implied Open-Circuit Voltage
J	Current
J_{pm}	Maximum Power Current Density
J_{sc}	Short-Circuit Current Density
k	Boltzmann Constant
n	Number of Free Electrons in the Conduction Band
$n_{1,2}$	Diode ideality factor
N_C	Effective Density of States of Electrons in the Conduction Band
N_V	Effective Density of States of Holes in the Valence Band
p	Number of Holes in the Valence Band

P_{max}	Maximum Power
R	Resistance
s	Probe Separation
T	Absolute Temperature
V_{oc}	Open-Circuit Voltage
V_{pm}	Maximum Power Voltage
α	Fitting Constant
β	Fitting Constant
η	Efficiency
θ	Angle
λ	Wavelength
μ	Mobility
σ	Conductivity
φ	Fraction

CHAPTER 1

INTRODUCTION

"One thing I feel sure of… is that the human race must finally utilise direct sun power or revert to barbarism."

- **Frank Shuman (1862-1918)**

1.1 Basics of Photovoltaics

1.1.1 The Use of Solar Energy Through History

The Sun is the one and only energy source of our planet. Throughout history, humankind used its energy to live and to survive. There are several forms of solar energy, and for the most part, early civilisations have used the passive heating of the Sun as well the stored energy within the biomass. Such applications are still in use in our current century with modified and developed versions.

However, until 1839, no one had an idea about the photovoltaic effect which was observed by Alexandre-Edmond Becquerel [1]. He realised that when platinum electrodes placed in an electrolyte containing an acidic solution with silver chloride dissolved in and illuminated, it would enhance the current. Unfortunately, back then the distinction between chemical effects and the photoelectric effect was not recognised and the results were considered to be an effect of the former.

In 1876, William Grylls Adams and Richard Evans Day used a platinum-selenium junction to observe the photovoltaic effect [2]. However, they did not consider the illumination to be the acting phenomenon in the current generation, but the crystal formation caused by the illumination.

In 1887 and 1905, respectively, Heinrich Rudolf Hertz discovered, and Albert Einstein further explained the photoelectric effect; a material-dependent threshold frequency [3]. The material can only absorb photons that can overcome this threshold and by doing so emits an electron.

One of the most important materials for solar cell production is monocrystalline silicon. It was realised early on that the material quality and purity play a major role in the performance of the cells. In 1918, Jan Czochralski invented a method in which high-quality crystalline materials can be grown which found its way to the c-Si technology around the 1950s [3].

The very first solar cell ever made was in 1954, when Daryl Muscott Chapin, Calvin Souther Fuller and Gerald L. Pearson of Bell Laboratories made a silicon-based cell with approximately 6% conversion efficiency [4].

The use of solar cells was first introduced as a power supply for space applications, especially for the Earth-orbiting satellites. For example, Vanguard 1, the fourth artificial satellite orbiting the Earth, was the first satellite with solar cells installed to it [5]. The first satellite, Sputnik 1, however; used silver-zinc based batteries to stay powered up for its mission which gave out after 22 days [6].

The oil crisis of 1973 brought the necessity of alternative energy sources to the surface among those was the terrestrial use of solar cells. As such, many companies around the globe started to manufacture photovoltaic modules and arrays applicable for such purpose. This increased the need for high-efficiency cells to be produced, thus many research facilities have been established around the world working restlessly to manufacture cost-efficient and industrially applicable solar cells while still performing as well as possible.

Although the silicon dominates the industry, the research for other semiconductor materials still continues, whether it may be amorphous silicon, III-V and II-VI semiconductors, or hetero compounds, and tandem cells for better absorption of the solar spectrum.

1.1.2 The Necessity of Solar Energy

The World's energy demand is continuously increasing. One of the most dependable energy sources since the industrial age has been coal. The coal, just like other fossil fuels yielded an amazing energy quota. Fossil fuels, however, are not sufficient enough as their fast depletion without proper generation makes them unsustainable. The other effect of the use of fossil fuels is on the environment. The

increase in the amount of greenhouse gases, such as carbon dioxide, poorly affects the climate and contributes to global warming. Because of these reasons, a new kind of energy source that can be "replenished by the natural process at a rate that is comparable or faster than its rate of consumption" is needed [5].

The renewable energy sources can be listed as wind, hydropower, tidal, geothermal, biomass and solar. Some of these sources are (directly or indirectly) powered by the Sun. Hydropower, tidal and geothermal sources use the flow of water, gravitational pull of the Moon and internal heat of the Earth as the source, respectively [7]. Most of the renewable energy sources have location dependency. For instance, dams for hydropower, require to be built on water sources, such as rivers, where elevation is also sufficient to induce water flow. However, these conditions do not exist everywhere on Earth. On the other hand, solar energy systems can be built on almost every location on Earth, shown in Figure 1.

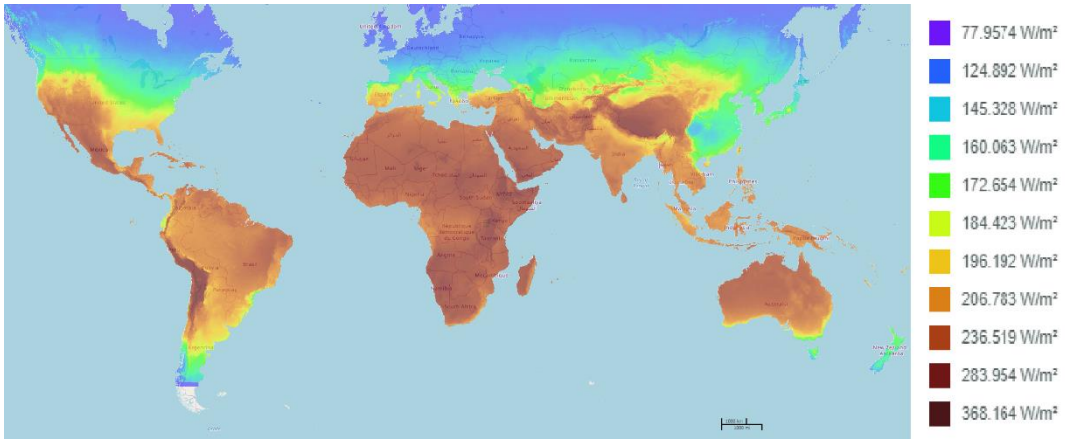

Figure 1 The solar power distribution around the World. (Adapted from [8].)

Solar cells can be installed on virtually anything, from immobile structures such as; rooftops and sides of buildings, over the parking lots, to mobile structures such as cars, buses, trains and planes. These adaptations reduce the local energy consumption, if not completely remove it. It is also possible that the generated energy can be sold if there exists a grid connection.

1.1.3 The Operating Principle of Solar Cells

1.1.3.1 The Silicon as a Bulk Material

According to their electrical conductivity, materials can be grouped under three different categories; conductors, semiconductors and insulators. One of the key parameters that affect the electrical conductivity of a material is the temperature. Semiconductors, for instance, behave like insulators when the temperatures approach absolute zero in Kelvin, whereas metals at that temperature are highly conductive. As the temperature increases, semiconductor materials become more and more conductive while the conductivity of metals decreases.

The conductivity of material arises from its lattice structure, i.e. whether the material has an amorphous or crystalline structure. For amorphous structure, atoms do not have a recognisable periodicity, while for a crystalline structure, atoms have (near) perfect periodicity. For the crystalline form of silicon which is an element on the fourth group (Figure 2 (a)) of the periodic table, the atoms are arranged in a diamond lattice (Figure 2 (c)). The atoms form a covalent bond (Figure 2 (b)) with one another and its effect can be recognised on the macroscopic level as the hardness of the material. For the semiconductor material to be conductive, some of these bonds must be broken so that free electrons would be present. This occurs when the temperature is different from 0 K.

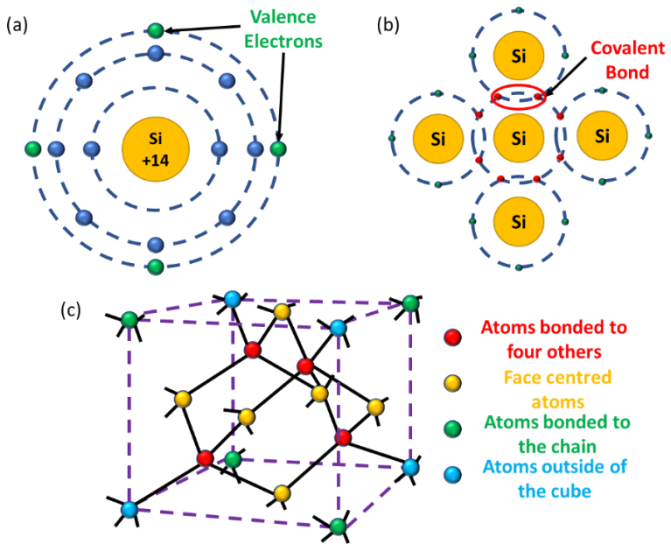

Figure 2 The atomic (a), the bond (b) and the lattice (c) structure of the silicon atoms.

Within a crystal lattice, the atoms are bonded together. This causes the energy levels of the atoms to interact with each other and split. This split is more prominent as the interatomic distance decreases and eventually at a specific distance there exists a clear gap between the bands which are called valence and conduction bands (Figure 3). This gap is called the bandgap, E_g, in which no electron states can exist. This is a material-specific parameter, e.g. for silicon, it is 1.17 eV at 0 K and 1.11 eV at 300 K [9]. The following empirical relationship by Varshni expresses the dependence of bandgap to temperature:

$$E_g(T) = E_g(0) - \frac{\alpha T^2}{T + \beta} \qquad \textit{(Eq. 1) [10]}$$

where α (7.021 x1 0^{-4} eV/K for silicon) and β (1108 K for silicon) are the fitting constants and $E_g(0)$ (1.16 eV for silicon) is the bandgap of the semiconductor at 0 K [10]. The insulators do have a bandgap as well, however, this gap is significantly larger in comparison to semiconductors which is between a few tenths of electron-volt to around 2 eV [11]. Metals rarely have a strictly periodic crystal lattice; therefore, electrons are not bounded, allowing free flow.

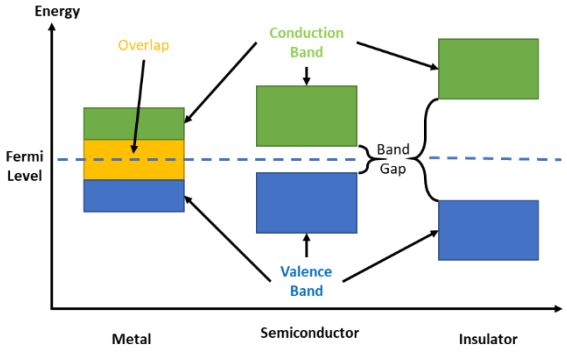

Figure 3 The energy band structure of metals, semiconductors and insulators.

1.1.3.2 The Charge Carriers in Semiconductors

The semiconductors at absolute zero Kelvin has all their electrons in the valence band and no electrons are present in the conduction band (Figure 4). As the temperature increases, some of these electrons are excited to the conduction band and occupy permitted energy states. Such states lie very close to the edge of the conduction band. However low in number, these electrons interact with the lattice which has a

significant effect on conduction. On the other hand, in the valence band, as some of the electrons are excited to the conduction band, leaving behind some empty space. These unoccupied states are called holes or defect electrons which are surrounded by electrons. Both electrons and holes can be considered as charge carriers in semiconductors and their interaction with the lattice has important consequences.

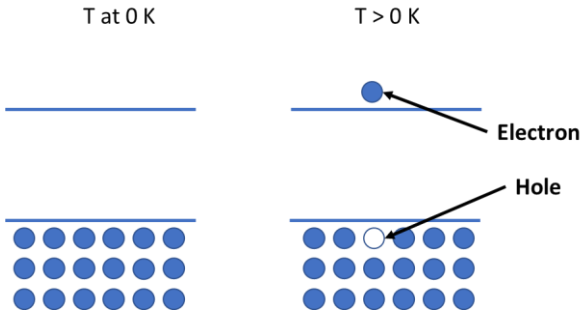

Figure 4 The state occupancies at different temperatures.

The temperature dependence of the state occupancy is given by the Fermi-Dirac distribution as;

$$f(E) = \frac{1}{1 + e^{\left(\frac{E - E_F}{kT}\right)}} \qquad \textit{(Eq. 2) [11]}$$

where E_F is the Fermi energy, k is the Boltzmann constant and T is the absolute temperature. For a semiconductor to be conductive it needs to have free electrons present. Their number can be figured out from the following relation;

$$n = N_C\, e^{\left(\frac{E_F - E_C}{kT}\right)} \qquad \textit{(Eq. 3) [11]}$$

where N_C is the effective density of states of electrons in the conduction band and E_C is the conduction band-edge energy.

For the number of holes in the valence band, the following relation can be used;

$$p = N_V e^{\left(\frac{E_V - E_F}{kT}\right)} \qquad \textit{(Eq. 4) [11]}$$

where N_V is the effective density of states of holes in the valence band and E_V is the valence band-edge energy.

According to Fermi-Dirac distribution, under thermal equilibrium, the number of electrons in the conduction band and the number of holes in the valence band must be equal to one another for an ideal semiconductor without any defects. From such a relation, Fermi energy level is given as,

$$E_F = \frac{E_V + E_C}{2} + \frac{kT}{2} ln\left(\frac{N_V}{N_C}\right) \qquad \textit{(Eq. 5) [11]}$$

1.1.3.3 Effects of Impurities to the Conductivity of a Semiconductor

Conductivity, apart from temperature is also related to the concentration of the charge carriers within the semiconductor material. The concentration is varied by a process called doping, in which impurities to the material are introduced on purpose. Atoms that have more valence electrons than of silicon which has four valance electrons (Figure 2 (a)) can be used as donors. The general element used for such purpose is phosphorus (Figure 5 (a)) which has five valance electrons. Replaced with silicon within the lattice four electrons of the phosphorus will bond with surrounding silicon atoms and the remaining single electron will be donated and such a material is called n-type.

On the other hand, the silicon can be replaced with atoms that have fewer valence electrons than of silicon; in general boron (Figure 5 (b)) is used for this

purpose. Boron having, three electrons, will form bonds with silicon resulting in a hole. These type of materials are called acceptors and the material is called p-type.

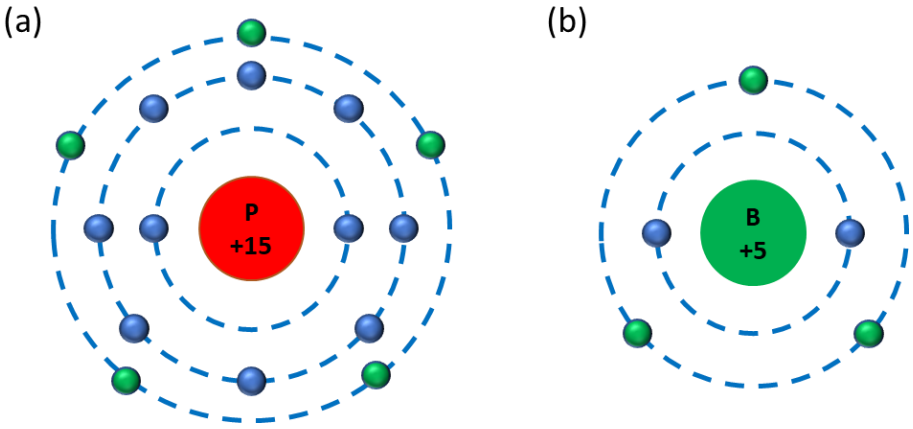

Figure 5 The electron configuration of (a) phosphorus and (b) boron atoms. Valence orbit electrons are shown as green orbs.

1.1.3.4 The Current Transport Mechanisms in Semiconductors

The free electrons and the holes are how the current is carried in a semiconductor. When an electric field is present, it would apply force on the electrons that will then increase their energy and move them around (Figure 6). In semiconductors, electrons will collide with the lattice or with an impurity atom, or with another electron which will cause the electrons to lose their energies to the lattice in the form of heat [11]. As the charges move under the effect of the electric field, they induce an electric current which is called the drift current with the following equation;

$$J_{Drift} = qn\mu_n E \qquad \textbf{(Eq. 6) [12]}$$

Another current-carrying mechanism arises from the difference in carrier concentrations. The current carrier will move from higher concentration to a lower one (Figure 6). This is called the diffusion current with the equation shown below (Eq.7). Both current types are linked to one another as both arise from a collision and statistical movements of charge carriers.

$$J_{Diffusion} = qD_n \frac{dn}{dx} \qquad \textit{(Eq. 7) [12]}$$

where both equations are considered for n-type semiconductors with nonuniform doping concentration and replacing the letter n with the letter p would give the equations for a p-type semiconductor. In both equations, q indicates the unit charge and n indicates the concentration of the free electrons. For the drift relation; μ_n is the mobility of free electrons. E indicates the magnitude of the applied electric field in one direction. For the diffusion relation; D_n is called the Einstein relation.

Then the total current can be related as,

$$J_{Total} = J_{Drift} + J_{Diffusion} = qn\mu_n E + qD_n \frac{dn}{dx} \qquad \textit{(Eq. 8) [12]}$$

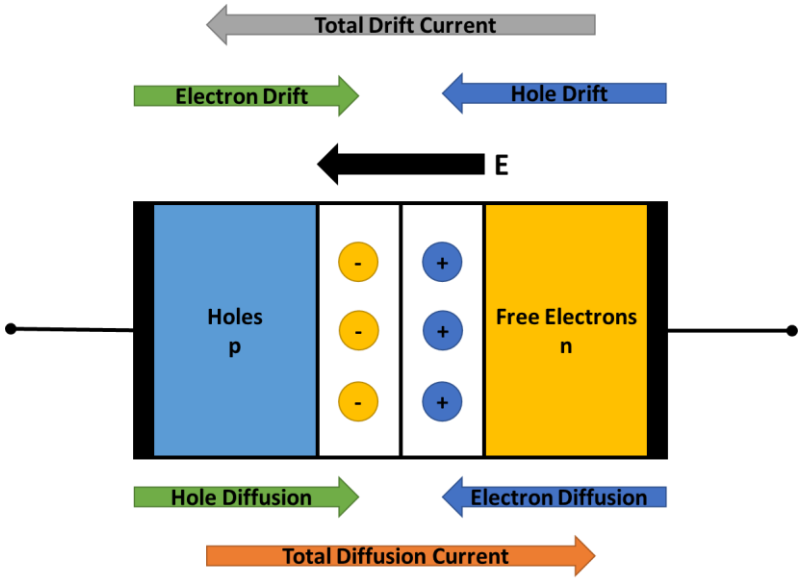

Figure 6 The drift and diffusion currents in a p-n junction.

1.1.3.5 Charge Carrier Generation Under Illumination

Photons with energies higher than the bandgap energy of a semiconductor will be absorbed and the electrons will be excited from the valence band to the conduction band. Photons, however, have negligibly small momentum. Therefore, an absorbed photon will increase the energy of the crystal while the momentum remains mostly unchanged.

Semiconductor materials can be classified under two groups according to their capabilities of absorbing a photon. If the maximum energy of the valence band lies directly below the minimum energy of the conduction band in the momentum-space, this type of semiconductor is called a direct semiconductor (Figure 7 (a)). An example of such a material is GaAs.

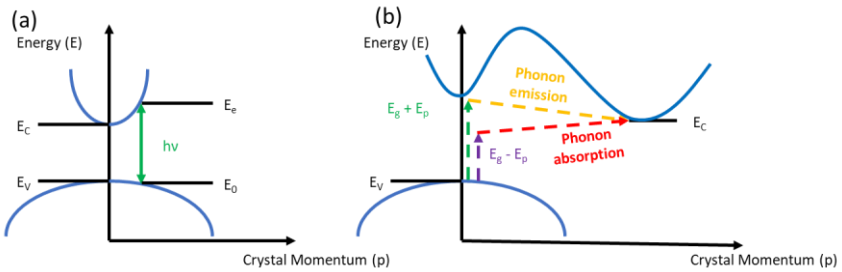

Figure 7 The band structure of (a) direct and (b) indirect semiconductors.

If the maxima of the valance band are not below the minima of the conduction band in the same momentum-space, this is called an indirect semiconductor (Figure 7 (b)). Silicon has an indirect bandgap. Such indirect materials require the contribution from the crystal lattice in the form of phonons; low energy, high momentum particles; to be able to generate electron-hole pairs, thus current.

There are some crucial differences between direct and indirect absorption. As the phonons are required in indirect materials, the probability of absorption is lower than of the direct materials. Because of this difference; for the photon to be absorbed; the indirect material should be thicker (around 200 μm), whereas for direct materials the material can be relatively thinner (few μm) to achieve absorption in the whole spectrum [11].

1.1.3.6 The Recombination of Electron Hole Pairs

When the incident light is absorbed, generated charge carriers would either be collected at the corresponding contacts or lost via different mechanisms. Recombination is one of the most prominent lost mechanisms where a generated carrier recombines with another carrier and losses its energy before being collected.

The radiative recombination (Figure 8) is the return of the electron from the conduction band to the valence band, emitting a photon while doing so. The

recombination is one-one, meaning one electron will annihilate one hole in the process. In indirect materials, the recombination behaviour is similar to the absorption. Because of this, an indirect material has long charge carrier lifetimes than of direct materials. The radiative recombination process is the main working principle of semiconductor-based LED and laser technology.

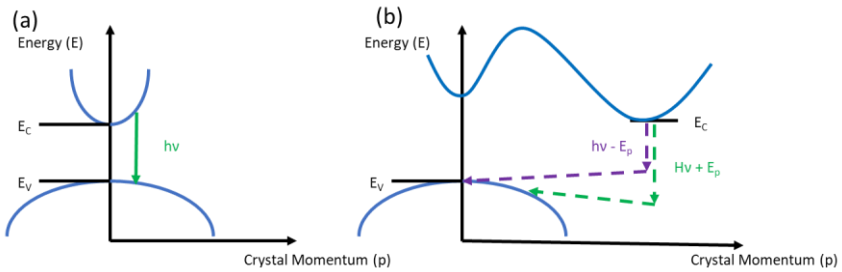

Figure 8 The radiative recombination of (a) direct and (b) indirect semiconductors.

The Auger recombination (Figure 9) occurs when a recombining electron transfers its extra energy to another electron either in conduction or valence band resulting in the second electron to move to a higher energy level. The second electron then starts to lose its energy to collisions with the lattice up until it reaches to its original state. This behaviour can be very well observed in highly doped materials.

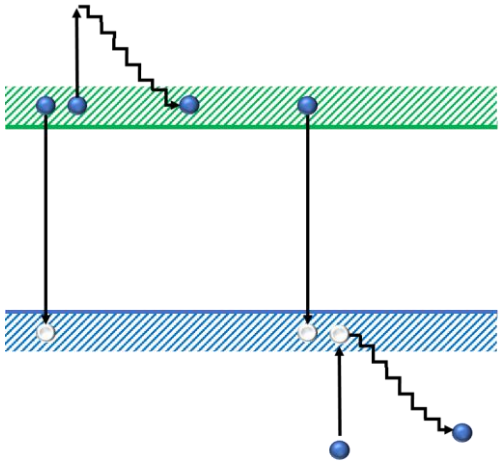

Figure 9 Auger recombination (a) in the conduction band and (b) in the valence band.

The Shockley, Read and Hall (SRH) recombination occurs when there exist crystal defects and impurities (Figure 11) which can trap the charge carriers, in the forbidden band. This type of recombination (Figure 10) can occur in four fundamental

processes; (1) an electron can be trapped by an unoccupied state, (2) an electron can be emitted from the occupied trap state to the conduction band, (3) a hole can be trapped by an occupied state and (4) a hole can be emitted from the occupied trap state to the valence band.

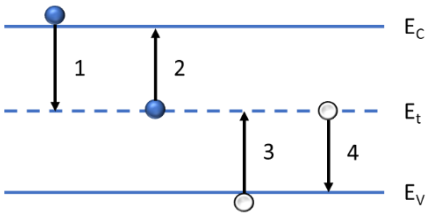

Figure 10 The possible processes of SRH recombination.

For the high-level injection case, the lifetime depends on the probability of carriers being captured by the trap states and not on their concentration. For the low-level injection case, the minority carrier lifetime is inversely proportional to the number of impurities.

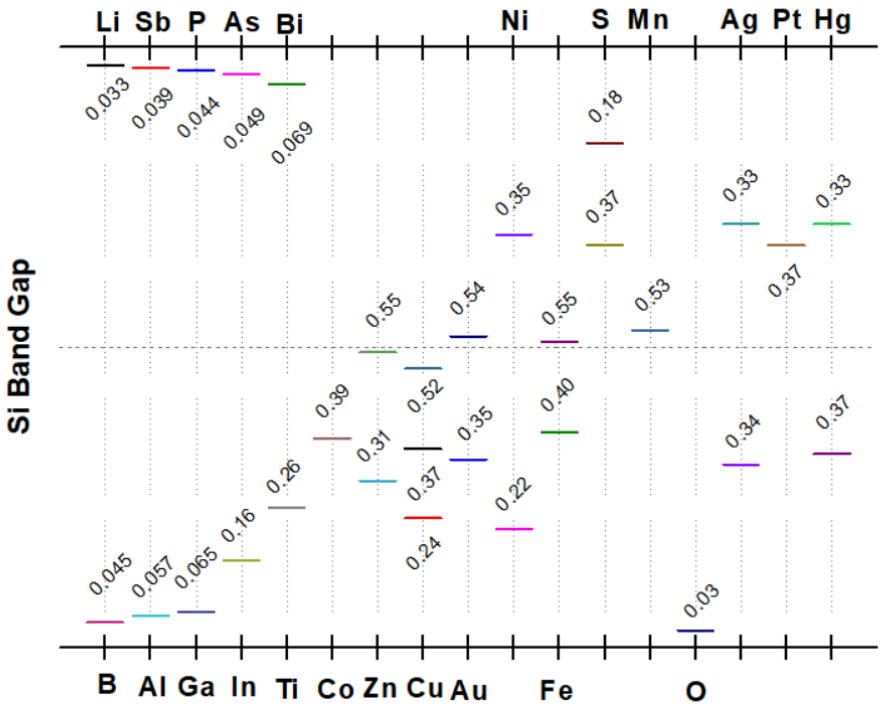

Figure 11 Some trap states of elements in silicon.

The lifetime of a material depends on the three aforementioned recombination processes and can be represented as follows;

$$\frac{1}{\tau_{\text{Total}}} = \frac{1}{\tau_{\text{Radiation}}} + \frac{1}{\tau_{\text{Auger}}} + \frac{1}{\tau_{\text{SRH}}} \qquad \textit{(Eq. 9) [11]}$$

1.1.4 The Sun as the Energy Source

The Sun is the centre of our solar system and our major energy source. At its core, nuclear fusion occurs which yields a very large amount of energy that is then released as electromagnetic radiation. Through absorption and re-emission, this energy is transferred to the surface of the earth. The visible surface of the sun (photosphere) has a temperature around 6000 K. At the mean distance between the Earth and the Sun, around 150 million km [13], the irradiance just outside of the Earth's atmosphere is 1361 W/m^2 which is called the solar constant [5]. This level is also called air mass (AM) zero, as no atmosphere is encountered by the solar irradiation. AM is the thickness of atmosphere solar irradiance has to pass through, which attenuates it (Figure 12). It is formulated as follows;

$$\text{AM} = \frac{1}{\cos\theta} \qquad \textit{(Eq.10) [5]}$$

The shortest distance is when the Sun is at zenith point, thus the angle the Sun makes with that point is indicated as 0° and when the Sun is at the horizon it is at 90°. The zenith (0°) point is called AM1, the industrial standard, AM1.5 corresponds to 48.2° in which the irradiance is taken as 1000 W/m^2, and at 60° it is AM2. AM1.5 is also separated into two: the light which is directly coming from the Sun; labelled with the letter D, or all light including those reflected from the surfaces around the ambience, which is denoted as global, G.

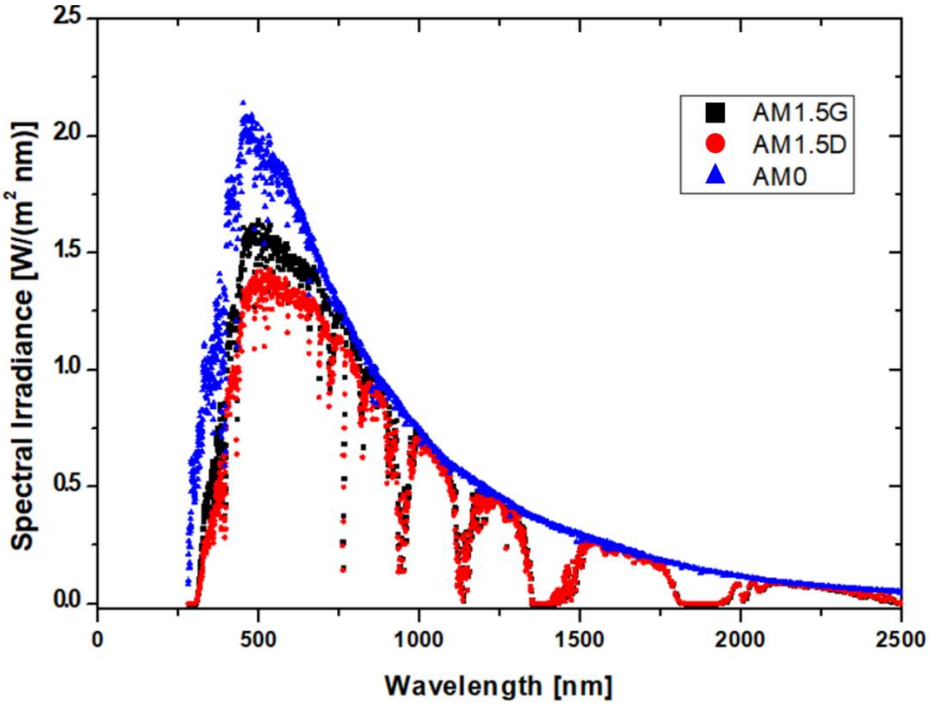

Figure 12 The solar spectrum at different air mass levels (Adapted from [14]).

1.1.5 Important Parameters and Equivalent Circuit Representation of Solar Cells

1.1.5.1 The Parameters

The solar cell performance can be represented by four important parameters which are obtained from J-V curves (Figure 13). The J-V curve can be used to extract preliminary parameters of a completed solar cell which are the short-circuit current density (J_{sc}), the open-circuit voltage (V_{oc}), and maximum power current density (J_{pm}) and voltage (V_{pm}) points. From these preliminary parameters, the fill factor (FF) and the efficiency (η) can be calculated with the given area (A) of the sample, but since the current density by definition has the area effect considered, the area factor can be ignored. As the solar cells are capable of absorbing light to generate current, the efficiency calculations are standardised to certain measurement rules. For instance, the illumination power (G) should be 1000 W/m^2 and it should also be similar to the solar irradiance which is called AM 1.5G. At the same time, the sample must be kept at a constant temperature which is 25°C.

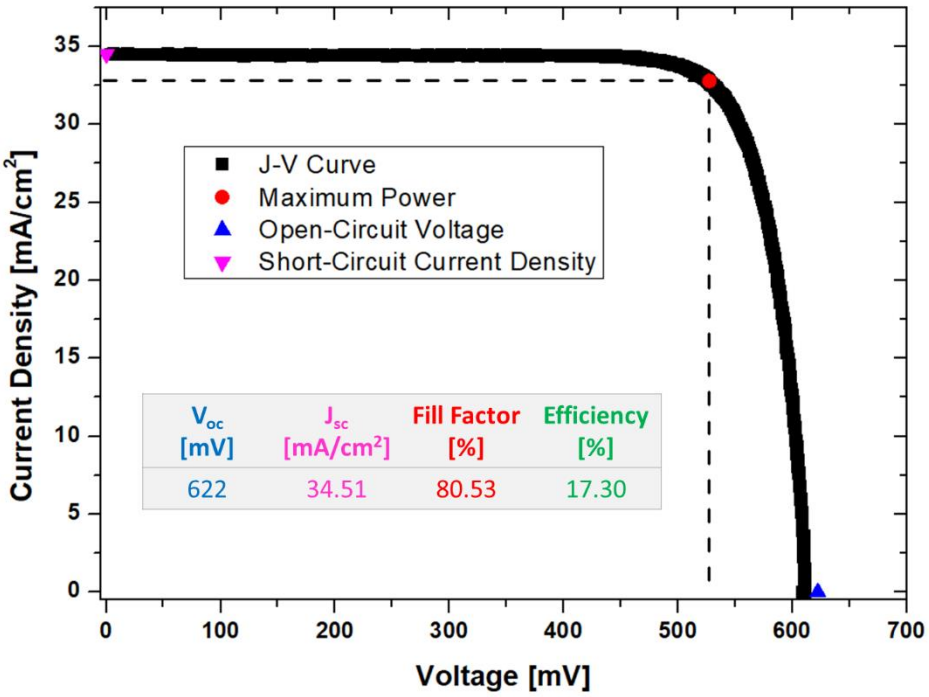

Figure 13 A sample J-V curve of a solar cell made in GÜNAM.

The short-circuit current density is the maximum current value the solar cell generates under illumination, and for that reason, it is dependent on the photon flux density. The use of current density instead of the current value is to remove the area dependence. The theoretical maximum current density of a solar cell can deliver is 46 mA/cm^2 [5], and in laboratory maximum current density measured from a c-Si solar cell is 42.3 mA/cm^2 and maximum reported commercial value is 41.3 mA/cm^2 [15].

The open-circuit voltage is the maximum voltage a solar cell can have when no current flows through it. This value represents the recombination of charge carriers in a cell. Maximum reported V_{oc} values for laboratory cells is around 744 mV and for commercial ones is around 737 mV [15].

The fill factor (Eq. 11) is the ratio of the maximum power of a cell to the product of V_{oc} and J_{sc}. In solar cells fabricated from the same material, the fill factor variation will be highly indifferent. It also represents the quality of the junction and the type of recombination with the ideality factor. Parasitic resistive forces also reduce the fill factor.

$$FF = \frac{V_{pm} \cdot J_{pm}}{V_{oc} \cdot J_{sc}} \qquad \textit{(Eq. 11) [5]}$$

The conversion efficiency (Eq. 12) value is the ratio of maximum power to the incident light power. As mentioned, due to the standardisation this is fixed at 1000 W/m^2 at room temperature.

$$\eta = \frac{P_{max}}{G} = \frac{V_{pm} \cdot J_{pm}}{G} = \frac{FF. V_{oc} \cdot J_{sc}}{G} \qquad \textit{(Eq. 12) [5]}$$

1.1.5.2 The Equivalent Circuit Representation

The solar cells can be represented by an equivalent circuit (Figure 14) that can be used to model their working principle and determine their characteristic behaviour of the relation between current and voltage. The model can be designed in three different variations, the simplest one being the ideal case where a current source and a single diode connected in parallel to one another (Figure 14 (a)). It is often more realistic to consider the external resistances (R_{Series}) due to the contacts and the shunts (R_{Shunt}) within the semiconductor material due to processes into account as well. For that reason, such resistances are added to the equivalent circuit in series for contacts and in parallel for modelling the sample (Figure 14 (b)). The series resistance affects the performance of the solar cell negatively, as the photo-generated current is lost without being contributed to the actual external device. On the other hand, the shunt resistance must be as high as possible, so that the diode can operate well. As the light-generated electron-hole pairs at the p-n junction recombine, this has a negative effect on the performance of the solar cell. This factor can be represented by an additional diode included at the solar cell circuit representation (Figure 14 (c)) which would have an ideality factor larger than one. The following equation is considered as the most realistic representation;

$$I(V) = I_{Diode-1}\left[\exp\left(\frac{e(V - AIR_{Series})}{n_1 kT}\right) - 1\right] + I_{Diode-2}\left[\exp\left(\frac{e(V - AIR_{Series})}{n_2 kT}\right) - 1\right] + \frac{V - AIR_{Series}}{R_{Shunt}} - I_{Photon} \quad \textit{(Eq. 13) [5]}$$

where $I_{Diode-1}$ and $I_{Diode-2}$ are the saturation currents of the two diodes with ideality factors n_1 and n_2, respectively. A is the area of the solar cell and V is the external voltage.

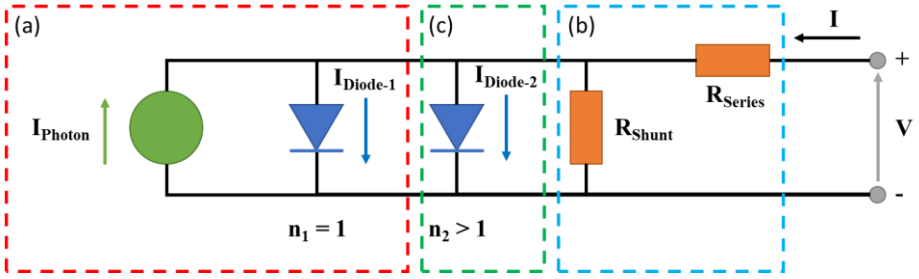

Figure 14 The equivalent circuit of (a) an ideal solar cell (b) with series and shunt resistance (c) with the two-diode model.

1.1.6 Theoretical Limits of Semiconductors

One of the important aspects of a solar cell is its conversion efficiency. It is imperative to understand that not all of the incident light on a solar cell can be turned into electricity. There are some important and major limiting parameters for solar cell efficiency.

The first limit to the efficiency comes from the thermodynamics (Figure 15). The idea is to consider the solar cell as a heat engine which has an absorber part and it is in ambient with the temperature of T_C 300 K. Here the absorber temperature T_A is converted into chemical energy which is stored at the electron-hole pairs within the solar cell. If this conversion happens without any losses, it can be considered as having an efficiency of 1. Thus, the efficiency of the thermodynamic heat engine (THE) can be given as,

$$\eta_{THE} = 1 - \frac{T_C}{T_A} \qquad \textit{(Eq.14) [5]}$$

If we consider the absorber to be a blackbody, it will absorb all the incident light from the Sun with the blackbody temperature of T_S 6000 K. If we assume that the maximal concentration is satisfied then the maximum absorber (A) efficiency can be given as,

$$\eta_A^{Max} = 1 - \frac{T_A^4}{T_S^4} \qquad \textit{(Eq.15) [5]}$$

If both of these equations (Eq.14) and (Eq.15) are combined the ideal solar cell (SC) efficiency can be defined with the following relation,

$$\eta_{SC} = \left(1 - \frac{T_C}{T_A}\right)\left(1 - \frac{T_A^4}{T_S^4}\right) \qquad \textit{(Eq.16) [5]}$$

From such an efficiency relation it can be said that around 2540 K the maximum efficiency, around 85%, is achieved. Of course, at this temperature, the majority of the elements would be either in liquid or gas phase, which includes most elements involved in semiconductors, with the exception of carbon [16].

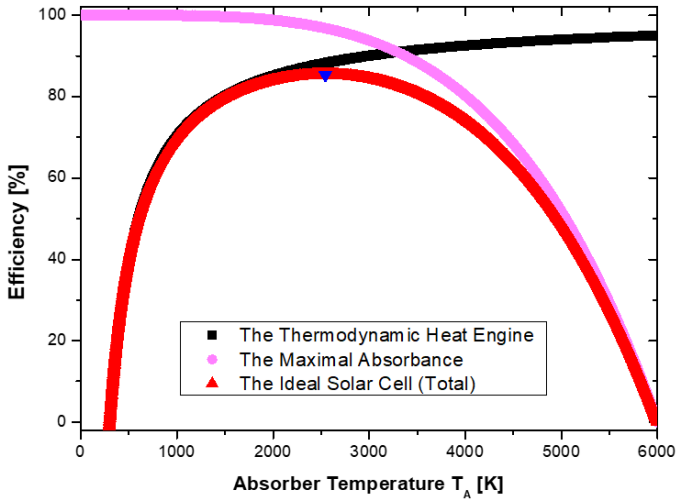

Figure 15 The efficiency limit of a solar cell for a solar temperature of 6000 K and an ambient temperature of 300 K. The blue point indicates the maximum efficiency which is 85% for an absorber temperature around 2540 K.

The second limiting case is called the Shockley-Queisser or detailed balance limit [17]. It is calculated by William Shockley and Hans J. Queisser and it can be described as the highest possible efficiency a single p-n junction can yield. As a semiconductor material can only absorb photons that have equal or higher energy than its bandgap, low energy ones will be transmitted. On the other hand, energetic photons will lose their extra energy to the lattice as heat in order to generate an electron-hole pair. The probability of this happening is high since the electrons tend to occupy the bottom of the conduction band and the holes the top of the valance band. This mismatch between the solar spectrum and the semiconductor material is one of the loss mechanisms calculated in this limiting case.

When they assumed that only one type of recombination is active in the solar cell, that is the radiative recombination and also considering the bandgap of the material, they have realised that for 1.1 eV (corresponds to Si) the maximum efficiency is 30% [17].

1.2 Classification of Solar Cells

The solar cells are separated into three groups based on the materials used, physical principles in action and to the advancements of the technology.

1.2.1 Crystalline Silicon-Based Solar Cells

This type of solar cell is based on silicon-based materials, whether mono-crystalline or multi-crystalline. The most conventional solar cell, called Al-Back Surface Field (Al-BSF, Figure 16), is typically made on a p-type wafer with a thickness of around 200 μm. The substrate is symmetrically doped with Phosphorus (P) on both sides. Afterwards, the front side is coated with SiN_x which acts as an anti-reflective coating (ARC). Finally, the rear side is fully screen-printed with Al, and on the front side, H-shaped grids are screen-printed with Ag paste which is then co-fired through a high temperature firing step.

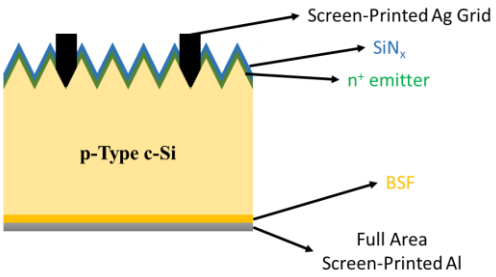

Figure 16 The cross-section of Al-BSF structure.

Currently, the highest efficiency belonging to such a structure is 20.29% produced at Shinsung Solar Energy [18]. Even though an impressive feat, there are other structures that utilise monocrystalline Si wafers to produce higher efficiencies by altering various parts of a solar cell and reducing the effect of loss mechanisms.

1.2.1.1 High-Efficiency c-Si Solar Cell Concepts

This type of cell utilises new device and material combinations designed and realized by many R&D activities in order to reach very high conversion efficiency values. For this purpose, the quality of the bulk material has been improved. For enhanced light absorption, novel texturing techniques have been developed. The doping process has been optimised to achieve better p-n junction. In order to obtain higher efficiencies, apart from these optimisations of process steps, the bulk material type can be switched from p-type to n-type in order to get rid of light-induced degradation caused by boron-oxygen compounds which act as a defect [19, 20]. Also, n-type wafers are less sensitive to impurities than p-type [22]. Moreover, oxidation can be used to passivate the surfaces to achieve lower surface recombination. In addition, multiple ARC layers can be applied so that more photons would be directed into the material rather than being reflected away. Contact formation can be altered in various ways to increase the collection of minority carriers, or even reduce the shadowing effects. All these changes can be applied, and their optimisation may result in a cell that is highly efficient.

There are many different techniques to achieve any of the listed improvements here, however, there also exists the fact that some of these improvements may not be viable as far as the industry is considered. As such, some of these improvements can

be applied by devices that have a very low manufacturing yield, in comparison to higher yield with lesser efficient ones.

High-efficiency solar cells can be listed as, passivated emitter rear locally diffused cells (PERL), passivated emitter rear totally diffused cells (PERT), passivated emitter and rear contact cells (PERC), interdigitated back-contact cells (IBC), heterojunction cells with an intrinsic thin layer (HIT), buried contact cells; metal-wrap-through (MWT) and emitter-wrap-through cells (EWT).

a) Monofacial Solar Cells

This type of cell has the grid pattern on the light-receiving side whereas the other side is completely covered with reflective contact metals to ensure a second absorption of the incident light. The contact structure can be different, but the rear sides are fully covered with metal. It is also observed that both types utilise p-type wafers as a substrate. The reason for this is because of the use of aluminium on the rear side generates a highly doped p^+ region which will act as Back Surface field (BSF).

PERC (Figure 17) is an improvement on the conventional Al-BSF structure, in which the rear surface is coated with a dielectric material that prevents full area contact formation between aluminium and silicon. Then; earlier with photolithography, afterwards with a laser; point contact holes or line contacts are formed through the dielectric material. The application of the dielectric material reduces the rear-surface recombination due to the full area metallisation which also behaves like a rear-surface reflector, giving the infrared region photons a second chance to be absorbed. Point contacts introduce a trade-off between recombination and resistance losses. Introducing a boron-doped layer on the rear whether fully or just where the point contacts are, has the potential to increase the efficiency of the cell as this would enhance the efficiency of the BSF. Such structures are called PERT and PERL, respectively, and they present good light trapping due to texturing, reflection control, optimised grid design, good surface passivation and high minority carrier lifetimes [21].

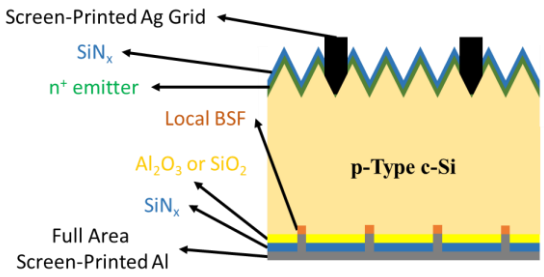

Figure 17 The cross-section of a p-type PERC solar cell.

The best PERC cells currently made in Australian National University which have an efficiency of 23.10% and fill factor of 82.10% with the open-circuit voltage of 688 mV and short-circuit current density of 40.80 mA/cm^2 with the area of 4 cm^2 [22].

b) Bifacial Solar Cells

This type of solar cells has the grid pattern printed on both sides as opposed to monofacial cells (Figure 18 (b)). This change allows for the solar cell to absorb sunlight from both front and rear surfaces. Such change also reduces the amount of paste used on the rear side as the grid pattern has large openings to allow the sunlight to pass through. The reason behind the grid pattern on the rear side is to allow diffused light from the surroundings to be incorporated into photoconversion as well. The efficiency values are measured from both sides and their ratio is called the bifaciality of the cell and it should be less than one otherwise, it would indicate that the solar cell is on its rear side.

$$\varphi_\eta = \frac{\eta_{\text{Rear}}}{\eta_{\text{Front}}} < 1 \qquad \textit{(Eq.17) [23]}$$

The bifacial structure can be applied to various existing structures such as PERC+ cells.

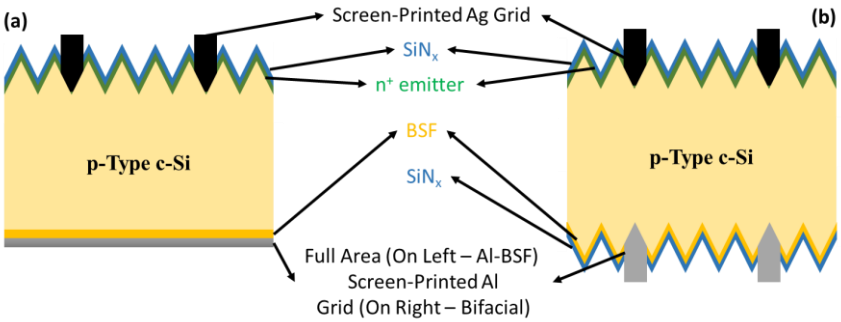

Figure 18 The cross-sections of (a) Al-BSF and (b) bifacial solar cell structures.

For the bifacial solar cell structure, the following cell made by Konstanz, with efficiency 19.51% (on the rear side - 19.38%) on 5 inches wafer [24]. The front and rear V_{oc} value was measured as 661 mV, J_{sc} value was 37.60 mA/cm^2 (on the rear side – 37.30 mA/cm^2) and FF of 78.44% (on the rear side – 78.54%). This bifacial cell almost has a bifaciality of 1. The champion bifacial cell efficiency, however, belongs to Trina Solar with 24.58% on n-type mono-crystalline silicon i-TOPCon structure [25].

c) Back Contact - Back Junction (BC – BJ) Solar Cells

The BC – BJ solar cells are the variations of the conventional cell in which the metal contacts and the front emitter is delocalised to the rear surface which means about 5-7% gain in the photogenerated current as no shadowing due to metallisation is present [28]. The structural shift occurs gradually, first by the delocalisation of the busbars to the rear leaving the fingers on the front surface, the second shift is the delocalisation of the fingers to the rear surface and finally moving the entire front structure to the rear side.

I. MWT

As mentioned, this is the first variation from the conventional solar cell (Figure 19). By the utilisation of lasers, tunnels through the wafers are drilled, which are then doped to form an emitter layer. Then the busbar on the front side is delocalised to the rear side and the fingers are connected to the rear busbar through the tunnels. This variation from the conventional cell increases the front surface illumination area.

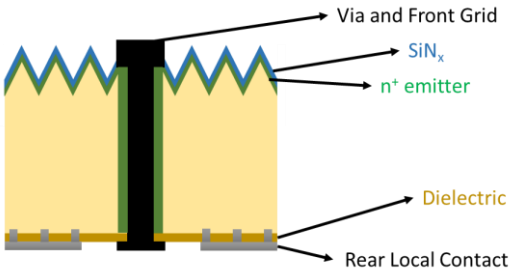

Figure 19 The cross-section of MWT solar cell structure.

Some high-efficiency solar cells fabricated via MWT structure with 20.10% efficiency comes from Fraunhofer ISE [26] and with 19.70% efficiency from ECN [27] both of which have an area of 239 cm^2.

II. EWT

In this type of cell (Figure 20), the emitter is expanded through the laser formed tunnels to the rear side of the cell where the emitter is doped in a grid pattern as well. But the contacts are formed on the rear side only, further increasing the illumination area as the grid pattern on the front side is also eliminated.

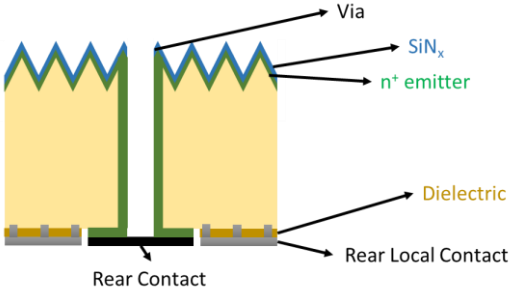

Figure 20 The cross-section of EWT solar cell structure.

Some of the high efficiencies in EWT solar cell structure are 21.60% by ISFH [28], 18.60% by FBK [29] and 15.70% by Fraunhofer ISE [30] with areas 4 cm^2, 0.16 cm^2 and 19.35 cm^2, respectively.

III. IBC

Interdigitated back-contact solar cells change the conventional solar cell structure by moving the front contacts completely to the rear side, as shown in Figure 21, just like the EWT structure. But the emitter is also moved to the rear instead of elongating it through the solar cell. By moving the contacts to the rear side, the optical shadowing effects are avoided which translates to an increase in solar cell efficiency as absorption and short circuit current density increase [31]. The front surface, being free from contacts which remove the contact resistivity considerations, can be optimised to have the best surface passivation performance [32]. Since the trade-off between grid structure and illumination area is removed contact size can be increased on the rear side to reduce contact resistivity. Interconnection during modulation becomes easier for such cells and uniform ARC layer provides visually pleasing results.

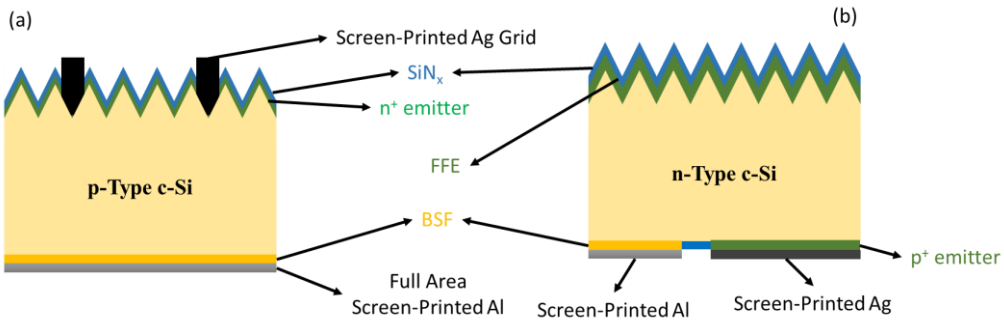

Figure 21 The cross-sections of (a) conventional Al-BSF and (b) IBC solar cells.

Due to the low susceptibility to impurities [33], n-type wafers are the usual choice for IBC solar cells. It is also required that high-quality materials with long diffusion length to be used as the photogenerated electron-hole pairs have to travel to the rear side of the wafer where the p-n junction resides [34]. For that purpose, excellent surface passivation must be achieved on both sides of the wafers and on the front side pyramid structure with ARC layer to increase light trapping.

The formation of a p-n junction on the rear side becomes troublesome as it increases the required amount of process steps if the lithography [35] – diffusion path is chosen which is also alignment dependent, or if ion-implantation path is chosen the alignment requirement still continues and also adds the high activation temperature

problem [36]. Laser doping [37] could be a viable option as it eliminates high activation temperature and the use of laser for multiple steps for contact formation could be applicable [38]. However, the laser process is also slow compared to other methods. Fourth doping method is the use of screen-printed boron paste [39] in junction with phosphorus diffusion which also has the potential to suffer from alignment problems. But among all processes, it is relatively the cheapest, safest and also presents an industrially applicable side.

The leading IBC solar cell belongs to Kaneka with their n-type heterojunction IBC cell structure. The cells have an efficiency of 26.6% with a designated illumination area of 179.7 cm^2, V_{oc} 740 mV and J_{sc} 42.5 mA/cm^2 amassing to an FF of 84.6% [15]. The second-best IBC cell efficiency with 26.1% belongs to ISFH with passivating POLO contacts for both polarities. The cells have V_{oc} 727 mV and J_{sc} 42.6 mA/cm^2 and an FF of 84.3% [40]. Before Kaneka took the lead SunPower held the record efficiency in IBC solar cells. Their mono c-Si cell structure with V_{oc} 737 mV, J_{sc} 41.33 mA/cm^2 and FF of 82.70% yielded 25.20% efficiency in 153.49 cm^2 area [41]. Other noteworthy solar cells with IBC structure are with efficiencies 24.37% [42] and 22.70% [43] produced by ANU and IMEC, respectively, with an area of 4 cm^2. The former having V_{oc} 702.5 mV, J_{sc} 41.95 mA/cm^2 and FF of 82.70%, the latter V_{oc} 688 mV, J_{sc} 41.50 mA/cm^2 and FF of 79.50%.

1.2.2 Thin-Film Solar Cells

Usually built on a carrier substrate like glass, stainless steel or polymer foils; thin-film solar cells are fabricated from the deposition of various semiconductor materials onto an electric back contact and they are capped with a transparent conductive oxide (TCO) layer on the sunny side (Figure 22). TCO layer is important as it both needs to be highly conductive and highly transparent at the same time. Some methods of processing such layers are; sputtering, low-pressure chemical vapour deposition (LP-CVD), metal-organic chemical vapour deposition (MO-CVD) or atmospheric-pressure chemical vapour deposition (AP-CVD) [5]. As such materials are very thin, nano-textured surfaces are usually necessary to increase photon path length to increase the chance of absorption.

Another type of material that falls under this group is the III-V group cells. They can be used as standalone on some substrate or they can be grown onto various layers by the epitaxy process to make multi-junction solar cells that are capable of absorbing various parts of the solar irradiance.

The third type of thin-film-based solar cells is chalcogenide solar cells that are produced by compounds with at least one anion from group VI (chalcogen) which are consisted of variations of copper, indium, gallium, selenide and sulphide (CIGSS) or cadmium telluride (CdTe) based cells.

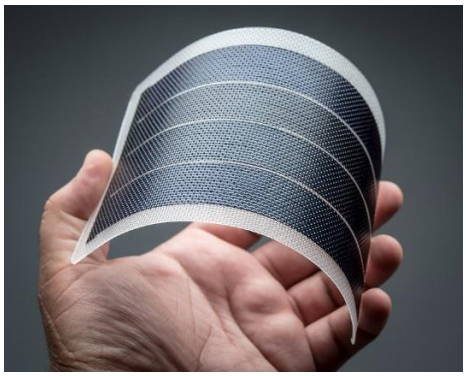

Figure 22 An example of thin-film solar cells (The image is obtained from [44]).

The last type that falls in this group is organic solar cells. Such cells utilise the conductive organic polymers or organic molecules which have carbon as the base, forming various compound structures. Hybrids of organic and inorganic materials are also a possibility. For instance, perovskite and dye-sensitised solar cells are among the research interest of many groups.

1.2.3 New Approaches for Solar Cell Fabrication

The ultimate aim of the solar cell research and development is to fabricate a solar cell with low cost while overcoming the limitation by Shockley-Queisser. The idea of this type of cell is to enhance the shortcomings of single-junction cells by introducing materials or cell structures that can have multiple bandgaps, e.g. multi-junction solar cells that have two or more cells stacked onto one another. They can be used for different irradiance levels as the number of suns increases the efficiency increases.

In general, in single-junction solar cells, one photon creates one electron-hole pair. This can be increased so that one photon excites more than one electron at a time, which can be manipulated by spectral conversion from organic dyes, quantum dots and ions of lanthanides or transition metals. Lastly, photons with lower energy than of the bandgap are not absorbed thus not generating any charge carriers. This problem can be tackled by intermediate band solar cells which utilise special materials, such as quantum dots, to absorb two low-energy photons to excite an electron from the valance band to the intermediate band absorbing the first photon, and then from intermediate band to the conduction band absorbing the second photon.

The efficiency chart of the best solar cells of all types is regularly published by NREL as shown in Figure 23. It is seen that the maximum efficiency (47.1%) is obtained from the cell having multiple junctions under concentrated light. However, in spite of this record efficiency, this type of cell has almost no share in the commercial market due to the high cost. On the other hand, the market share of the c-Si solar cell with an efficiency of 20-24% has exceeded 95%.

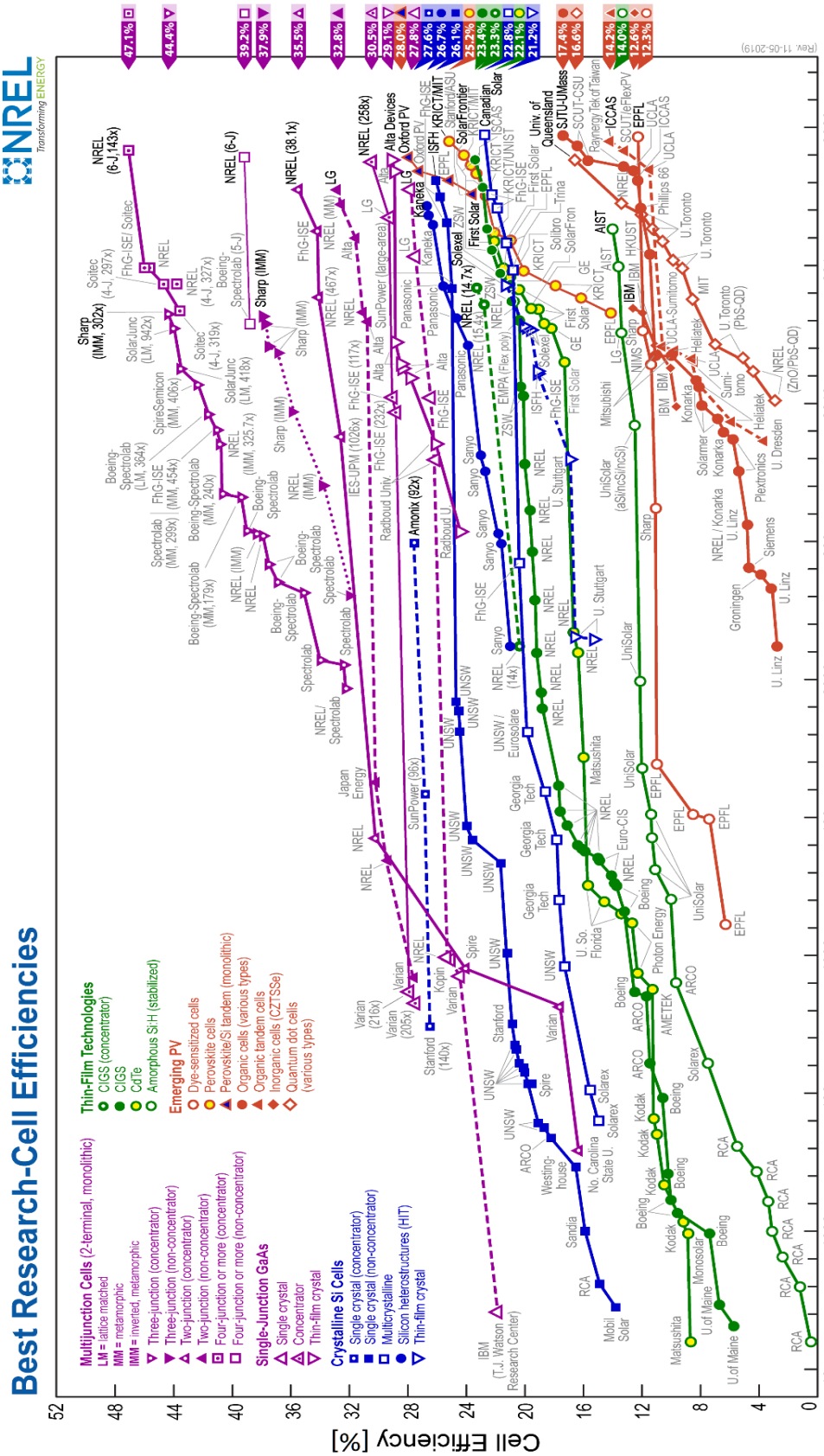

Figure 23 The solar cell efficiency chart of NREL. (Obtained from [45])

CHAPTER 2

BASICS OF CRYSTALLINE SILICON PHOTOVOLTAIC TECHNOLOGY

"The first rule of science, you have to have an interest. Otherwise, you don't deserve to know."

- **Milly Farrier (Dumbo, 2019)**

2.1 Cell Fabrication Steps

In general, a solar cell fabrication process consists of the following steps: texturing, doping, anti-reflective coating deposition and metallisation. This is, however, neither a complete nor fixed list as many research institutes and companies around the world make variations to this schematic by adding, omitting or replacing some steps.

2.1.1 Surface Texturing

One of the fundamental processes involved in solar cells is the texturing of the surface. The texturing, by increasing the path length, allows the solar cell to have a reduced reflection at the surface by redirecting it back into the substrate rather than back into the environment which is also called as light trapping. Usually, potassium hydroxide (KOH) based solutions are used to etch the surface, or other alkaline based solutions which, in general, is used to etch away the damage caused by saw cutting (Figure 24 (a)). This type of etching is dependent on the crystalline orientation, thus results in the formation of pyramids on the surface (Figure 24 (b)), as in one direction, the etch rate is relatively high in comparison to the other orientation. Other additives; such as isopropyl alcohol (IPA) and organic additives; are used to control the structure of the pyramids and their uniformity. The KOH etching occurs with the following equation;

$$Si + 2KOH + H_2O \longrightarrow K_2SiO_3 + 2H_2 \qquad \textit{(Eq. 18) [46]}$$

The generalised etching can be shown with the following reaction equation;

$$Si + 2OH^- + 2H_2O \longrightarrow Si(OH)_4 + H_2$$
$$\longrightarrow SiO_2(OH)_2{}^{2-} + 2H_2 \qquad \textit{(Eq. 19) [47]}$$

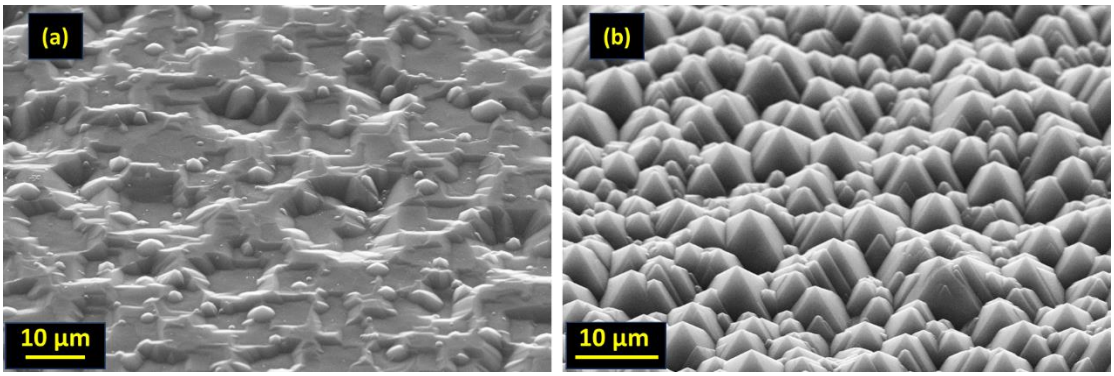

Figure 24 The SEM images of (a) saw-damage etched (SDE) and (b) textured surfaces.

2.1.2. Doping

The conductivity of a semiconductor material can be changed by introducing impurities. For this purpose, boron and phosphorus can be used. When doped with boron the material becomes p-type due to the lack of electrons in the crystal lattice. Aluminium, owing to a valence electron composition similar to boron (Figure 5 (b)), is sometimes used as dopants like in the case of Al-doped BSF at the backside of the standard solar cell. On the other hand, doping with phosphorus adds more (free) electrons to the crystal lattice which becomes n-type. The purpose of doping is to from a p-n junction so that minority charge carriers can be separated from the majority ones by the potential difference at the junction.

There are several methods to dope the substrate. One method is the diffusion of a solid, liquid, or gaseous chemical source in the form of vapour under high temperature, or diffusion of a doped silicon dioxide source. Another one is the ion-implantation followed by an annealing process to activate the dopants and reverse the damage caused by the implantation process. The other method is the use of doping paste.

All these methods have their advantages and disadvantages to one another. For instance, diffusion furnaces (Figure 25) and ion-implanters are very expensive compared to a screen-printer (Figure 29) which is the most common metallisation method for the production of solar cells.

Figure 25 The image of SEMCO furnace with PECVD unit on the right side (red rectangle). On the left side, from top to bottom BCl_3 (orange circle), oxidation (yellow circle) and $POCl_3$ (green circle) furnaces are shown.

Diffusion furnaces and ion-implanters virtually have an infinite source; thus, their doping concentrations can be quite high, in some cases overwhelmingly high to a degree that the solid solubility of the dopant in silicon is exceeded causing unwanted recombination sites. This problem is not viable for a screen-printer as the dopant source is finite but achieving high doping concentrations may also be problematic in return.

In different diffusion furnaces, shown in Figure 25 with orange and green circles, the samples under vacuum are doped with BCl_3 and $POCl_3$ gases with the help of additional reaction gases such as O_2. The following reactions occur inside the furnace that deposits a layer of BSG and PSG, respectively. Then, with the help of low pressure and high temperature, the dopants are diffused in Si. The following reaction equations show the process. The BCl_3 vapour reacts with the oxygen gas and forms a layer of B_2O_3 on the Si wafer surface.

$$4BCl_3 + 3O_2 \longrightarrow 2B_2O_3 + 6Cl_2 \qquad \textit{(Eq. 20) [48]}$$

Afterwards, the formed BSG layer is diffused into Si with the following reaction where elemental B replaces the Si atoms within the lattice.

$$2B_2O_3 + 3Si \longrightarrow 4B + 3SiO_2$$ ***(Eq. 21) [49]***

For $POCl_3$, similar reaction equations exist where P_2O_5 is formed on the surface after reacting with O_2.

$$4POCl_3 + 3O_2 \longrightarrow 2P_2O_5 + 6Cl_2$$ ***(Eq. 22) [50]***

Afterwards, the formed PSG layer is diffused into Si with the following reaction where Si atoms within the lattice are replaced by elemental P atoms.

$$2P_2O_5 + 5Si \longrightarrow 4P + 5SiO_2$$ ***(Eq. 23) [51]***

Theory of Diffusion

The emitter is formed when impurity of opposite polarity to the substrate is diffused into the Si wafer. The introduced impurity changes the electrical properties of the material and thus forms a junction. For the n-type substrate case, an emitter is formed by diffusion of B atoms. The diffusion of an impurity can be mathematically explained by the Fick's laws . The first law states that the flux (J) of the impurities are varied by the change in the concentration and given as;

$$\mathrm{J} = -\mathrm{D}\frac{\partial C(x,t)}{\partial x}$$ ***(Eq. 24) [52]***

where C is the concentration and D is the diffusion constant. The change in the impurity concentration is not only related to the concentration gradient but also related to the time. This can be shown with Fick's second law as;

$$\frac{\partial C(x,t)}{\partial t} = \mathrm{D}\frac{\partial^2 C(x,t)}{\partial x^2}$$ ***(Eq. 25) [52]***

The solutions of Fick's laws with appropriate boundary and initial conditions would give the impurity profiles for various cases such as when the impurity sources are considered as infinite and finite.

For the infinite source case, the initial condition is,

$$C(x,0) = 0$$ ***(Eq. 26) [52]***

And the boundary conditions are,

$$C(0,t) = C_S$$
$$C(\infty,t) = 0 \qquad \textit{(Eq. 27) [52]}$$

where C_S is the surface concentration. Solving the Fick's law (Eq. 25) with these initial and boundary conditions yield the following solution;

$$C(x,t) = C_S erfc\left(\frac{x}{2\sqrt{Dt}}\right) \qquad \textit{(Eq. 28) [52]}$$

where erfc represents the complementary error function. This solution can be used to represent the diffusion furnace process. On the other hand, for processes that have finite dopant sources, such as ion implantation or chemical predeposition, can be represented by changing the boundary conditions as follows;

$$\int_0^\infty C(x,t)\,dx = Q_0$$
$$C(x,\infty) = 0 \qquad \textit{(Eq. 29) [52]}$$

where Q_0 represents the total quantity of impurity. Solving the Fick's law with respect to these boundary conditions and the initial condition given in (Eq. 26 yields a Gaussian distribution.

$$C(x,t) = \frac{Q_0}{\sqrt{\pi Dt}} e^{\left(\frac{-x^2}{4Dt}\right)} \qquad \textit{(Eq. 30) [52]}$$

Both of the solutions can be normalised with respect to a common parameter, as;

$$z = \frac{x}{2\sqrt{Dt}} \qquad \textit{(Eq. 31) [52]}$$

The behaviour of both of the functions with respect to this parameter is shown in Figure 26.

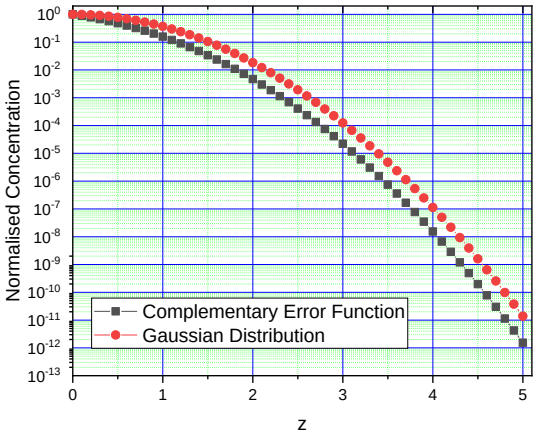

Figure 26 The Gaussian and complementary error function distribution with respect to z.

In a crystal lattice, atoms can occupy one of two positions (Figure 27); substitutional and interstitial. The substitutional atoms are electrically active and thus contribute their free electrons on holes to the Si lattice. On the other hand, the interstitial atoms are not active and after a thermal process, they may be activated which is the process of diffusion. For instance; ion implantation is such a process where high amount of interstitial atoms can be deposited to the lattice that needs to be activated after the implantation process, usually at high temperatures.

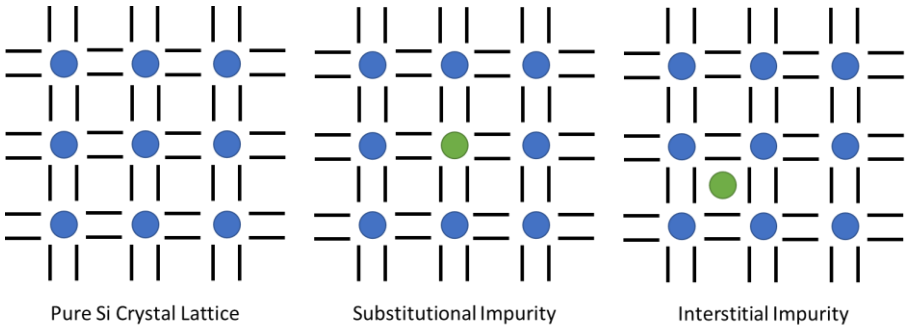

Figure 27 The crystal lattice and impurity positions.

The introduction of impurities into a solid material can occur with one of the three mechanisms (Figure 28). In the vacancy diffusion mechanism, the impurity changes its place with an existing vacancy within the lattice. On the other hand, interstitial diffusion occurs when an electrically inactive impurity moves from one interstitial position to another one. Lastly, the interstitialcy diffusion occurs when a Si atom that is occupying an interstitial position knocks out an impurity atom. This

impurity could then knock out another substitutional Si atom given enough activation energy was transferred from the previous collision.

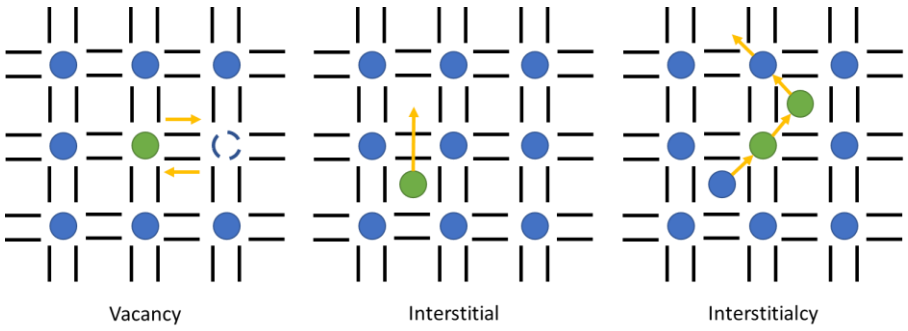

Figure 28 The diffusion mechanisms in solids. Blue atoms represent the Si atoms, green atoms represent the impurities.

Sources for diffusion furnace and the ion-implanter are extremely toxic, corrosive and can ignite very easily, making them unsafe and harder to handle. Because of this, the trade of such materials is (heavily) regulated, both domestically and internationally. The doping paste is safe as long as good ventilation is satisfied. On the other hand, the doping paste is highly susceptible to the temperature variations where it loses its viscosity as the ambient temperature increases. This causes the paste to spread out of the printing design and at the same time; the solvents can evaporate, and thus the paste dries out.

2.1.3 Anti-Reflective Coating (ARC)

Texturing is the first modification done to achieve more generation from the reflected photons. However, it is not enough as the solar spectrum is not uniform. For that reason, anti-reflective coatings must be utilised to best absorb the light from the Sun. ARC layers, silicon nitride (SiN_x), are deposited by plasma-enhanced chemical vapour deposition (PECVD - Figure 25) by using silane (SiH_4) and ammonia (NH_3). Such a layer changes the refractive indices of the surface helping more of the light to converge to the material. SiN_x layers incorporate hydrogen atoms which can reduce the recombination due to defects and impurities. Another importance of hydrogen, especially for p-type wafer-based cells, is the effect on boron-oxygen defects. Such defects reduce the efficiency of the solar cells and hydrogen can be used to stabilise such defects. In the PECVD system, the following reaction occurs leading to deposition of the ARC layer;

$$3SiH_4 + 4NH_3 \longrightarrow Si_3N_4 + H_2 \qquad \textit{(Eq. 32) [53]}$$

The layer deposited in this manner does not usually have the stoichiometry of Si_3N_4, but usually referred to as SiN_x or Si_xN_y:H if large amounts of hydrogen are present. The thickness of the deposited layer is also important to ensure the trapping of a maximum number of photons. This refractive index of the layer and its thickness can be related to one another with the following equation;

$$d_{Layer} = \frac{\lambda_i}{4n_{Layer}} \qquad \textit{(Eq. 33) [54]}$$

where the d_{Layer} indicates the thickness and n_{Layer} indicates the refractive index of the deposited layer. The incident wavelength of the light is shown as λ_i.

2.1.4 Metallisation

The final step of the production of a solar cell is the metallisation. In this step, the contacts that carry the electron from the substrate to the external circuit, are formed by a technique called the screen-printing. A screen-printer, shown in Figure 29, uses pre-designed screens to deposit the intended pattern; such as H-grid Ag and fully covered-Al; onto the surface of the wafer in the form of a paste. Here, the screen design, the paste composition and the squeegee play a major role in the quality of the printed pattern.

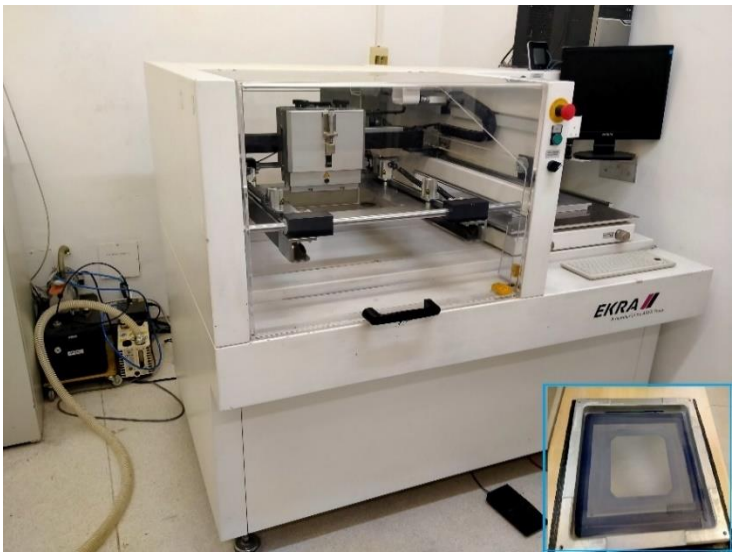

Figure 29 The image of the screen-printer reserved for research at GÜNAM with inset showing an Al-BSF screen on the bottom right corner.

After printing the paste is dried to remove the solvents in a drying furnace (Figure 30). This step plays a crucial role before the firing step, as overdried paste would become ash-like and brittle and will not form proper contact, whereas, under dried paste may release unwanted solvents to the environment.

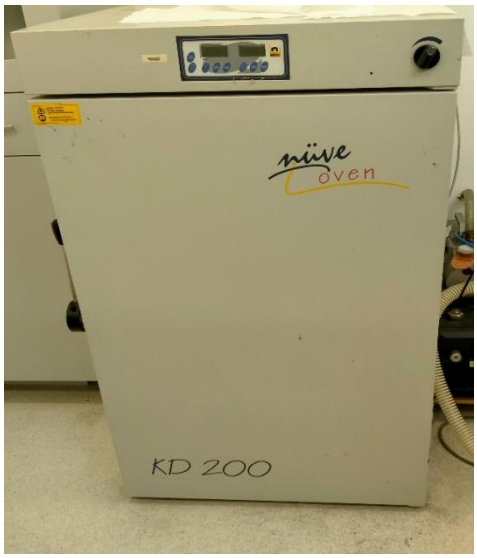

Figure 30 The image of the drying furnace.

Lastly, the wafers are co-fired in a firing furnace (Figure 31) to form eutectic contacts with the respected doped regions.

Figure 31 The image of the firing furnace.

As happens due to the composition of the paste, it can etch through the nitride layer to form Ag contacts with the help of glass frits which is usually used on the front and BSF layer is obtained after this step. On the rear, aluminium paste is used which increases the cell performance; it behaves like p-type doping, reducing minority carrier concentration and increases the voltage.

2.2 Characterisation Techniques

2.2.1 J-V Measurements

The solar simulators use xenon lamps to artificially generate the spectrum of solar irradiance with the help of AM 1.5G filters. The simulators (Figure 32) have two types, flash and continuous illumination. In both cases, a bias voltage applied to the solar cell, with the difference that in continuous measurement the voltage is gradually varied. Then, the behaviour of the solar cell can be traced both with illumination and dark. Without illumination, the solar cell behaves like a diode and has current-voltage curves in first and third quadrants which is called a passive device. On the other hand, under illumination, the curve shifts towards the fourth quadrant and thus; the solar cell generates electricity and is called an active device. From these curves, the open-circuit voltage and the short-circuit current density can be determined which are the interception points of the curve to the x and y axes, shown in Figure 13, respectively. The inverse of the slopes of the curves at V_{oc} and J_{sc} would give the series and the shunt resistance.

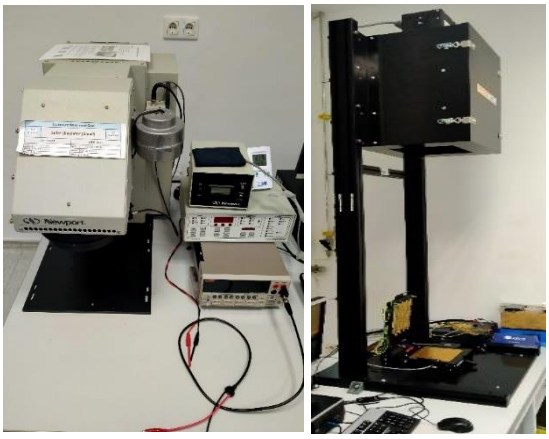

Figure 32 The images of the continuous (left) and flash (right) solar simulators.

2.2.2 Electrochemical Capacitance-Voltage (ECV) Profiling

The ECV profiler is used to determine the concentration of doping which has an indispensable effect on the performance of a solar cell. The ECV can be used on any type of silicon wafer as it is not susceptible to the surface roughness. The capacitance measurements are carried out under constant DC bias on the Schottky contacts with a frequency varied AC voltage superimposed that will give the carrier densities [55]. One critical point of ECV is that it can only measure active dopants within a sample. More general knowledge about the concentration of dopants, whether active or passive, can be obtained from a method called secondary ion mass spectroscopy (SIMS). Both methods have their advantages and disadvantages as such SIMS works better with polished surfaces, ECV, on the other hand, can be used for all surface types. The best approach is to use both methods, especially when the solid solubility limit is of concern.

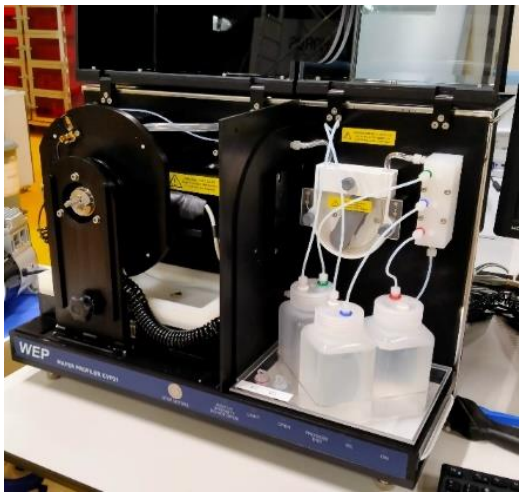

Figure 33 The image of inside the ECV instrument.

2.2.3 Reflection, Transmission, and External Quantum Efficiency (R/T – EQE)

PVE300 setup is capable of measuring reflection, transmission and external quantum efficiency of solar cells as such measurements require the spectrum to be scanned to measure the performance (Figure 34). The source of the system consists of dual xenon – quartz halogen light which can generate a spectrum between 300 to 1800 nm. An integrating sphere is used for the reflectance and transmittance measurements and a temperature-controlled vacuum chuck for spectral responsivity measurements. In order to see the response of the samples to the spectrum, a monochromator is used

to disperse the light into its components with the help of reflection type diffraction gratings.

The integrating sphere is coated with a material called barium sulphate ($BaSO_4$) which is a highly diffusively reflective material at the spectrum range of the instrument. The sphere is used so that, in theory, the light reflected from the sample will be reflected in all directions and detection from any part of the sphere will give the same result.

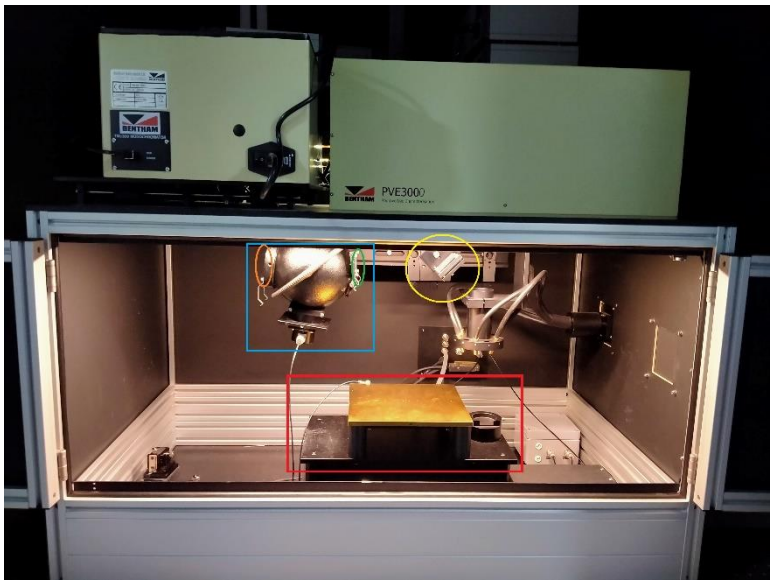

Figure 34 The image of the R/T-EQE instrument. The red rectangle shows the sample stage for the EQE measurements, the yellow circle shows the movable mirror necessary for the diversion of the light source. The blue rectangle contains the integrating sphere with reflectance (orange circle) and transmittance (green circle) ports.

2.2.4 Carrier Lifetime and Suns-V_{oc} Measurements

The carrier lifetime measurements are carried out by Sinton Lifetime Tester (Figure 35). It utilises a high-intensity flash to generate electron-hole pairs within the silicon sample. Then, an inductive coil measures the conductivity of the sample as the flash decays. This is then converted to the minority carrier lifetime, the time it takes for the carrier pairs to recombine. This measurement technique is quick, non-destructive and contactless. It can be used to check the quality of the surface passivating layers and the bulk silicon performance. The change in the

photoconductance (σ in Siemens) of the substrate can be shown with the following relation;

$$q\Delta n(\mu_p + \mu_n)W = \sigma \qquad \textit{(Eq. 34) [56]}$$

where q is the unit charge, Δn is the photogenerated excess carrier density, μ_p and μ_n are the hole and electron mobilities, respectively, and W is the thickness of the substrate.

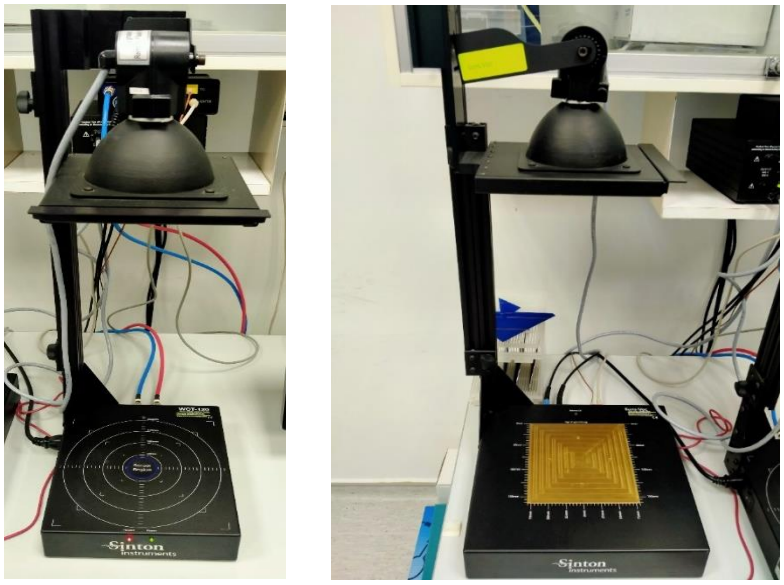

Figure 35 The image of the lifetime measurement instrument (left) and suns-V_{oc} instrument (right).

Suns-V_{oc} measurement is used on the completed cells to assess their performance in the absence of series resistance. Just like the lifetime measurements, a high-intensity flash is used to measure the voltage of the cell as a function of illumination intensity.

2.2.5 Transfer Length Method (TLM)

TLM, shown in Figure 36, can be measured on two different structures, either on a pattern which is specifically made for TLM measurements or on a completed cell where one-centimetre stripes are cut out with equidistant fingers. The method yields contact resistivity, sheet resistance, contact resistance and shunt resistance. One of the key assumptions here is that the fingers formed during metallisation are ohmic in nature.

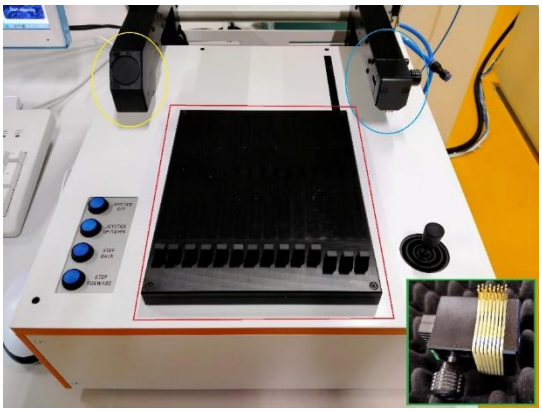

Figure 36 The image of PVTOOLS with TLM chuck (red rectangle), TLM probe (inset – green rectangle), optical microscope (yellow circle) and 4PP (blue circle).

The automated probes measure the J-V characteristics of each finger with respect to one another and their resistance can be extracted. When these resistance values are plotted with respect to the finger separation, extrapolating the line to intercept the resistance axis yields double the contact resistance at zero separation (Figure 37). The slope of the line gives the sheet resistance per stripe (or finger) width.

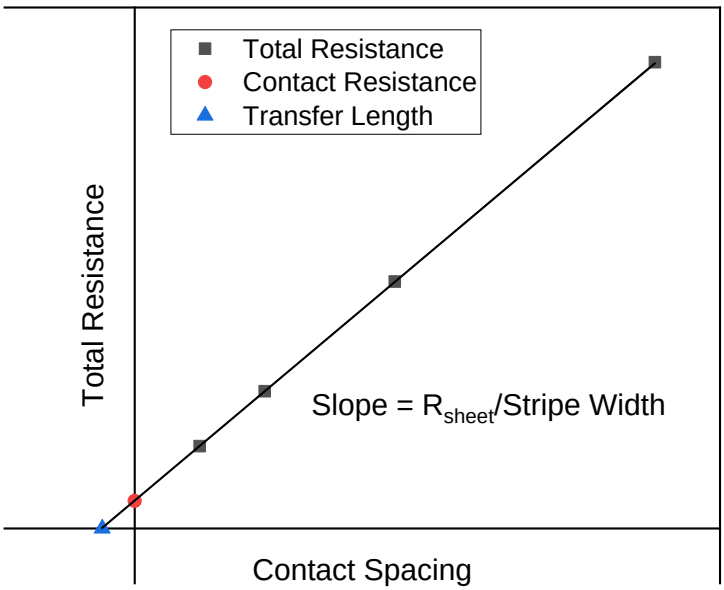

Figure 37 Typical TLM measurement with respect to varying contact spacing. The blue triangle and the red circle show the doubles of the transfer length and the contact resistance, respectively.

2.2.6 Four-Point-Probe (4PP)

The four-point-probe is used to measure the sheet resistance of a conductive layer or the bulk material. The two outer probes pass a current through the sample while the inner two probes measure the voltage and convert it to sheet resistance. The sheet resistance can be calculated using the following equation under the assumptions that the material is not thicker than the 40% of the probe separation (s) and the sample is sufficiency large along the lateral direction [57];

$$R_{Sheet} = \frac{\pi}{\ln(2)} \frac{\Delta V}{I} = 4.53236 \frac{\Delta V}{I} \qquad \textit{(Eq. 35) [57]}$$

This can be used to estimate the doping concentration. As the doping concentration increases the surface becomes more and more conductive, in other words, less resistive.

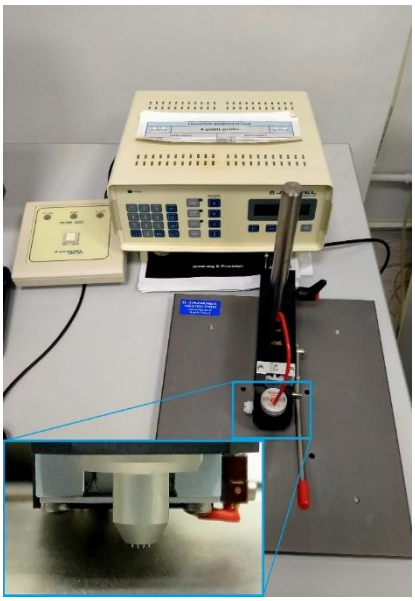

Figure 38 The image of the four-point-probe. The inset shows the probe head.

2.2.7 Scanning Electron Microscopy (SEM)

The SEM device (Figure 39 - ZEISS EVO 15) at GÜNAM laboratory uses lanthanum hexaboride (LaB_6) crystal to thermionically emit electrons which are accelerated and focused through anodes and electromagnetic lenses to image the surface topography, morphology and cross-section of the samples. For that purpose, the secondary electron (SE) detector is used. Other detectors in the SEM are back-

scattered electron (BSE) and energy-dispersive X-ray (EDX). The advantage of SEM to optical microscopy is that higher magnification can be achieved due to electron wavelength.

The image obtained by the SEM measurement is virtual. It is generated after electrons are detected and the result is projected to a screen. As there is no actual colour on the image, the differences are observed through the contrast of the image. For instance, a flat and uniform surface may not generate a contrast, whereas different atomic numbers, like Si, B or P, would contribute different contrasts from backscattering electrons [55]. The secondary electrons are susceptible to the topography changes and the contrast will increase when the sample is tilted from normal incidence.

In our studies, the SEM is utilised to check the morphology of the surface for textured and SDE samples and for pyramid rounding experiments. Another use is for to check the adhesion of the B-paste to various surface morphology types after curing and cross-sectional diffusion depth where possible. Cross-sectional imaging is also used for metallisation samples to check the FT depth of the metal pastes.

Figure 39 The image of the SEM system with EDX detector shown in the blue rectangle.

2.2.8 Photoluminescence (PL)

Photoluminescence is used to determine the electrical and optical properties of materials (Figure *40*). For silicon materials, it is utilised to observe carrier lifetime, emitter saturation current and implied open-circuit voltage, as PL is capable of exciting the impurities within a silicon wafer (Figure 11). This method can be used throughout the process flow and yields a two-dimensional image of the wafer. It is a non-invasive method that works both on unfinished and finished cells and has high image quality compared to electroluminescence which is a measurement technique where only a finished cell can be measured with a low-quality image.

The principle of photoluminescence is that when photons with energies higher than the bandgap energy are used, the electrons are further excited into the conductance band where they non-radiatively decay back to the edge of the conduction band and are trapped by the trap states. A singlet-singlet or singlet-triplet relaxation like this would emit a photon which can be detected and converted into various aforementioned parameters.

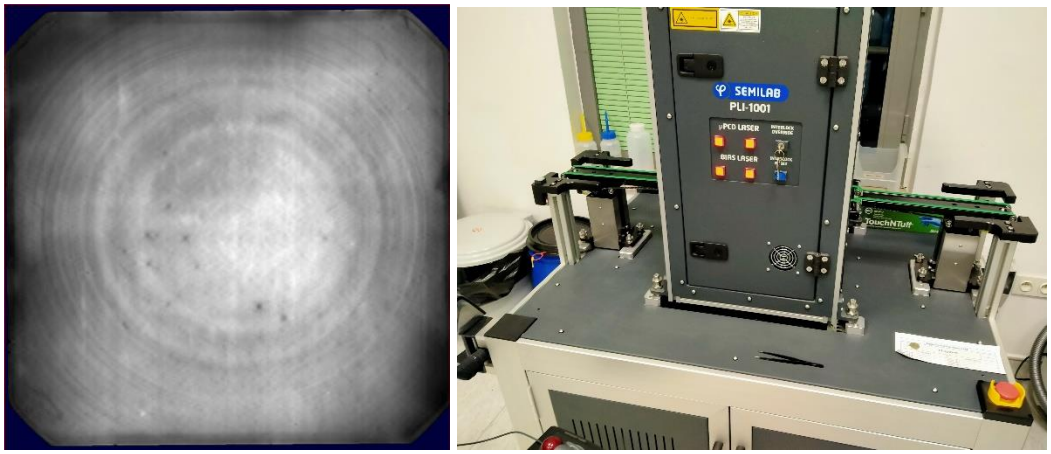

Figure* 40 *The image of the sample (left) measured with the PL instrument (right).

2.2.9 Optical Microscope

The optical microscope (Nikon ECLIPSE LV100D - Figure 41) is used for a quick check of the surface coverage of the screen-printed boron doping paste after drying. The microscope uses the reflected light from the surface to image. It allows magnifications up to 1000 times of the sample.

Figure 41 The image of the reflected light microscope.

2.2.10 Profilometer

Dektak stylus profiler (Figure 42) can be used to measure the thickness and height of screen-printed fingers and busbars. The setup has a fine tip needle that tracks along the surface and plots the height of the surface with respect to the distance traced. Other exemplary applications of Dektak could be listed as measuring of the thickness of thin films up to 10 nm, stress and surface roughness.

Figure 42 The image of the profilometer.

2.2.11 Ellipsometry

This method (Figure 43) uses polarised light to measure the thickness of dielectric films on a substrate, line width, and optical constants of films or substrates [55]. The light is then reflected from the surface of the substrate and reflected towards a detector on the other end. The detector, coupled with an analyser, measures the

variation in the light intensity and polarisation. The light source and the detector are placed at a substrate-specific angle to ensure that the light is reflected from its surface which is 70° for Si.

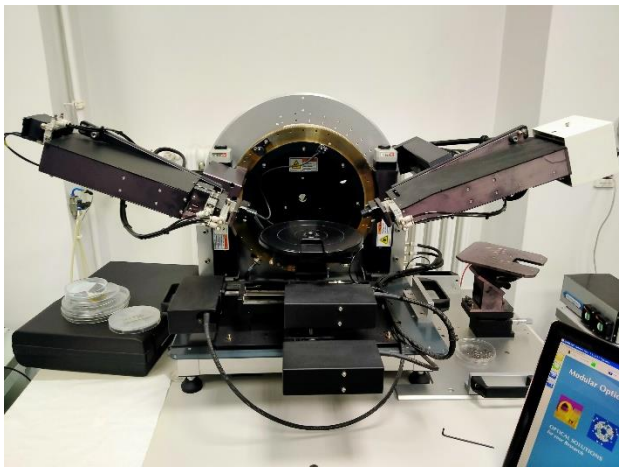

Figure 43 The image of the ellipsometry system.

CHAPTER 3

EXPERIMENTAL DETAILS

"If we knew what it was we were doing, it would not be called research, would it?"

- **Albert Einstein**

3.1 Previously Optimised Process Steps

The following steps have been optimised in GÜNAM labs and have been utilised in the processes mentioned throughout this chapter. Some of which may have been altered to accommodate the necessities of the processed cells.

3.1.1 Texturing

The sample texturing is applied in a 4% KOH solution with AlkaTex to achieve small size random pyramid structures on both surfaces of the wafers. Temperatures around 75 – 80°C is applied. N_2 gas is used as a stirring agent to ensure uniform temperature distribution and etching. Following the texturing, standard RCA-1 and RCA-2 are applied to remove the organic residue due to Alkatex and alkaline residue due to KOH.

3.1.2 $POCl_3$ Diffusion

Liquid $POCl_3$ is carried by the N_2 gas into a high-vacuum chamber as a gas in which the phosphorus atoms are diffused onto the both surfaces of the wafers. Single side diffusion can be applied by using a barrier layer like silicon nitride or silicon oxide to protect one side of the wafer while doping the other side. At GÜNAM labs this diffusion is carried out at 840°C.

3.1.3 Oxidation

Oxidation is used to passivate the doped regions. Both dry and wet oxidation can be applied. Former requires oxygen to be injected into the furnace or a mixture of O_2 and H_2 which is burnt to produce H_2O that is then deposited under vacuum. For the

latter, water is boiled and carried into the furnace with the help of nitrogen flow which is applied under atmospheric pressure.

3.1.4 SiN_x as ARC

Before metallisation, a silicon nitride layer is coated on both surfaces that acts as an ARC. Under low vacuum, this layer is deposited by the method called plasma-enhanced chemical vapour deposition (PECVD).

3.1.5 Etch Resist

The etch resist is used as a protective layer against acidic etching solutions to pattern the desired doping region onto the surface of the wafer. It is screen-printed onto the surface and dried in a stack furnace.

3.2 Boron Doping Paste

In order to control the doping profile of the boron paste, two sets of experiments have been designed. First one has concentrated on the annealing parameters of the paste whereas the second set of experiments has focused on the optimisation of the printing parameters for the paste.

3.2.1 First Set of Optimisations for the Annealing Step on SDE Wafers

This set focuses on the effects of annealing temperature, environment and duration (Table 1) on the doping profile of the paste. Boron doping paste was printed on 156x156 mm^2, n-type SDE wafers with printing speed of 200 mm/s and squeegee force of 48 N. The samples are then dried in a belt furnace at a peak temperature of 490°C with the belt speed of 480 cm/min. Dried samples are then broken apart into smaller pieces which went through an annealing step with temperatures varying from 800°C to 950°C with intervals of 50°C, in an environment of pure nitrogen gas (120 sccm) and mixture of nitrogen-oxygen gas (120-30 sccm and 20-5 sccm), and durations ranging from 30 minutes to 120 minutes in intervals of 30 minutes. Afterwards, the samples are dipped in HF to remove the borosilicate glass (BSG) layer. After the removal of the BSG layer and RCA cleanings, the samples went through sheet resistance mapping on the p^+ side to relate the doping concentrations to the sheet resistance values, and rear sides were also checked for auto-doping where boron source may degas during the gas phase of the doping and dope the neighbouring

wafer during the annealing step in the furnace [58]. Implied V_{oc} measurements were also carried out on the samples as a quality check in between HP dips and RCA cleanings.

Table 1 The parameters used for the annealing of the doping paste.

Temperature	**800°C**	**850°C**	**900°C**	**950°C**
Environment	**High (120 sccm) N_2 Flow** **High N_2 (120 sccm) + O_2 (30 sccm) Flow** **Low N_2 (20 sccm) + O_2 (5 sccm) Flow**			
Duration	**30 Mins**	**60 Mins**	**90 Mins**	**120 Mins**

The printed samples are separated here so that one set can be used to profile the doping concentration with ECV while the other set can be used for TLM and J-V measurements. TLM and J-V sets were prepared in such a way that they were coated with SiN_x on the boron paste printed side where the SiN_x layer acts as a diffusion barrier and then diffused with $POCl_3$ on the opposite side to form $p^+/n/n^+$ structure. Then the samples are cut in half with the help of a laser to form different contact structures as shown in Figure 44. Cut pieces are Al or Ag evaporated to form spreading TLM patterns on one surface and on the other surface Ag or Al evaporated to form contacts for J-V measurements (Figure 44).

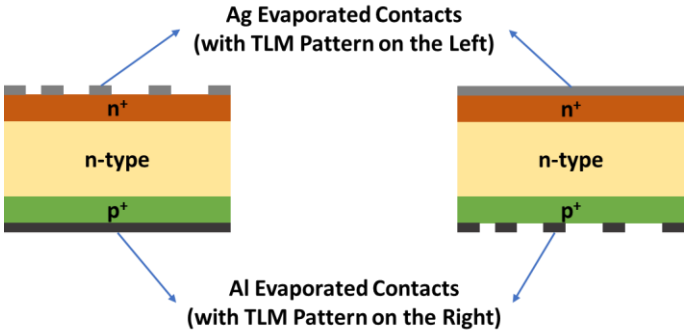

Figure 44 The TLM and J-V design of the annealing step.

3.2.2 Second Set of Optimisations for the Printing and Drying Parameters for Polished (SDE) Wafers

This set was designed to observe the effects of the screen-printer parameters on the printing quality and the effects of belt furnace drying on the adhesiveness of the paste to the surface as well the doping concentration for polished wafers. As for the experimental parameters (Table 2), the printing force was kept constant and both the printing speed for printing quality and the belt speed for the drying process were changed. The former was to ensure the complete surface coverage of the paste which was an encountered problem in the previous sets where bubbles would form on the surface, and the latter was to speed up the drying process. The dried samples were annealed in high N_2 flow for 100 minutes at 950°C.

Table 2 The parameters used for the printing and drying trials of the doping paste.

Printing Parameters	**Printing Speed**	**10 mm/s**	**60 mm/s**	**200 mm/s**
	Printing Force	**64 N**		
Drying Parameters	**Temperature**	**430°C**	**450°C**	**600°C**
	Belt Speed	**50 cm/min**	**100 cm/min**	**150 cm/min**

3.3 Pyramid Rounding Studies

After the observation of the failure of the paste adhering to textured surfaces, confirmed first by visual inspection, then with SEM images (Figure 45) and following the correspondence with Merck, the company that produced the B-paste, it was decided that pyramid rounding could help reduce the problem. For that reason, a set of experiments utilising chemical etching to smoothen the pyramids were designed using a mixture of hydrofluoric acid (HF), nitric acid (HNO_3) and water (H_2O). The working principle of this etching is first by oxidising the surface with nitric acid with the following reaction;

$$Si + 2NO_2 + 2H_2O \rightarrow SiO_2 + H_2 + 2\,HNO_2$$ ***(Eq. 36) [53]***

The nitric acid in its liquid form partially decomposes into nitrogen dioxide (NO_2) under heat or light illumination with the following reaction;

$$4HNO_3 \leftrightharpoons 4NO_2 + 2H_2O + O_2$$ ***(Eq. 37) [59]***

The formed SiO_2 in (Eq. 36) is etched away by HF as;

$$SiO_2 + 6HF \rightarrow H_2SiF_6 + 2\,H_2O$$ ***(Eq. 38) [53]***

The overall reaction can be written as;

$$Si + HNO_3 + 6HF \rightarrow H_2SiF_6 + HNO_2 + H_2O + H_2$$ ***(Eq. 39) [53]***

The resulting hexafluorosilicic acid (H_2SiF_6) is stable in water. In the (Eq. 37) and (Eq. 39) O_2 and H_2 gases are released, respectively, and this causes bubbling around the samples. The bubbles can be removed by moving the samples around in the mixture, from time to time.

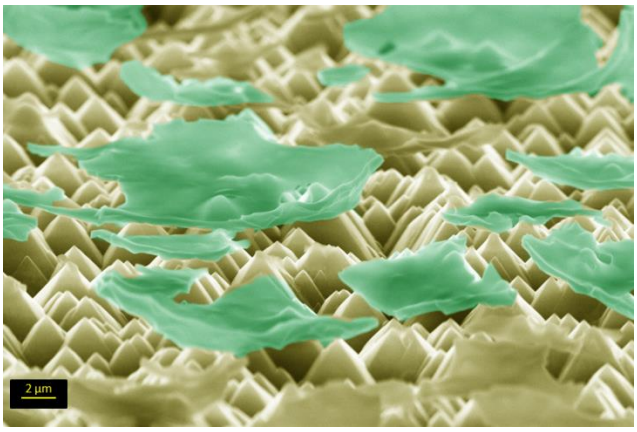

Figure 45 The SEM image of B-paste floating on a textured surface. The image is coloured to show paste flakes.

3.3.1 First Set of Rounding Studies

On the first set (Table 3), the HF amount was kept constant, while HNO_3 and H_2O amounts were varied with respect to duration so that controllability of the etching can be observed with respect to reflection. The n-type, KOH textured samples, small in area (9 cm^2), were immersed into acidic solutions of various chemical compositions to test the single side etching under different durations (Figure 46). The samples were rinsed with deionised water to stop the etching process and dried with a nitrogen gun.

Then, the reflectance of the samples and two references, SDE and textured, was measured, in the range of 300 – 1200 nm. The surface morphology was also checked with an optical microscope as well as SEM imaging.

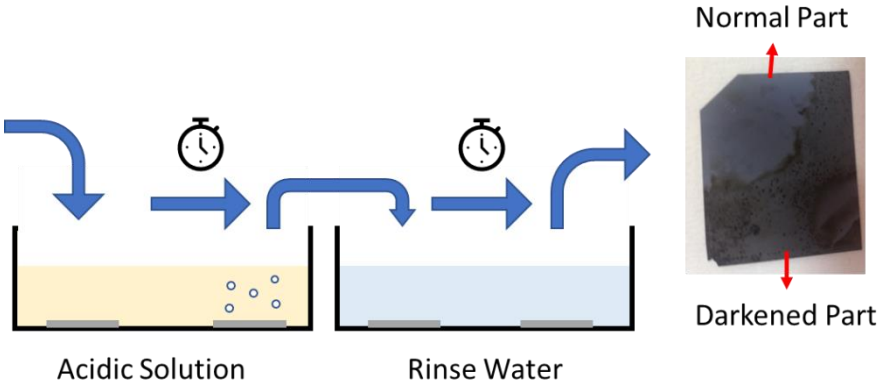

Figure 46 The rounding process with an example of the results.

3.3.2 Second Set of Rounding Studies

The second set (Table 3) focuses more on the consumption of the HNO_3 by reducing its amount, keeping the HF fixed and varying H_2O amount to check the effect of water on the etch rate, as well as the controllability of the etching under varied durations. The reflectance of n-Cz small size samples along with references of textured and SDE wafers was measured and the surface morphology was examined using SEM.

3.3.3 Final Set of Rounding Studies

On the final set (Table 3), all concentrations were kept the same while the duration is varied. This time, the samples included full-size p- and n-type wafers.

Table 3 The pyramid rounding parameters.

	First Set	Second Set	Final Set
38% HF [ml]	**1**	**1**	**1**
65% HNO_3 [ml]	**5, 10**	**5**	**10**
H_2O [ml]	**0, 1, 5, 10**	**1, 5**	**10**
Duration [Sec]	**10 - 60, 90, 120**	**60 - 100**	**25 – 45 75, 90, 150**

Also, some of the samples originally produced in the first and second sets underwent a secondary rounding procedure in this set to check whether changing the etchant concentration would have a better effect on rounding profile or not, would it affect the etching orientation differently. Lastly, in this set, samples that have regionally darkened (Figure 46) during previous sets have been dipped in HF to see if recovery is possible. This darkening occurred on both types of samples along with bubbling, especially on p-type wafers, due to the etching in an acidic solution. The samples were measured for their reflectance and imaged with SEM to check the morphology.

3.4 Final Set of Optimisations

The results of previous optimisation sets (Table 4) were used to produce bifacial and IBC cells that utilise boron doping paste instead of conventional furnace-based boron diffusion or ion-implanter.

Table 4 The best results obtained from previous studies that have been used for the manufacturing of bifacial and IBC solar cells.

Rounding Parameters
Ratios: [1] HF : [10] HNO_3 : [10] H_2O **Duration: 75 seconds for n-type, 90 seconds for p-type**
Printing Parameters
Speed: 10 mm/sec **Force: 64 N**
Drying Parameters
Temperature: 200°C **Duration: 10 minutes**
Annealing Parameters
Temperature: 950°C **Environment: High N_2 (120 sccm) flow** **Duration: 90 and 120 minutes**

3.4.1 Small-Size Bifacial Cells

The n- and p-bifacial cells (Figure 47), were manufactured following the process flow shown in Figure 48.

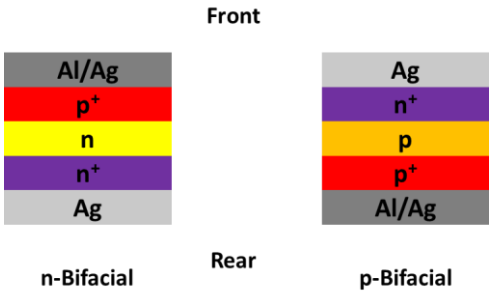

Figure 47 Basic structure of the bifacial cells. Contacts are shown as bulk, instead of a grid.

SDE, textured and pyramid wafers of both p- and n-types where boron paste will be printed on are coated with a SiN_x layer in a PECVD system to prevent phosphorus doping to diffuse on that side of the wafer. This change in the conventional process flow, conventional being the diffusion of boron as a first step, was done to prevent phosphorus diffusion to nullify the effect of boron doping, as boron paste is a finite doping source whereas $POCl_3$ is infinite. The full-size samples were then dipped in an HF-HCl mixture to strip away the protective SiN_x layer to reveal undoped side. Afterwards, the boron paste was screen-printed on the wafers using the printing parameters investigated in earlier studies. The paste was dried in a furnace for 10 minutes at 200°C. Then, the samples were cut by a laser into smaller chunks of an area around 25 cm^2. The smaller size samples were annealed in an atmospheric tube furnace, using the best two results of the annealing step studies. Before annealing, from the sub-cells reserved for ECV measurements, a sub-sample for SEM imaging was taken to observe the dried boron paste layer.

After the annealing step, the samples were RCA cleaned. Following the cleaning process, the ECV measurements were carried out, as well as detailed sheet resistance mapping, photoluminescence (PL) and implied V_{oc} measurements on both sides of the wafers. After the cleaning an oxidation process to passivate both the p- and n-layers was applied. Another set of photoluminescence and implied V_{oc} measurements on both sides were carrier out to observe the effects of passivation.

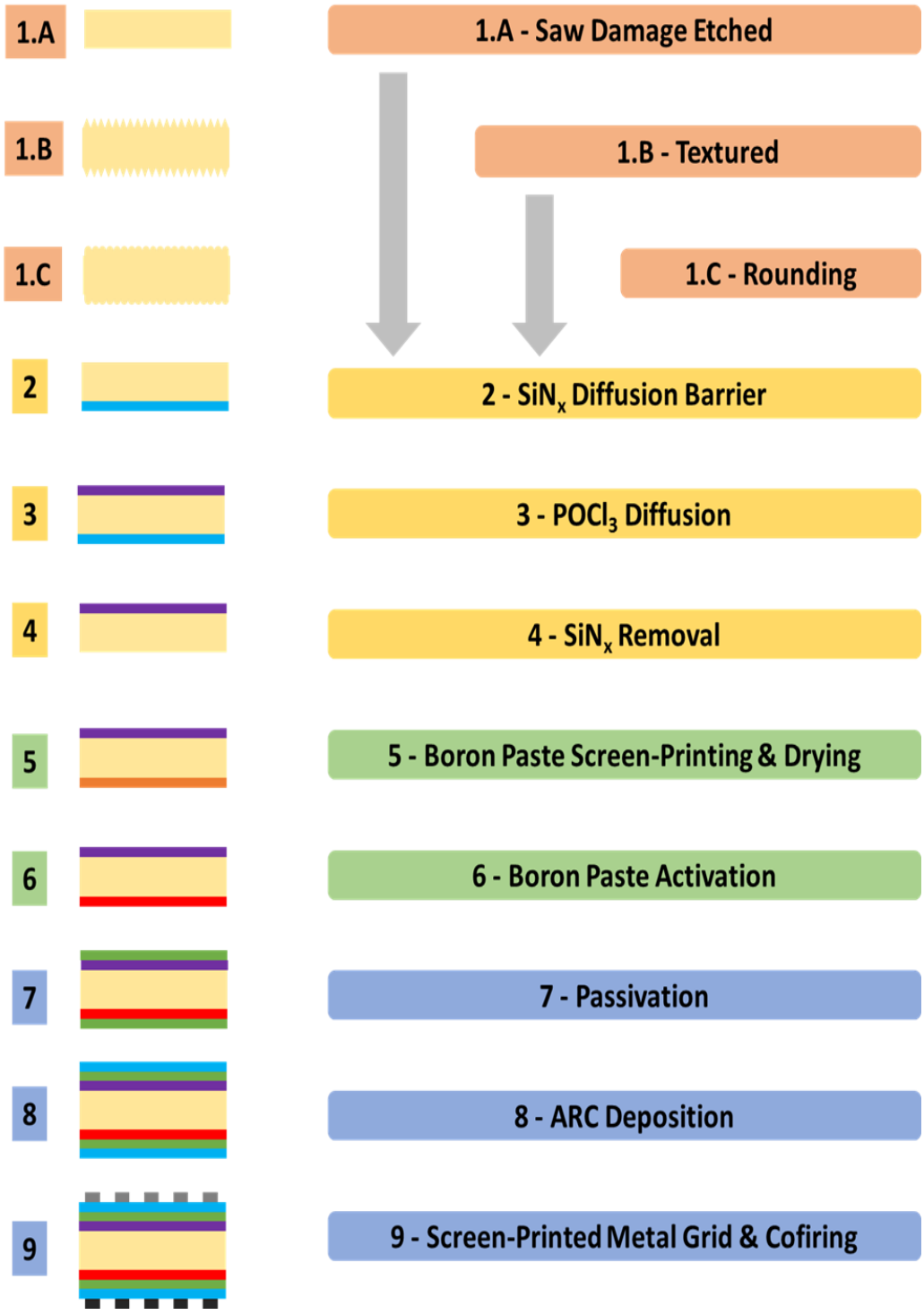

Figure 48 The process flow of small-size bifacial cells.

Before the metallisation step, the samples were PECVD coated with SiN_x on both sides to form ARC layer. Another set of PL and iV_{oc} measurements on both sides were carried out to check for the quality of the ARC layer.

Lastly, the H-grid pattern was printed on both sides of the cells with appropriate fire-through (FT) metallisation pastes which were then dried in a furnace and co-fired in a belt furnace at various temperatures. To finish up, the performance of the completed cells was measured using the solar simulator on both sides. Also, PL, Suns-V_{oc} and TLM measurements were carried out on both sides of the finished cells, as well.

3.4.2 IBC Cells

The best results obtained in the small-size bifacial studies were also used on the production of small size IBC cells with the given process flow in Figure 49. In order to form the n^+ region on the rear side of the wafers, a Si-rich SiN_x layer with the thickness of 120-140 nm was deposited on the rear side of the wafer as a diffusion barrier. Afterwards, on top of the nitride layer, a layer of etch resist was screen-printed. The wafers were dipped into HF to remove the nitride layer through the openings of the etch resist layer to reveal the doping region. The samples went through $POCl_3$ diffusion on p-type and n-type wafers which form the front floating emitter (FFE) and front surface field (FSF), respectively, and the n^+ region on the rear for both types. FFE was etched back to increase the emitter sheet resistance with TMAH. The sheet resistance of both the FSF and FFE has been checked after the diffusion and after the etch-back step.

After the diffusion step, the SiN_x was completely removed to allow screen printing of the boron paste. The paste was activated by the best result of the aforementioned annealing step. The doping profiles of both dopants have been checked using ECV and 4PP, also with PL and iVoc the process quality. RCA cleaned samples then went through an oxidation step to passivate the samples on both sides and an ARC on both sides was deposited by PECVD and after each step; the samples were quality checked with PL and iV_{oc} on both sides. Then, both contact metals were screen-printed on the rear side for the appropriate polarities and then co-fired using the belt furnace with the best results obtained from the small-size bifacial studies. As

a last step of production, the samples were edge isolated, from full-size to 16 cm^2, to remove shunting problems. The cells were then measured for J-V, PL, Suns-V_{oc}, as well as EQE on selected cells.

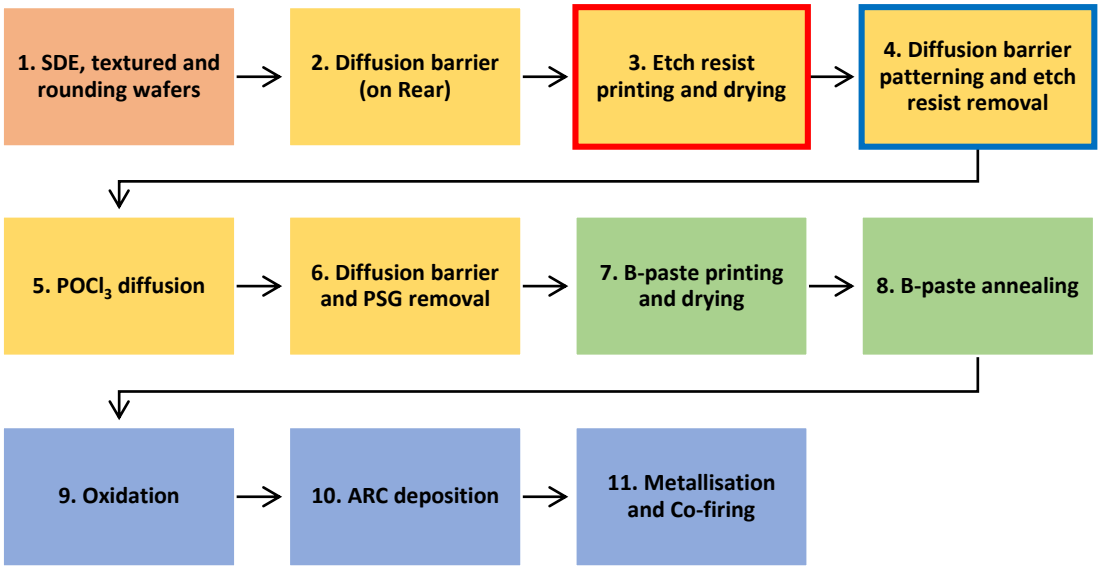

Figure 49 The process flow of IBC solar cells. The red outlined box shows the additional screen-printing step and the blue outlined box shows additional HF dip step.

.

CHAPTER 4

RESULTS AND DISCUSSION

"I have no doubt that we will be successful in harnessing the sun's energy… If sunbeams were weapons of war, we would have had solar energy centuries ago."

- Sir George Porter (1920-2002)

4.1 Previously Optimised Process Steps

In Figure 50, cross-section of a pyramid textured Si is shown with an average pyramid height of 4.3 μm. This texturing recipe is used at GÜNAM laboratories for various cell process steps, among which a record efficiency of 19.23% has been achieved on Al-BSF solar cells.

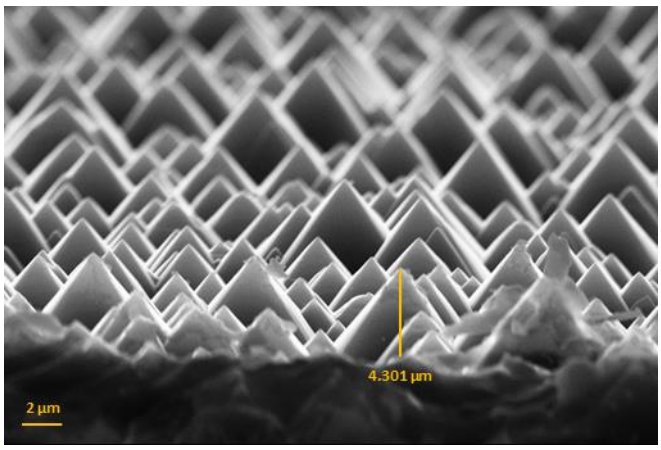

Figure 50 The SEM image of the textured surface. The marked pyramid shows an average pyramid height of 4.3 μm.

A textured silicon wafer without ARC has a 12.56% weighted average reflection in comparison to an SDE wafer with 33.80% in 400-1100 nm range and the corresponding reflection spectrum is shown in Figure 51. This reduction in the reflectance after texturing is one of the key optical gains in cell efficiency based on light trapping.

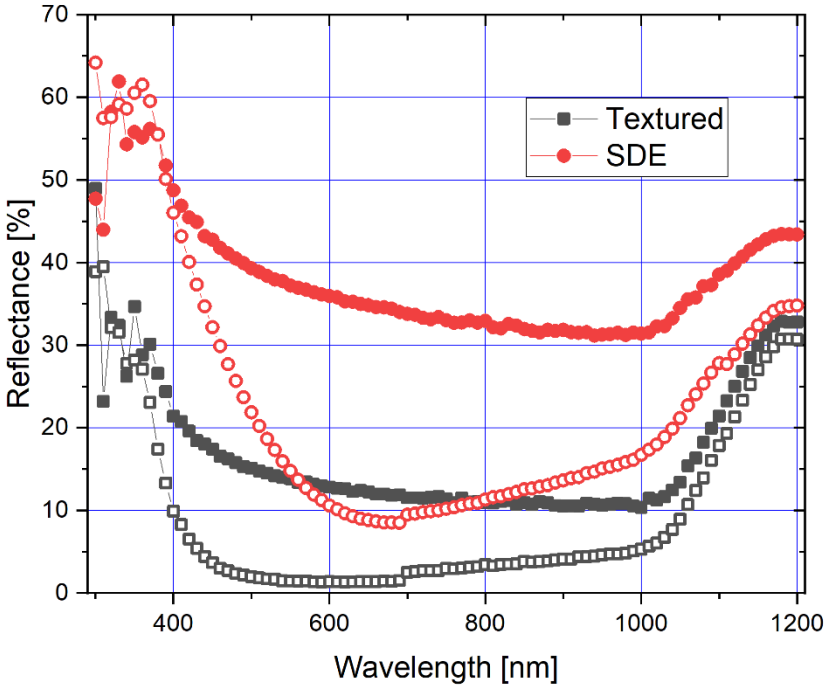

Figure 51 The reflectance of textured and SDE wafers before and after ARC layer deposition. Hollow symbols show the reflectance after nitride deposition.

After texturing, diffusion is the following key process step in the cell fabrication process.

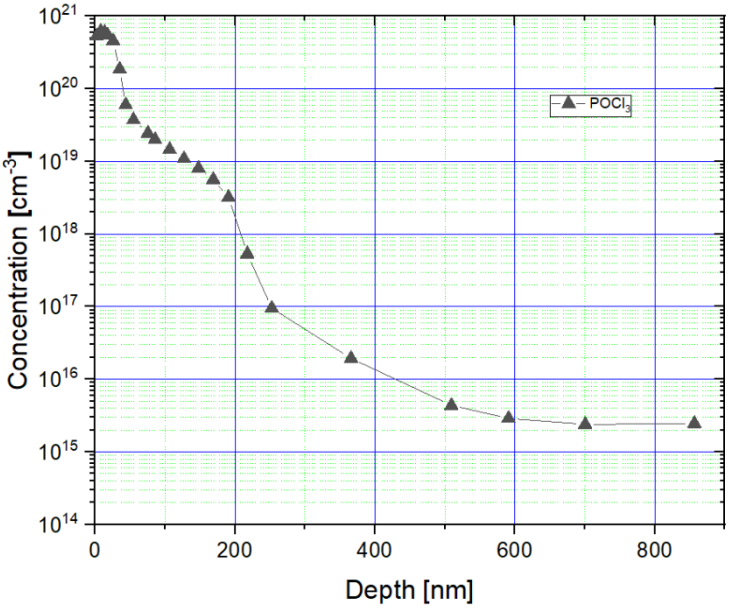

Figure 52 The typical concentration profile of $POCl_3$ diffusion measured by ECV used in produced solar cells.

Considering the ECV profile given in Figure 52, currently optimized $POCl_3$ diffusion recipe at GÜNAM laboratories has a peak doping concentration of $7x10^{20}$

cm^{-3} with a junction depth of around 500 nm. The corresponding sheet resistance for this recipe is 60 Ω/□ on 1-10 Ω.cm, textured, p-Cz wafers. During bifacial cell processes, the same recipe was applied on wafers with diffusion barrier at one side to end up with single side doping. For the case of IBC cell processes, the same diffusion barrier having 120-130 nm thick SiN_x layer was applied at the rear side of the wafers and then patterned for the corresponding diffusion process. Depending on the substrate type, the diffusion barrier was patterned either for emitter or for BSF region prior to $POCl_3$ diffusion. With the help of ECV and sheet resistance measurements, it has been confirmed that the regions lying under the SiN_x layer are well protected while the open regions are doped during $POCl_3$ diffusion processes.

As a passivation layer, 4-5 nm oxide layer was grown on the samples in a reduced pressure furnace at 850°C for 40 minutes on both sides. The grown SiO_2 was capped with a SiN_x layer acting as an ARC. The weighted average reflectance of this ARC layer is 4.73% for a textured surface and 16.27% for the SDE surface with the corresponding reflection spectrum shown in Figure 51.

4.2 Boron Doping Paste

The results of the boron doping paste on SDE and textured wafers are given in this section. Before an experimental matrix was designed, the screen-printer was checked if it were possible to print the paste or not. For that purpose, a full-size Al screen has been used to provide the designated screen for the paste applications, regarding paste optimisation and bifacial applications.

4.2.1 First Set of Optimisations for the Annealing Step on SDE Wafers

Before going through the results, it is worth mentioning that the Al screen would cause bubbling on the surface after the snap-off. After a very short time, the bubbles would burst due to the weight of the paste and its low viscosity and form small rings. The rings would eventually close off; however, this would also mean that if a pattern were to be applied, its resolution would not be the desired one, considering the real purpose of the B-paste, for IBC doping pattering. These small rings, would still be clearly visible after diffusion and barely visible after HF dip to remove the BSG, as shown in Figure 53. To prevent the bursting of the bubbles the samples were cured

as soon as they were printed. However, the airflow in the dryer to satisfy uniform heating would burst the bubbles anyway. At first thought, the expectation was that the bubble formation would affect the doping profile poorly, as those regions looked uncovered. The decision at that point was to address this issue with another experimental matrix (Table 2) that focuses on improving the printing quality and remove the bubble formation which follows right after this subsection.

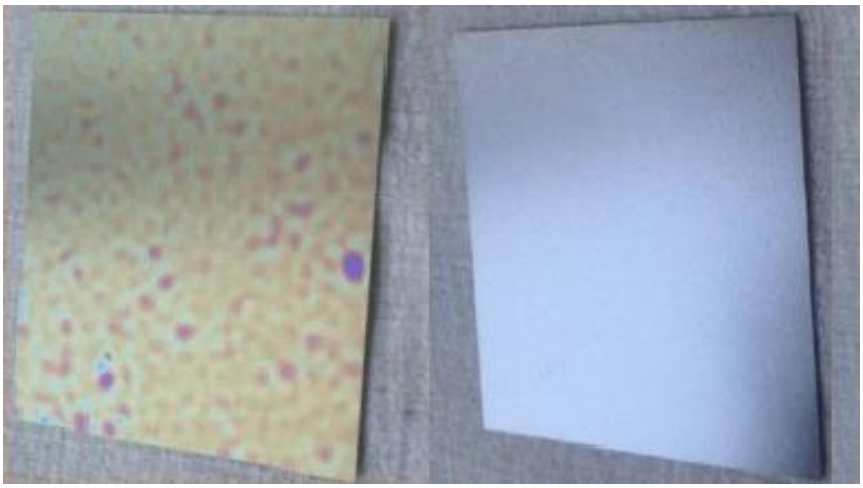

Figure 53 The images of the annealed B-paste before (left) and after (right) HF dip to remove BSG.

After activating the B-paste, it was observed that the surface would diffract the light as a thin soap bubble. As the annealing temperature increased the rings would become darker with a mixture of blue and pink and right outside the contour throughout the surface a faint yellow. To check the hypothesis that rings could distort the doping profile, four-point-probe measurements were carried out on and around the rings and regular mapping (3 by 3 on B-paste side and two on the rear side) of the surface. The size of the rings were too small compared to the probe head to be sure of the results of the measurements but, the samples yielded uniform sheet resistance values on the surface, on and around the rings. The rear side measurements were carried out to check if auto-doping [58] occurred between two successive samples then it was realised that there was no such effect occurring during activation. Absence of auto-doping was also verified by ECV measurements of the rear side on randomly selected samples.

The aforementioned matrix in Table 1 was used to print full-size B-paste samples then they were cut into smaller pieces and used for activation optimization studies. The results of the doping profiles under high nitrogen flow rate are shown in Figure 54. The low-temperature diffusion, at 800°C, was insufficient to diffuse the boron paste into the silicon substrate deep enough and rather would form a highly resistive layer that would prevent the ECV tool to measure it. Although the formed BSG layer was removed with an HF dip, this highly resistive layer would still be present, suggesting a very shallow and dense layer. This measurement problem was also observed for the samples annealed at 850°C for 90 minutes, but not on the other samples annealed at the same temperature and could be due to the poor removal of the BSG layer. At 850°C, the 4PP mapping has shown high sheet resistance values with high nonuniformity. This implied that the diffusion temperature and duration were not sufficient enough for a uniform doping. The best doping profiles were achieved with the annealing temperature of 950°C for 90 and 120 minutes. For this temperature, as the annealing duration was increased both the sheet resistance, the nonuniformity decreased accordingly. Although the samples were prepared on wafers from the same batch, the profiles showed slight concentration variations for the substrate concentration.

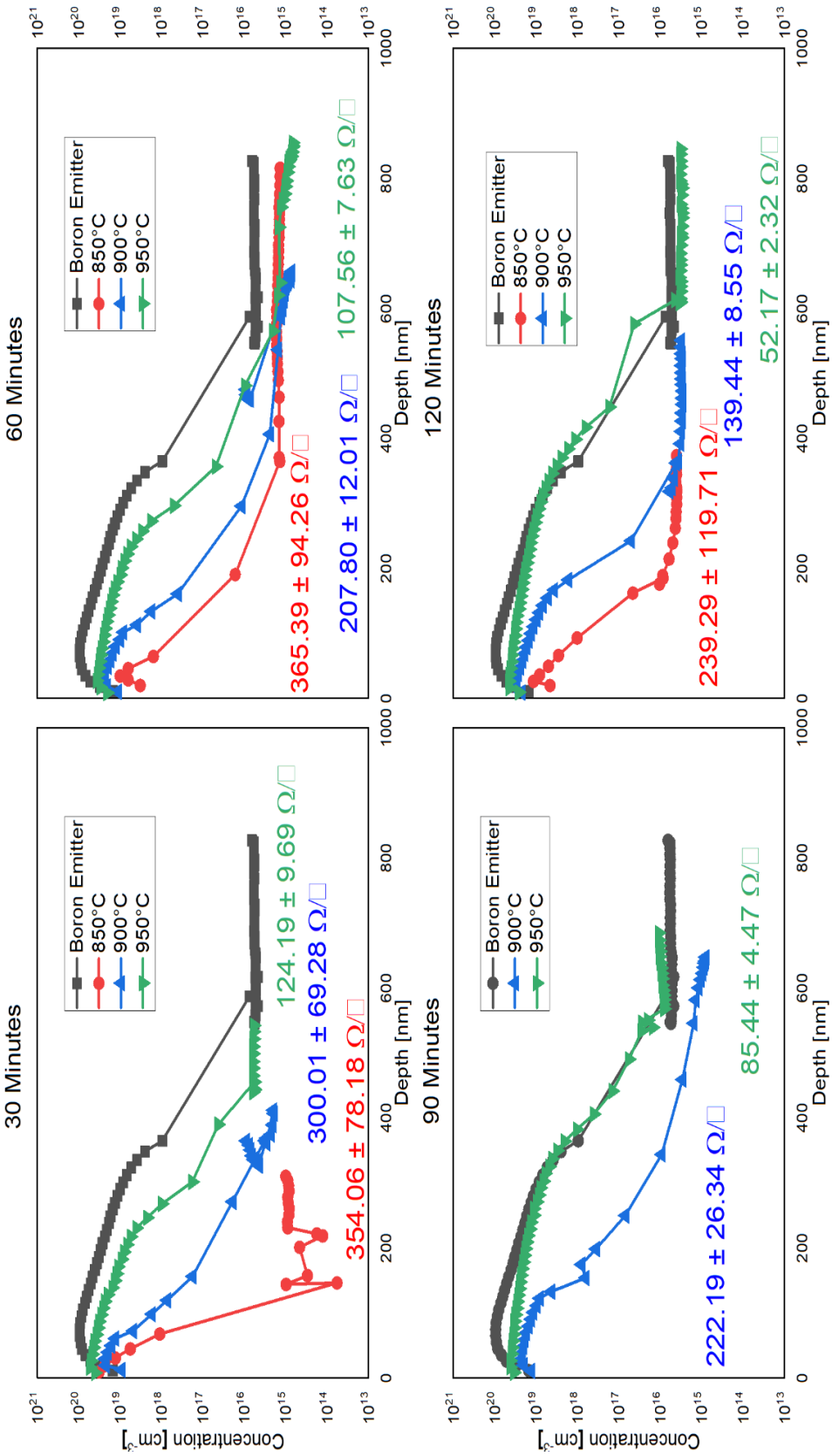

Figure 54 The ECV and 4PP results of annealing trials under high N_2 (120 sccm) flow.

As shown in Table 1, the effect of O_2 addition to the annealing gas mixture was tested. Addition of O_2 was expected to change the composition of the BSG layer and thus change the boron concentration at the surface. In order to reduce the O_2 consumption, the flow rates of N_2 and O_2 were lowered with the same ratio as in the previous set and their effect on doping profiles was tested with a fixed annealing temperature of 900°C and duration of 60 minutes while varying the environment. The ECV results of these trials are shown in Figure 55.

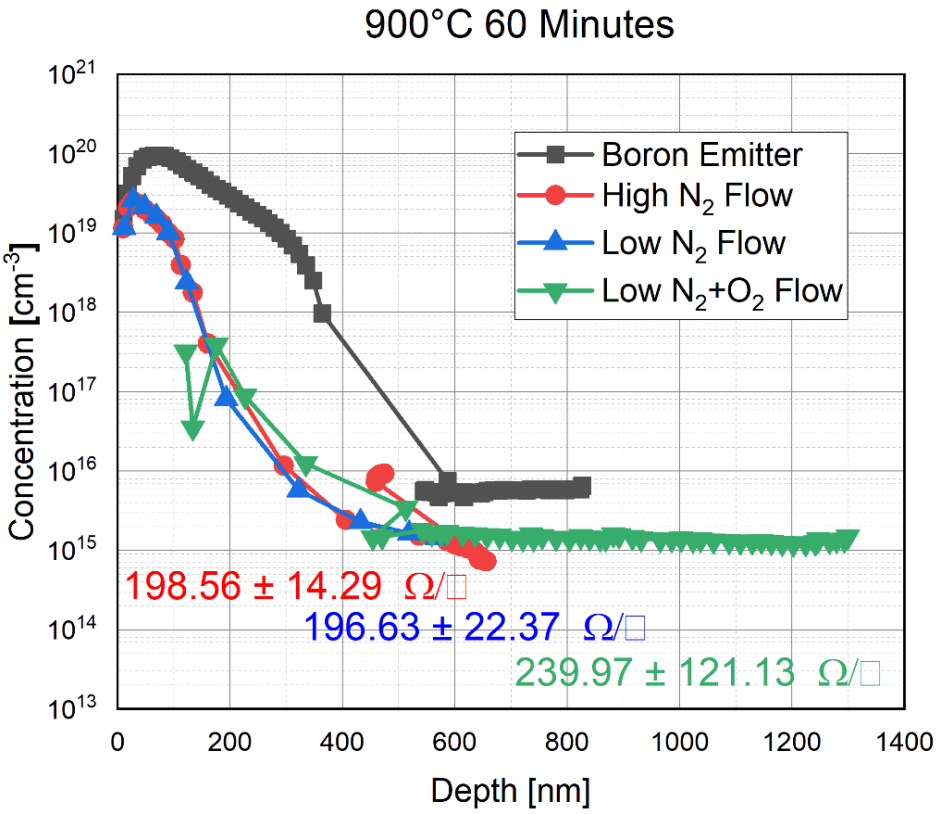

Figure 55 The ECV results of varied environment trials.

Based on ECV profiles, it is clear that the reduction in nitrogen flow alone did not have a significant effect on the sheet resistance values, and a slight reduction in uniformity. It was also worth noting that samples annealed under high (120 sccm) and low (25 sccm) N_2 flow showed the same concentration profile. On the other hand, with the introduction of oxygen to the environment, both the uniformity and sheet resistance were worsened. The surface got highly oxygenated and thus during the HF dip, the oxygen rich BSG was stripped away, realised by the reduction in peak

concentration. However, the rest of the concentration profile changed along with other flow schemes.

Unfortunately, due to the high oxygen consumption, the sets involving 900°C and 950°C for all durations of high oxygen flow set were discontinued, and those samples did not have measurable concentration profiles.

Last doping profiles belong to low O_2 and N_2 flow samples, shown in Figure 56. The best ECV results were obtained at the highest annealing temperature, 950°C with questionable results at 900°C. For almost all the samples the peak concentrations were at least one order of magnitude lower than both the high flow N_2 case and the boron emitter. The increased sheet resistance around 60 minutes could be observed on these samples as well. The 900°C sample profiles did not show the characteristic behaviour of the paste observed on the samples annealed at the high temperatures. The observation was that the duration was not sufficient enough to initiate proper doping and boron tends to diffuse slower.

From the 4PP measurements, the sheet resistances and their nonuniformity were high for all the samples. This highly resistive surface could hinder the ECV measurements as well. Unfortunately, for the annealing temperatures of 800 and 850°C, the boron paste did not diffuse at all and both the ECV results and the 4PP measurements yielded the concentration and the sheet resistances of the substrate, instead of a p^+ layer.

After the annealing and HF dip, the samples were also measured for their iV_{oc} values as shown in Figure 57. Considering all temperature and duration ranges it is clear that the paste yields best iV_{oc} values, a range from 550 to 580 mV when the environment was of pure nitrogen. Aside from some outliers, the general trend was a decrease in iV_{oc} as the annealing duration increased. This could be due to the variation in the concentration of atoms at the surface.

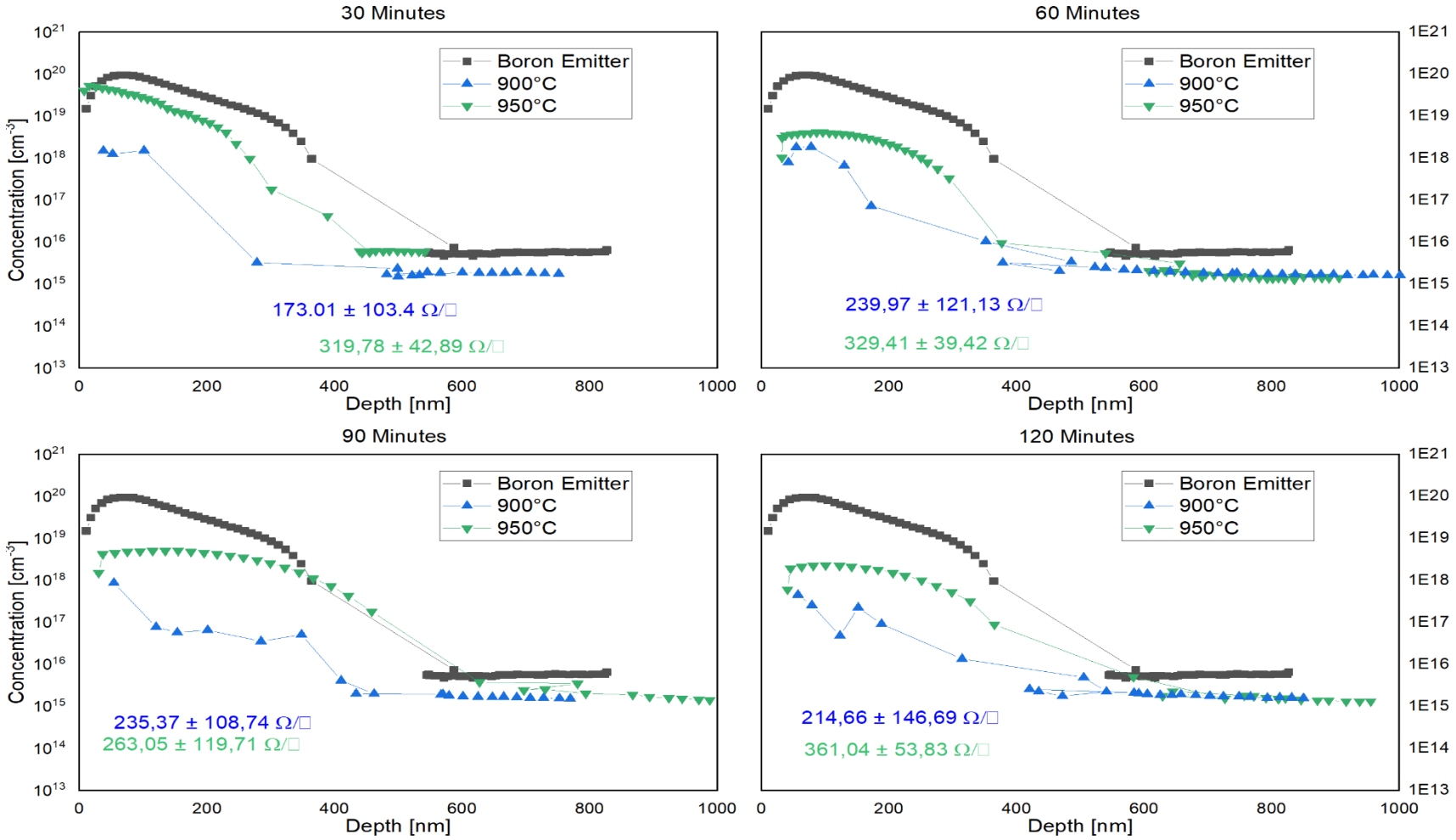

Figure 56 The ECV and 4PP results of annealing trials under low N_2 (5 sccm)+O_2 (20 sccm) flow.

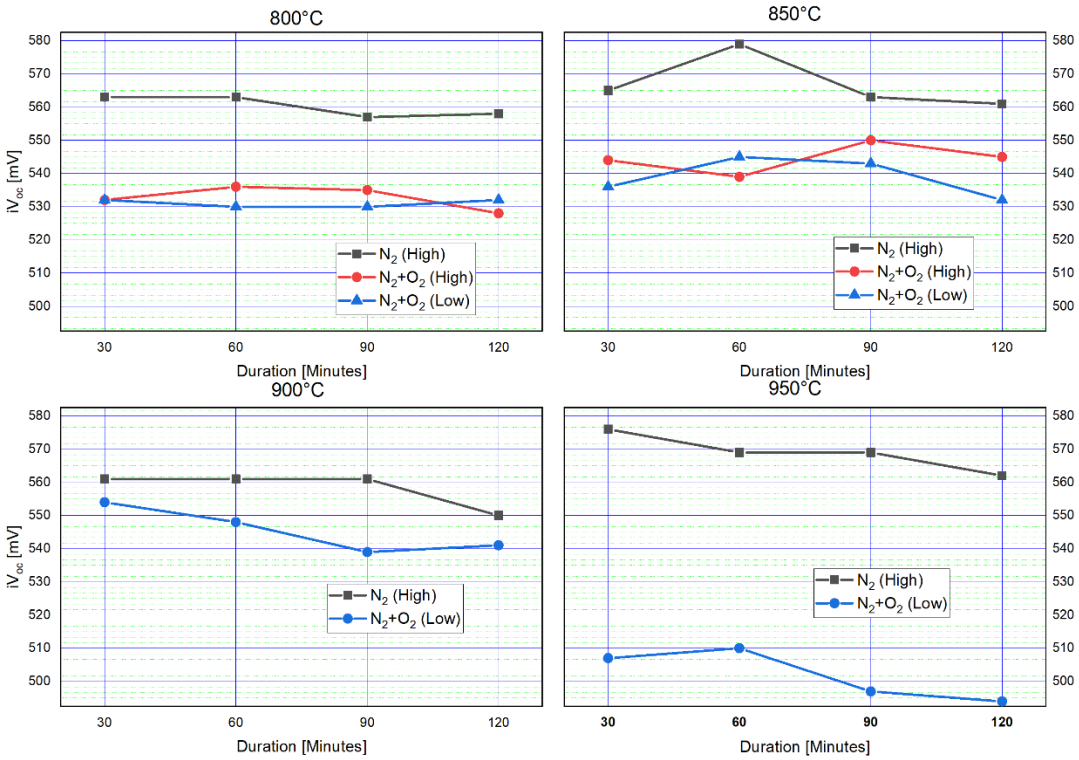

Figure 57 The iV_{oc} results of the experimental set.

After the metallisation of the samples, dark I-V and TLM measurements were carried out. Instead of using a regular front H-grid, a TLM pattern with varying pad separation was evaporated (Figure 44) as the front contacts and was annealed at 400°C. Thus, the same samples could be used both for dark I-V and TLM measurements. The general behaviour of the samples was ohmic, a few showed diode behaviour which could be related to the increasing annealing temperature for both annealing environments. Another hindering reason could be due to the weak contact formation of thermal evaporation compared to FT paste. After the first few test measurements, it was realised that the results were highly inconsistent with one another, both on the same sample among different rows, and from sample to sample. For these reasons, TLM measurements on this set were cancelled and varying TLM pattern was abandoned to equidistant pattern applications like bifacial.

For the case of cell fabrication, B-paste was annealed first at a high temperature, then it was followed by $POCl_3$ diffusion during which B-paste printed regions were protected by a SiN_x layer. In Figure 58 the effect of $POCl_3$ diffusion to B-paste profile is shown. Even though the $POCl_3$ diffusion was done at a lower

temperature than B-paste annealing temperature, it is clearly seen that a slight shift occurs throughout the profile. The enhanced diffusion in the tail region could be related to the additional thermal energy provided by $POCl_3$ diffusion while the increase in the surface concentration could be explained by the activation of inactive boron atoms during $POCl_3$ diffusion. Lastly, double printing of the B-paste was tried to achieve peak concentrations similar to the boron emitter. But as can be seen in Figure 58, the peak concentration only increased slightly without reaching to the boron emitter whereas the doping profile shifted deeper into the substrate similar to the boron emitter. This could be observable as a second layer of B-paste present on the surface satisfying the high to low gradient diffusion. Double printing, however, did not make a lot of sense as IBC processes would have good alignment requirements and that would present a challenge to already existing problems.

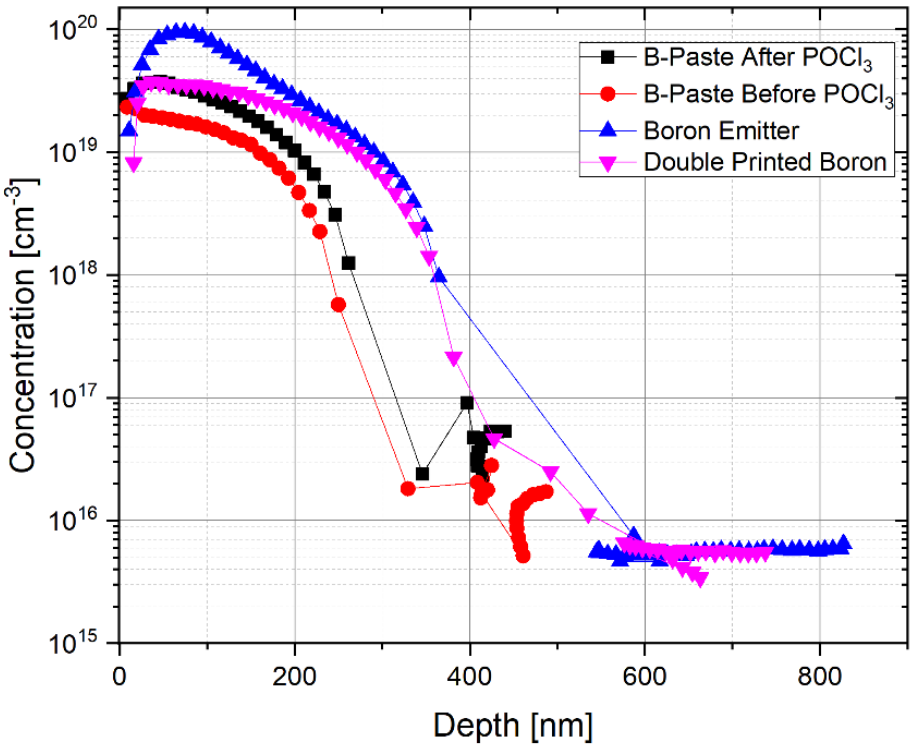

Figure 58 The ECV results of various high temperature processes and double printing.

4.2.2 Second Set of Optimisations for the Printing and Drying Parameters for Polished (SDE) and Textured Wafers

The aforementioned bubbling effect was planned to be optimised with this set of experiments. For the first trials, a set of 135 textured samples were screen-printed by B-paste and dried using belt furnace. While the samples were collected, flakes were realised on the surface, shown in Figure 45 with SEM and in Figure 59 with optical microscope images. In hindsight, the flakes were considered as artefacts of the drying process and they were dismissed, just like in the bubbling case where bubbles were considered as artefacts of the printing process, and the experiment continued as planned. The printed samples were annealed, and HF dipped, then measured with 4PP. The results showed that B-paste did not diffuse into Si at all which was also double-checked by ECV measurements. At that point, it was realised that due to the long shelf waiting time for the printed samples to be dried in the belt furnace, they actually have air-dried instead.

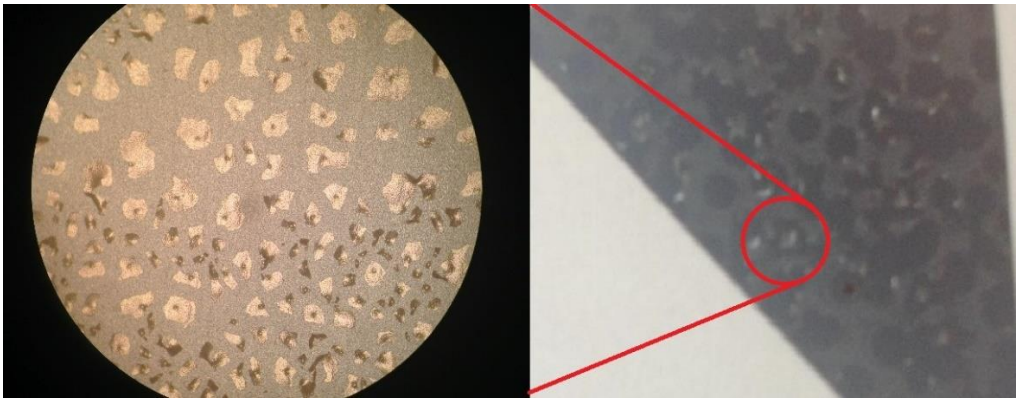

Figure 59 The B-paste flakes on the wafer surface (right) under the optical microscope (left).

To correct this issue, a smaller set of 9 textured and 9 SDE samples were prepared where the previously optimised annealing parameters were used. Although B doping was achieved on all the samples, textured wafers were more uniform with sheet resistance (142 ± 9 Ω/□) in terms of sheet resistance compared to SDE wafers (227 ± 125 Ω/□). For the sheet resistance readings, both types of wafers were equally higher than the samples prepared in annealing studies shown in Figure 54 with the ECV profiles of the second trial given in Figure 60. Comparing both these figures, it is clear that the surface concentration was actually lower than the annealing studies.

In this set, the samples were annealed for 100 minutes which could be the reason why the sheet resistances increased.

Even though the results of this batch yields positive results for the textured wafers, the actual experience with the B-paste required further investigation of increasing the adhesiveness of it to a textured surface. For that reason, the following experiments were done.

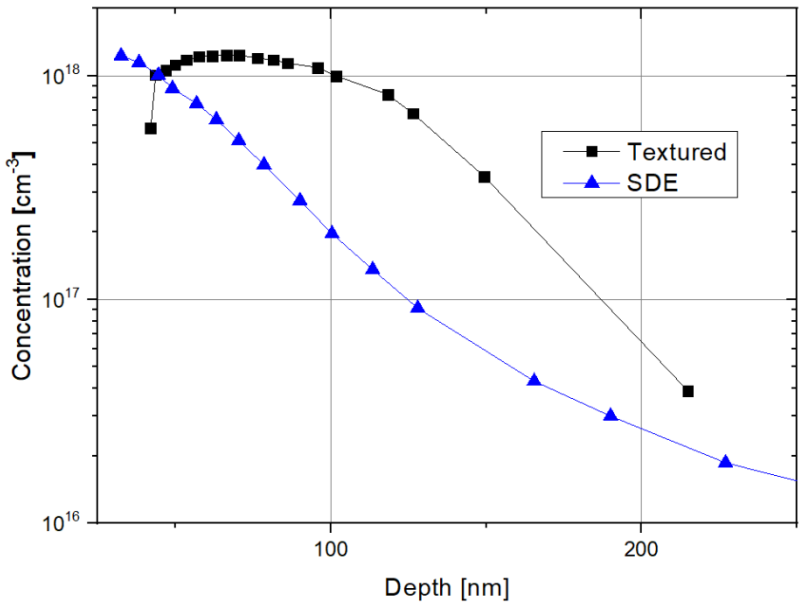

Figure 60 The ECV results of the second trial.

4.3 Pyramid Rounding Studies

The many failed attempts for the optimisation of B-paste on textured surfaces required the investigation of pyramid rounding. For that reason, mixtures of various acids in different concentrations were used. Below the results of these trials are shown sorted by sets of trials.

4.3.1 First Set of Rounding Studies

The samples with high nitric acid concentration (HNAC - right side in Table 5) yielded a gradually varying distribution of the reflectance could indicate the controllability of etching, while the lower reflectance results were obtained in low nitric acid concentrations (LNAC - left side in Table 5); some of them are lower than textured values. These promising results shifted the focus on lower nitric acid concentrations due to not only the low reflectance but also the reduction in acid

consumption. LNAC samples partially and HNAC samples totally showed a reduction in reflectance as the amount of water is increased. This could be due to a decrease in etchant concentration. The mixture becomes less harsh and the etch rate was slowed down. This could also mean that; especially for similar reflection values on HNAC samples with textured samples; the etching was not enough to round the pyramids.

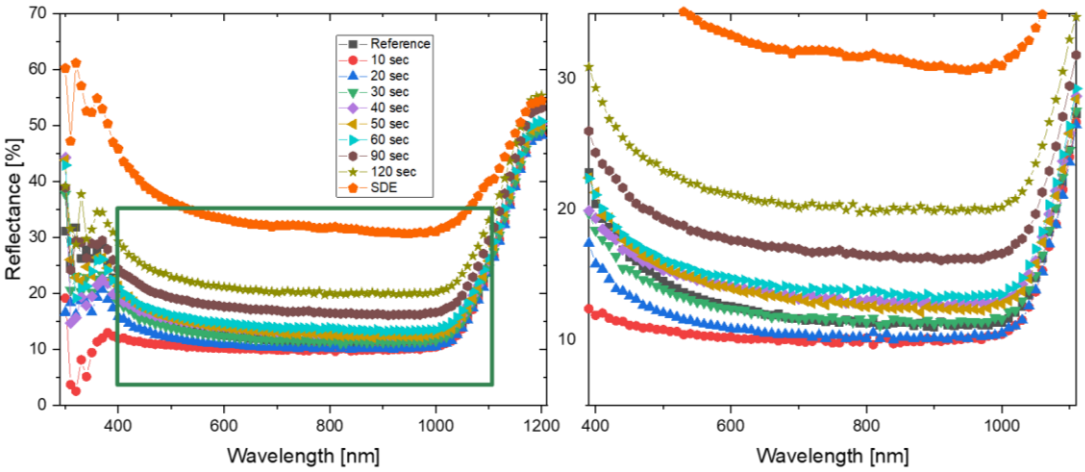

Figure 61 The reflectance results of first pyramid rounding trials with the acid concentrations of (1)HF : (5)HNO_3 : (1)H_2O. The right-hand side graph represents the boxed part on the left-hand side graph.

The results shown in Figure 61 indicated that a short dip, 10, 20 and 30 seconds, in the acid mixture of (1) HF : (5) HNO_3 : (1) H_2O reduced the sample reflection even further than any other durations. It can also be observed that as the duration increased, the reflection also increased. But, none one of the durations yielded a reflection that was in the proximity of SDE type wafers. It is worth mentioning that the KOH textured samples are referred to as the reference. Although considering the reflection for short durations resulted in an overall positive result especially around the UV region, the surface texturing was not adequate enough for paste applications Figure 62.

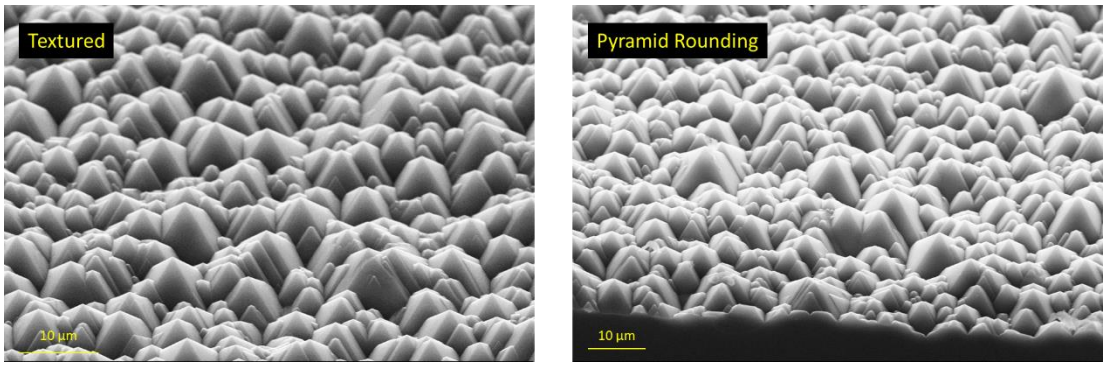

Figure 62 The SEM images of textured (left) and rounding (right) samples in first trials for the acid concentrations of (1)HF : (5)HNO_3 : (1)H_2O in 20 seconds.

The darkened sample shows desired results, however achieving it on a small sample in a uniform manner is difficult, thus larger samples would be even more problematic.

Table 5 The weighted average reflectance results of the first set of rounding studies on n-type wafers. The result shown with the red font is measured from darkened samples. The weighted average is over 400-1100 nm range.

Weighted Average Reflectance [%]	(1) HF (5) HNO_3 (0) H_2O	(1) HF (5) HNO_3 (1) H_2O	(1) HF (5) HNO_3 (5) H_2O	(1) HF (5) HNO_3 (10) H_2O
Textured	13.16	13.15	13.16	13.16
10 sec	17.83	11.31	17.00	18.78
20 sec	20.43	11.79	14.63	20.25
30 sec	24.79	13.15	13.30	24.41
40 sec	25.94	14.60	13.18	27.62
50 sec	31.30	14.38	13.39	28.08
60 sec	31.68	15.26	13.15	32.05
90 sec	33.45	18.21	9.33	36.16
120 sec	39.18	21.83	13.21	37.64
SDE	33.31	33.31	33.31	33.31

Weighted Average Reflectance [%]	(1) HF (10) HNO_3 (0) H_2O	(1) HF (10) HNO_3 (1) H_2O	(1) HF (10) HNO_3 (5) H_2O	(1) HF (10) HNO_3 (10) H_2O
Textured	13.15	13.15	13.15	13.15
10 sec	18.74	16.95	14.26	13.26
20 sec	19.95	18.29	15.51	12.47
30 sec	23.56	18.33	17.81	12.73
40 sec	23.12	24.53	18.88	11.83
50 sec	23.84	22.16	18.98	13.59
60 sec	25.29	26.50	21.08	13.02
90 sec	32.39	28.29	25.85	15.28
120 sec	33.38	36.58	27.34	16.16
SDE	33.31	33.31	33.31	33.31

4.3.2 Second Set of Rounding Studies

The requirement for pyramid rounding for B-paste application while maintaining the lowest possible reflection from the first trials required the selection of the concentrations laid in Table 3 – second set. As shown in Figure 62, the surface needed longer durations for the etching to take effect. Since the results of these samples were to be used for large size solar cell applications, the scale-up requirements were also needed to be considered. For that reason, a recipe with low acid usage that could control the etching rate by varying the water concentration was designed.

Table 6 The weighted average reflectance results of the second set of rounding studies on n-type wafers. The weighted average is over 400-1100 nm range.

Weighted Average Reflectance [%]	(1) HF (5) HNO_3 (1) H_2O	(1) HF (5) HNO_3 (5) H_2O
Textured	12.65	12.65
60 sec	23.31	12.47
70 sec	25.23	12.59
80 sec	26.78	12.61
90 sec	22.4	12.43
100 sec	27.45	12.69
SDE	30.23	30.23

As shown in Table 6, extending the rounding duration had very different results for the samples. For the same recipe used in the first trials for the same duration, lower water concentration - 60 seconds, the reflection jumped from 15.26% to 23.31%. On the other hand, for high water concentration samples, the reflection results remained the same compared to the previous set. The results indeed showed that the variation of water concentration could be used to control the etching rate.

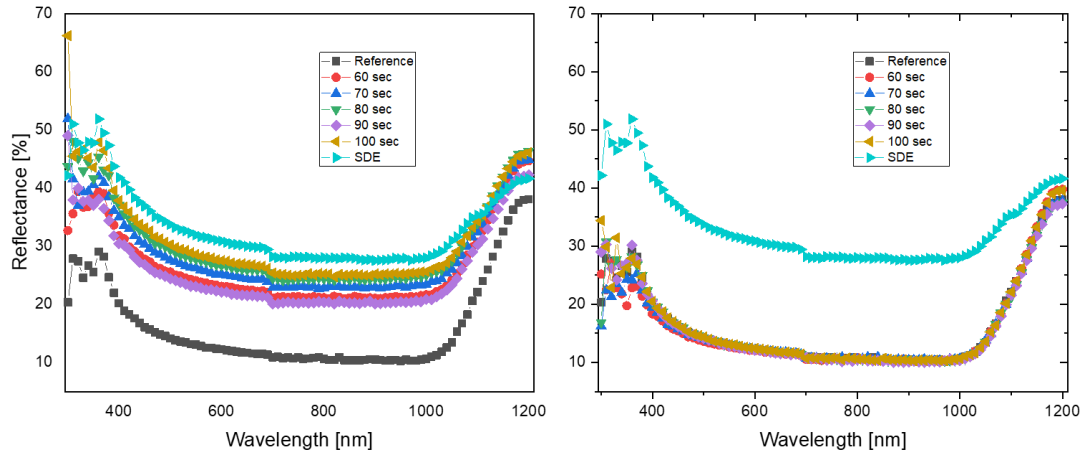

Figure 63 The reflectance results of second pyramid rounding trials with the acid concentrations of (1) HF : (5) HNO_3 : (1 - left and 5 - right) H_2O.

From Figure 63 it is observed that lesser water amount caused the acid mixture to react with the surface more therefore, etching it very close to the proximity of SDE. On the other hand, for greater water concentration mixture the etching had slowed down or maybe did not happen at all due to the exact reflection results obtained in

comparison to the textured surface. The SEM images, Figure 64, show that the surface was indeed etched very harshly, and the surface looked closer to of SDE with lesser water concentration. On the other hand, for the greater water concentration, the surface was similar to a textured surface with tips of the pyramids slightly more slanted than usual.

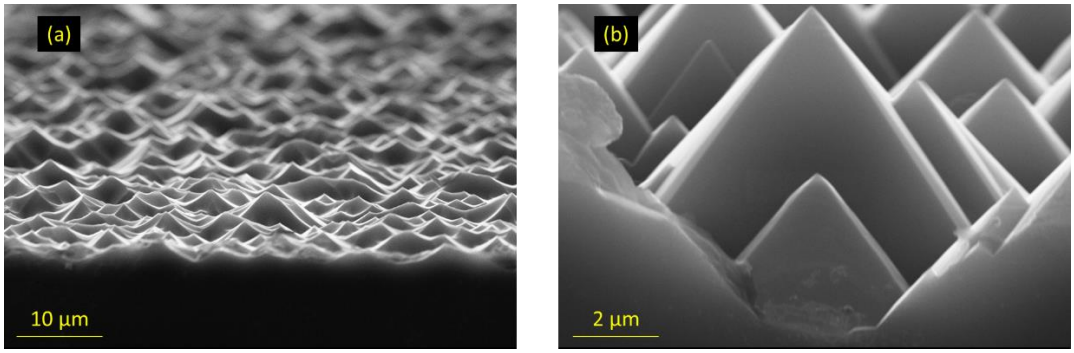

Figure 64 The SEM images of (a) low water concentration and (b) high water concentration samples for the second pyramid rounding trials.

4.3.3 Final Set of Rounding Studies

As none of the rounding trials yielded satisfactory results a third set was designed, details are shown in Table 3 – final set. In this set the etching durations were varied and p-type wafers were also introduced as the following solar cell trials were planned to include them as well. As a secondary test, to see whether as-cut n- and p-type wafers could possibly be used for paste applications were also included. These as-cut wafers were planned to undergo the rounding recipe of this section and to see if the saw damage can be removed while rounding. The recipes used in the previous sets were useful if the only desired outcome were an improvement in reflection. However, the actual rounding effect occurred either extremely rapid or extremely minuscule and adhesiveness of the paste to the surface is the main concern as long as reflections lower than SDE could have achieved.

Table 7 The weighted average reflectance results of the final set of rounding studies on n-type and p-type wafers. The weighted average is over 400-1100 nm range.

Weighted Average Reflectance [%]	Textured	25 sec	35 sec	45 sec	75 sec	90 sec	150 sec	165 sec	As-Cut	90 sec (As-Cut)
n-Type	13.04	13.16	13.05	12.93	14.88	13.25	x	13.27	41.69	17.53
p-Type	12.91	13.42	12.98	12.75	12.21	13.64	14.65	13.07	40.75	19.87

The reflectance results of the final set are given in Figure 65. For the as-cut wafers of both types, it was observed that the reflectance at the UV region reduced significantly after etching. They are also similar to textured and rounded samples in the UV range. The reduction on the reflectance in the infrared region is, however, low in both cases, and about 10-15% higher than other samples.

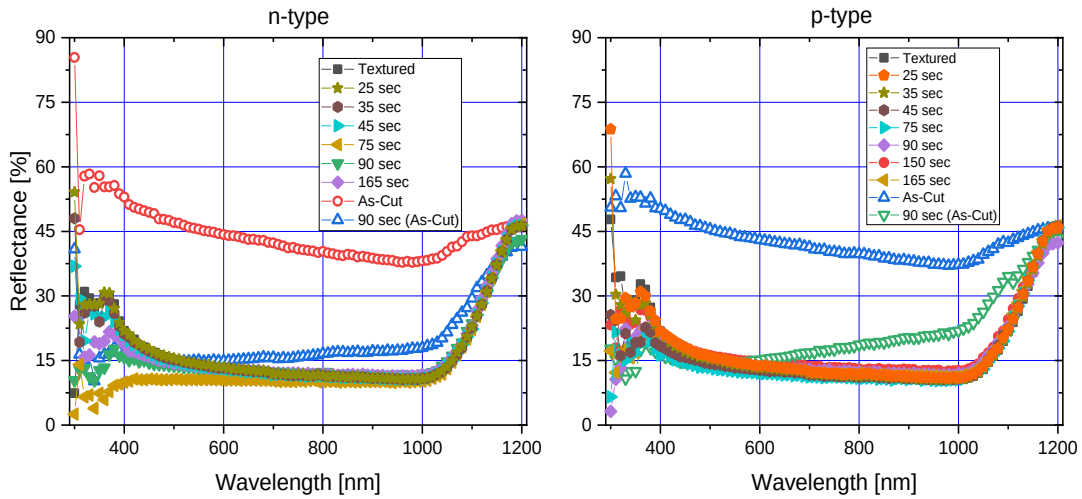

Figure 65 The reflectance results of the final rounding trials on n- and p-type wafers.

Comparing textured and rounded samples of this set, it was observed that all trends in the visible and infrared region are similar to one another. However, in the UV region, there is a spreading. For n-type wafers 75 seconds of etching yields the lowest reflection values which were the preferred etching duration for the following sets of cell sets. On the other hand, for p-type no singular lowest reflectance value corresponds to a duration. For that reason, the weighted average reflectance values, shown in Table 7, as well as SEM images, shown in Figure 67, were also considered for the choice regarding p-type etching recipe. In both images, it is shown that the tips of the pyramids are slightly rounded.

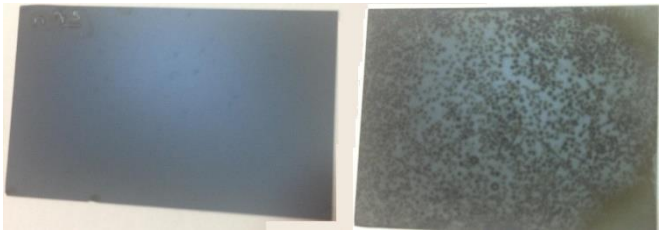

Figure 66 The surface of n-type (left) and p-type (right) wafers after rounding.

Another important observation of this set was that p-type wafers would react with acids much more than n-type wafers. The aforementioned bubbling effect on the surface had a visible effect on the sample surface especially on p-type wafers if left alone, as shown in Figure 66.

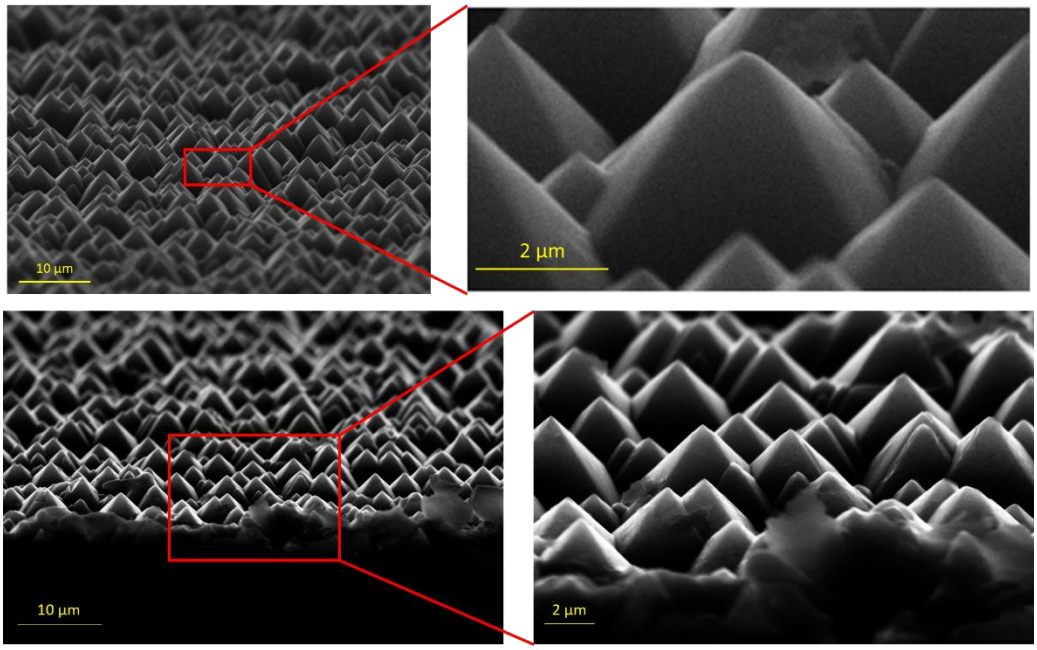

Figure 67 The SEM images of n-type (top) and p-type (bottom) of rounding samples at 75 seconds.

Introduction of Acetic Acid

To control the etching better a subset was designed where acetic acid was introduced to already existing mixture.

Table 8 The weighted average reflectance results of the final set of rounding studies on n-type and p-type wafers with acetic acid. The weighted average is over 400-1100 nm range.

Weighted Average Reflectance [%]	Textured	15 sec	30 sec	45 sec	60 sec	75 sec	90 sec	105 sec	120 sec	600 sec
n-Type	12.68	12.60	12.59	12.89	12.63	12.58	12.38	12.78	12.36	17.86
p-Type	14.49	14.74	14.51	14.27	13.58	12.79	13.61	13.64	13.46	25.47

The results, shown in Figure 68, indicated that the reflection of the rounded samples with the introduction of acetic acid showed improvement in the UV region for p-type wafers whereas, no changes occurred for n-type wafers.

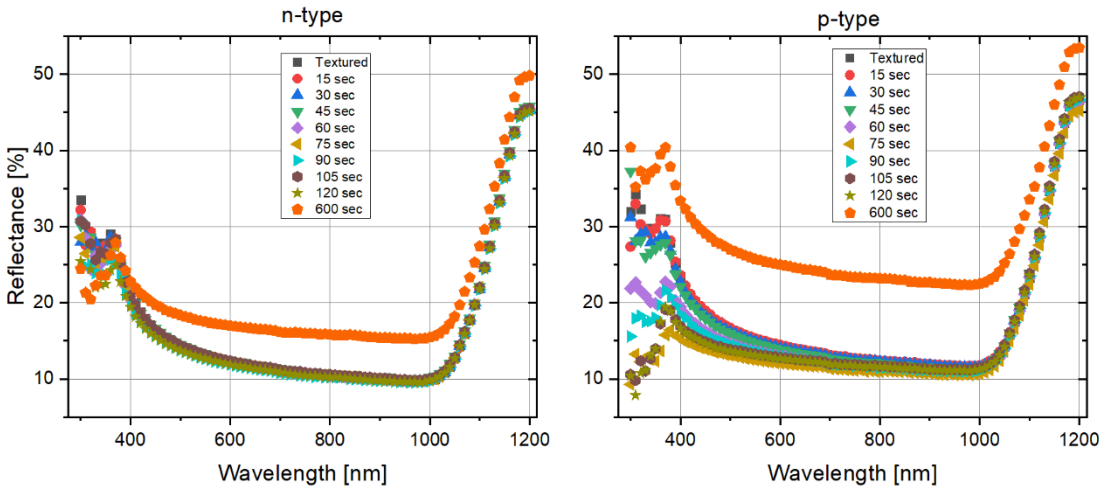

Figure 68 The reflectance results of pyramid rounding samples on n-type (left) and p-type (right) wafers with added acetic acid to the mixture.

The introduction of acetic acid to the mixture was tested at an extreme etching scheme of 10 minutes. It is shown in Figure 69 – (b) that the pyramids were still visible at the end of the etching unlike seen in Figure 69 – (b). The reduction in etch rate was probably not only due to the acetic acid introduction but also related to the increase in water concentration.

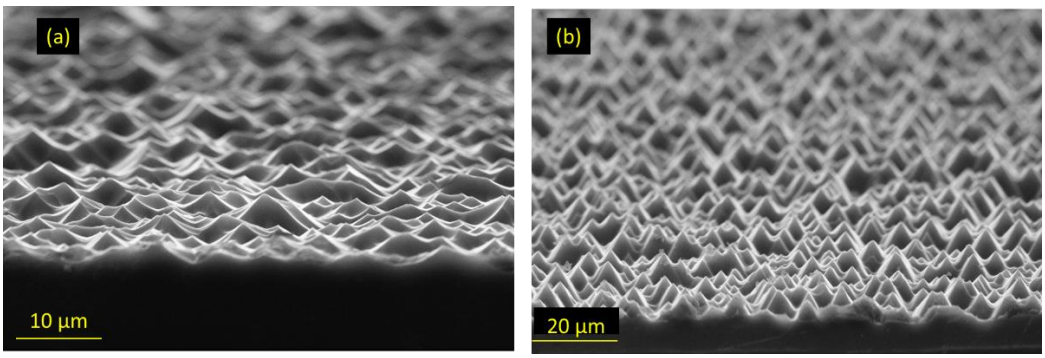

Figure 69 The SEM image of the final set of pyramid rounding samples (a) without and (b) with acetic acid. The sample with acetic acid was etched for 10 minutes.

4.4 Final Set of Optimisations

Before producing the following solar cell sets, a small test had been done on SDE, textured and rounded pyramid cells with the B-paste. The test aimed to check

the adhesiveness of the paste to various surfaces. In Figure 70, it is shown that the B-paste adheres to SDE wafers decently with a coverage of 90%.

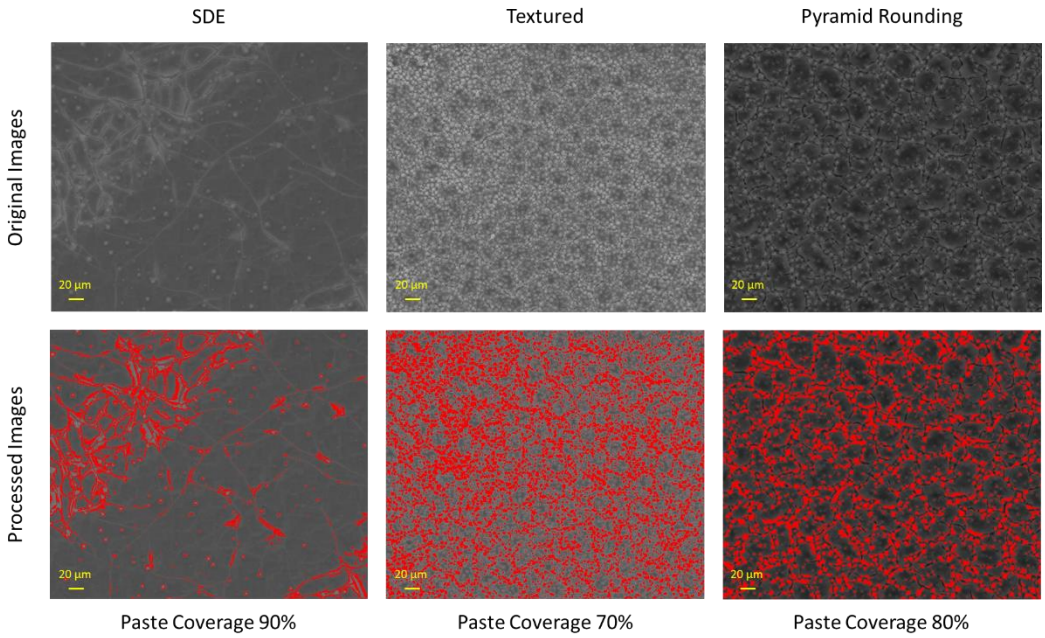

Figure 70 The SEM images of the B-paste (gray) coverage on various surfaces after printing and curing. The images were processed by using the software "ImageJ".

The flake sizes were usually small in comparison to the other two texturing types. Comparing the textured and rounded surfaces, it is clear that about 10% more paste coverage was achieved on rounded samples. The larger parts of these samples were annealed to check their doping profiles. Unfortunately, only the SDE wafer yielded results whereas, the other two failed and only the substrate concentration was measured. Although the surface coverage increased about 10%, the diffusion was not achieved due to the flakiness of the B-paste so further investigation is required.

At this point, it is worth mentioning that a set of IBC cells were produced using textured wafers. But those textured wafers were printed at the early stages of the experimental process. But as time passes the paste quality may have degraded due to various conditions.

4.4.1 Small-Size Bifacial Cells

Using all of the optimised parameters from the annealing, printing and drying studies, as well as the pyramid rounding studies; 5 cm x 5 cm pseudo square bifacial

cells were produced on n-type and p-type wafers. Corresponding reflection spectra are shown in Figure 71 top two graphs.

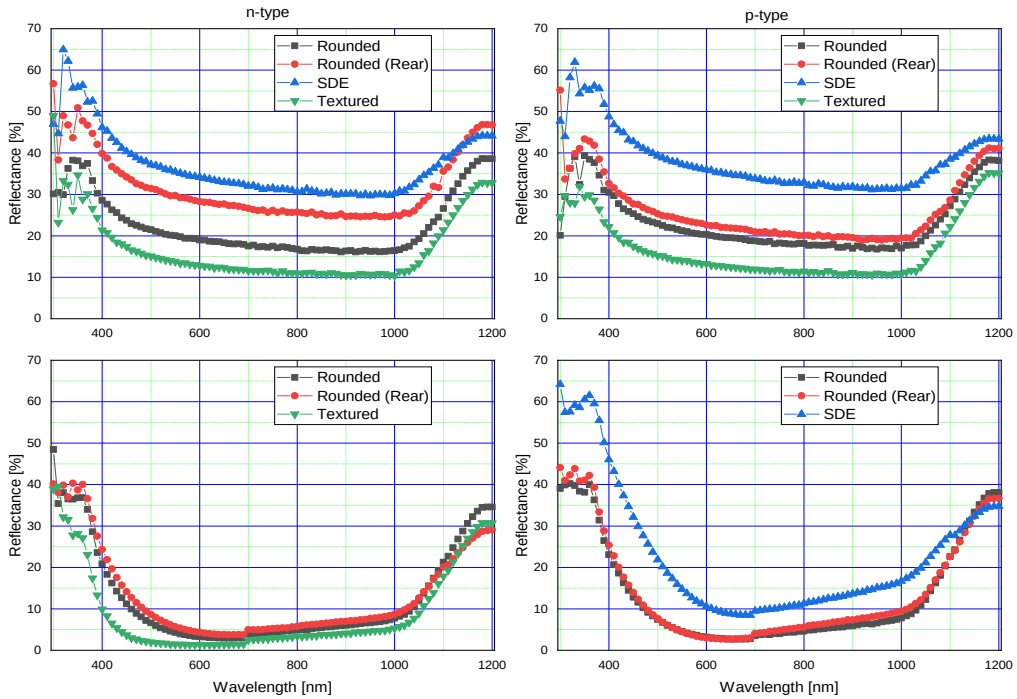

Figure 71 The reflectance of bifacial cells after rounding (top) and after ARC (bottom). The left-hand side shows n-type wafer results and p-type results are given on the right-hand side.

The reflection measurements have shown that rounded samples are indeed in between textured and SDE surfaces. Initially, the rear side ($POCl_3$ diffused side) was expected to be safe from the effects of rounding as samples were immersed in the acidic mixture single side up position (B-Paste to be printed). But reflection results indicate that the rear side was also etched, and the weighted average reflectance of these surfaces are given in Table 9.

Table 9 The weighted average reflectance results of the produced bifacial cells after rounding and after the ARC layer.

	Wafer	Process	Rounded	Rounded (Rear)	SDE	Textured
Weighted Average Reflectance [%]	n-type	After Rouding	18.29	26.92	32.34	12.56
		After Nitride	7.37	8.40	x	4.73
	p-type	After Rouding	19.27	21.50	33.80	12.80
		After Nitride	7.59	8.48	16.27	x

The sheet resistance values of the annealed and HF dipped cells were measured using the 4PP, shown in Table 10. For n-type textured and SDE wafers, it was

observed that after annealing the B-paste was not sufficient enough to turn the polarity from p to n-type, as both sides yielded the same sheet resistance values. On the other hand, for p-type textured and SDE wafers, B-paste was capable of doping the substrate uniformly.

Table 10 The sheet resistance values of annealed samples for bifacial solar cells.

Sheet Resistance [Ω/sq]						
Wafer Type	Textured		SDE		Pyramid Rounding	
	$POCl_3$	B-Paste	$POCl_3$	B-Paste	$POCl_3$	B-Paste
n-Type	30±2	31±2	20±10	18±1	31±1	52±29
p-Type	38±3	76±1	31±2	110±2	36±3	266±34

For pyramid rounding case, both n-type and p-type wafers yielded nonuniform doping profiles and for n-type substrate, although nonuniform, a variation in the sheet resistances exist. The doping profiles of p-type SDE wafers, Figure 72, were measured on both sides as those set of samples were expected to work if none of the others did. The doping profile of pyramid rounded (PR) samples were not measured by ECV as the surface structure would be something in between textured and SDE, and that would require correction factor calculations.

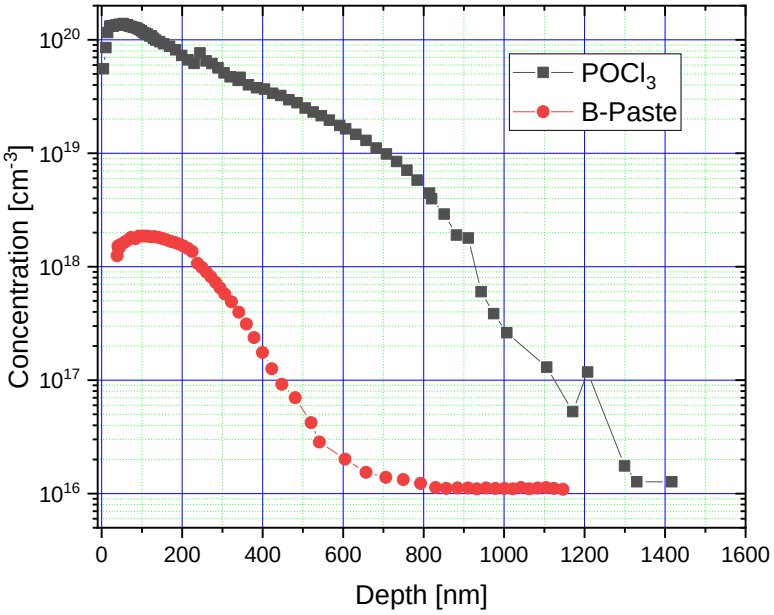

Figure 72 The ECV results of p-type SDE wafers used in bifacial solar cells.

Initially, the solar cell fabrication steps up to SiN_x deposition step were applied on 126 small-size wafers. At this step, however, due to the sample size, some samples had to be eliminated. For that reason, iV_{oc} measurements were carried out after annealing and after oxidation. Among those samples, the best four sets were chosen (n-type; textured and PR– p-type; SDE and PR), and those samples continued to ARC deposition.

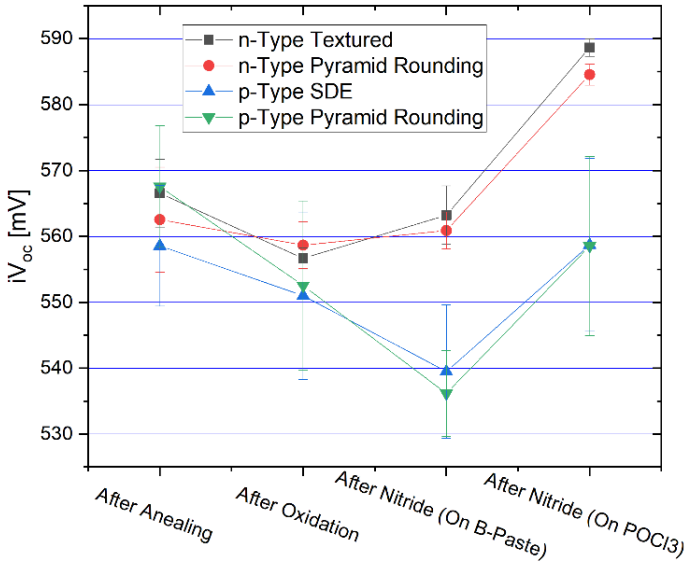

Figure 73 The implied open-circuit voltage results of bifacial cells after various process steps.

In Figure 73; for after annealing and oxidation cases; the iV_{oc} measurements were applied in an emitter-up manner, whereas for after nitride deposition, both sides were measured. After annealing, the iV_{oc} values were close to one another and peaking at 567 mV for p-type PR samples. After oxidation, there was a slight decrease and samples were in the range of 550-560 mV. For p^+/n and n^+/p junctions, the iV_{oc} improved slightly, whereas for n^+/n junction showed around 30 mV of increase. On the other hand, p^+/p junction suffered after ARC layer deposition. One of the main reasons for such variations is due to the nonuniformity of the ARC layer on B-paste side. The HF dip was kept short to ensure not to etch away the doping, thus some of the PSG must have been left on the surface. The PSG caused a rougher surface that ARC could not be coated the entirety of the surface. The $POCl_3$ side was however uniformly coated. The other reason is that doping concentration was lower than what has been expected. This was assumed to be related to the age of the paste.

As the last step, the ARC deposited samples were double-side screen-printed with FT-Ag and FT-AgAl paste with H-grid pattern for metallisation. The samples were then fired with peak temperature range of 880-940°C with 20°C of increments. J-V characteristic of the best performing cell is shown in Figure 74.

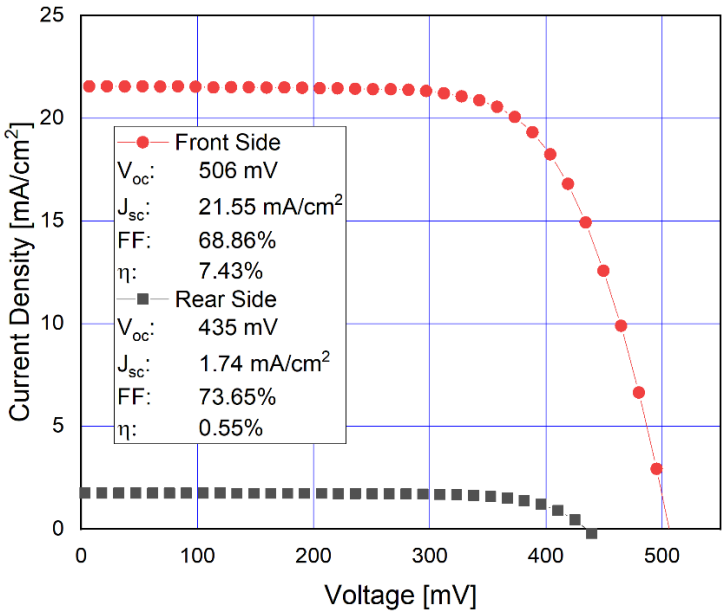

Figure 74 The J-V curves of the best cell produced using B-paste. The cell is p-type PR and fired at 920°C.

The best bifacial cell fabricated with these parameters yielded 7.43% efficiency on the front side and 0.55% efficiency on the rear side. The bifaciality factor of the cell is 7.40%. The difference between FF of the front and rear sides may be caused by the peak firing temperature where different pastes e.g. FT-Ag and FT-AgAl would require different peak temperatures. The basis of the best cell is on a p-type wafer with pyramid rounding. This indicated that rounding, although poorly, did work with bifacial cells and can be used for IBC solar cells. The EQE measurements, shown in Figure 75, of the bifacial cell from the front side, yielded J_{sc} values of 23.66 mA/cm^2 which when corrected, could improve the cell efficiency to 8.16%.

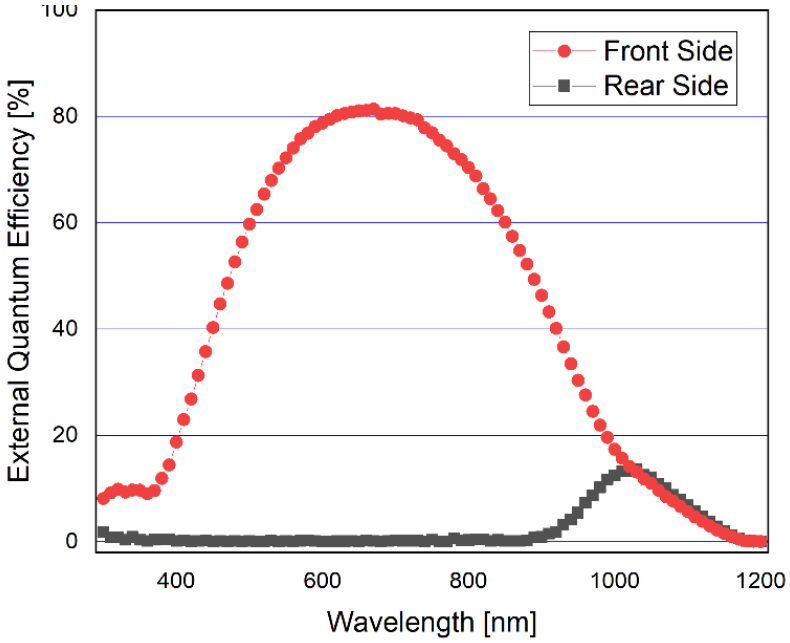

Figure 75 The EQE of the best bifacial cell.

The EQE results show that the rear side is slightly responsive to the infrared region and shows no response in neither UV nor visible range. On the other hand, the front surface shows a similar response to the rear side after 1000 nm.

4.4.2 IBC Cells

Following the described cell process flow a set of IBC cells were fabricated using textured p-type Cz-Si wafers with 1-3 Ω.cm resistivity. After $POCl_3$ (on both front and rear) and B-paste diffusion, the dopant concentrations of all dopants on either side (Figure 76) were measured using ECV. The curve shown as blue triangles indicates the controlled etch-back of the FFE. The diffusion barrier blocking the BSF regions was sufficient enough that after B-paste diffusion, high B concentration was achieved. This also indicates that the etch resist patterning was decent.

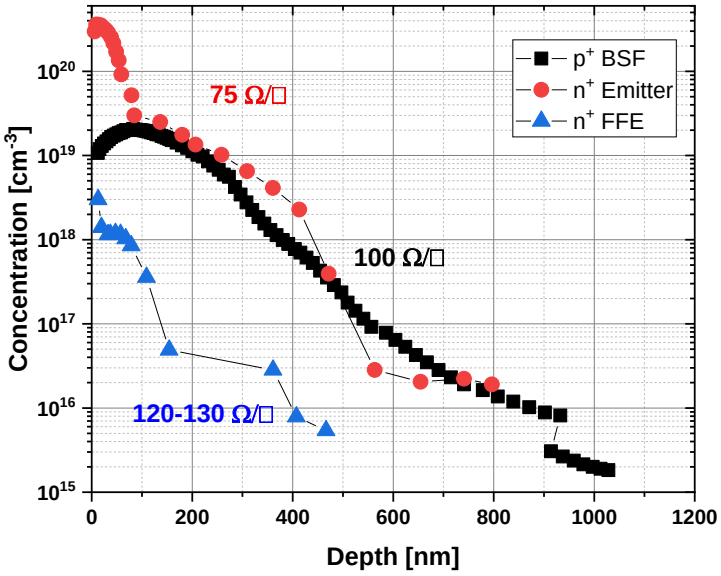

Figure 76 The concentration of dopants on IBC solar cells.

The first working IBC cells, using the parameters listed in Table 4 for boron paste, produced at GÜNAM labs yielded an efficiency of 8.70% with an FF of 76.32%, shown in Figure 77.

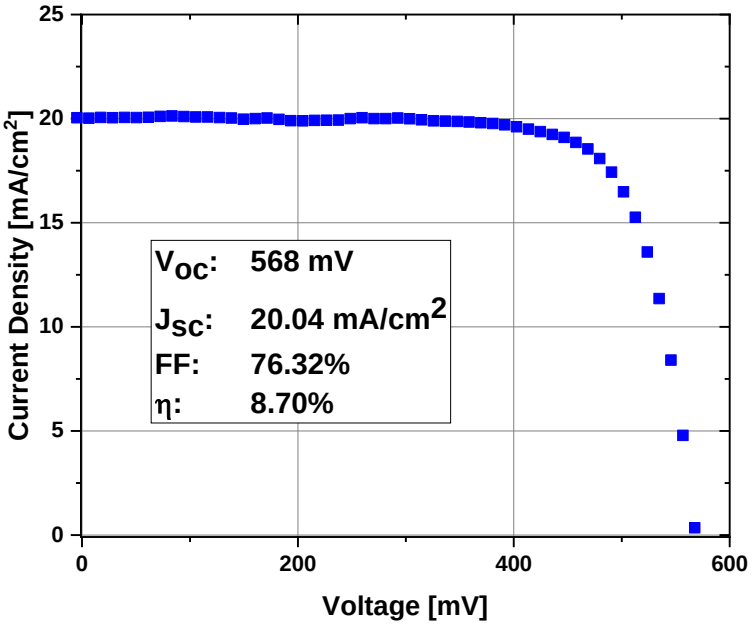

Figure 77 The J-V curve of the best cell produced using B-Paste.

It is observed that the V_{oc} dropped tremendously after the metallisation step as shown in Figure 78. The high metal coverage of the doped surfaces could be the reason why the V_{oc} decreased. Comparing the after oxidation and after silicon nitride

deposition measurements, it was observed that the variations in the pitch size did not have a significant effect on cell efficiency for this size of solar cells.

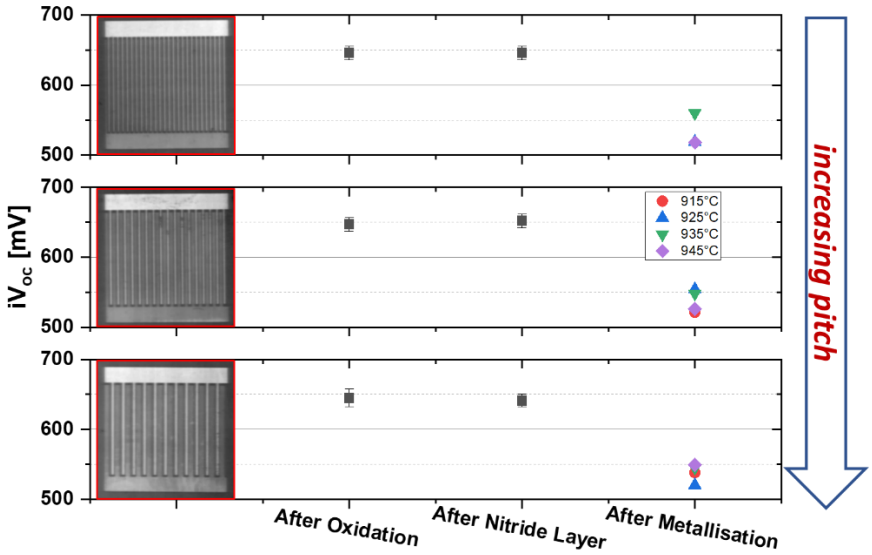

Figure 78 The implied-V_{oc} values of the IBC cells The V_{oc} values after the metallisation step are given as a comparison.

The EQE measurements, Figure 79, show that the cell responsivity in the UV region is almost non-existent due to high recombination values. The response of the emitter region is higher compared to the BSF.

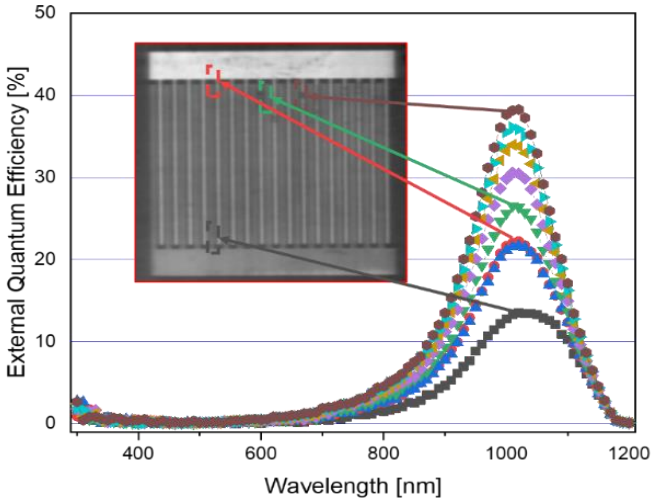

Figure 79 The EQE of the best IBC cell.

CHAPTER 5

CONCLUSIONS

"Scientists will eventually stop flailing around with solar power and focus their efforts on harnessing the only truly unlimited source of energy on the planet: stupidity. I predict that in the future, scientists will learn how to convert stupidity into clean fuel"

- **Scott Adams (1957-)**

In this work, a screen printable boron doping paste has been optimised in the processes of printing, drying and curing for possible device applications. Application of the boron paste has shown to facilitate the process sequence of IBC and bifacial solar cells. Although the efficiency values were low compared to other groups working on similar ideas, the proof-of-concept has been demonstrated. The paste can be applied to bifacial and IBC cells with the most confidence and as shown, decent results have been achieved.

The use of screen-printer for metallisation is a widely accepted method in the solar cell industry. Since such application already has alignment support B-paste is a viable option to have at hand that can be used along with already existing systems. Complex process schemes like IBC could benefit from this approach and become industrially applicable.

In the first part of this thesis work, the B-paste was optimised so that a controlled set of sheet resistance and doping profile could be achieved on textured and SDE wafers. The undesirable bubbling effect which was observed during the printing studies necessitates an optimisation study on this process. Also, the drying studies made it apparent that dried paste could have a flaky form, especially when printed on textured wafers. A further investigation had shown that the surface structure was preventing the paste to adhere to the surface properly and thus under stress caused by the drying step, the flakes would form. To solve this problem rounding recipes were

investigated. After several sets, a suitable etching recipe was achieved. The aim of the recipe was to decrease the surface reflection while increasing the adhesiveness of the paste to the surface. As a secondary benefit, the rounding recipe can be used for various other applications where necessary. The best sheet resistance value of 52.17 Ω/sq was achieved at the annealing temperature of 950°C for 120 minutes. The peak concentration of this profile is 4.51×10^{19} cm^{-3} with the junction depth of 600 nm.

Lastly, using all of the optimisations, two types of solar cells, i.e. bifacial and IBC, were produced. The best bifacial cell has an efficiency of 7.43% with V_{oc} 506 mV, J_{sc} 21.55 mA/cm^2 and FF 68.86% on the front side. On the other hand, the best IBC cell yielded an efficiency of 8.70% with V_{oc} 568 mV, J_{sc} 20.04 mA/cm^2 and FF 76.32%.

As a future work, the paste can be applied to full-size IBC solar cells which were the initial point. Full-size applications may yield better results; as in small-size, alignment issues are usually cumbersome. The reduction in process steps and complications by B-paste integration could allow IBC solar cells to become industrially more feasible. The viscosity of the B-paste could be improved so that screen-printing applications can be easily applied. The boron concentration of the paste could also be altered so that limitations for the peak impurity concentration can match other doping methods

BIBLIOGRAPHY

[1] "Becquerel Prize for Outstanding Merits in Photovoltaics," [Online]. Available: https://www.becquerel-prize.org/about-the-becquerel-prize/alexandre-edmond-becquerel/. [Accessed 30 11 2019].

[2] Y. N. Sudhakar, M. Selvakumar and D. K. Bhat, Biopolymer Electrolytes: Fundamentals and Applications in Energy Storage, Amsterdam: Elsevier, 2018.

[3] D. Lenardic, "Photovoltaics - Historical Development," 23 12 2015. [Online]. Available: http://www.pvresources.com/en/introduction/history.php. [Accessed 30 11 2019].

[4] D. M. Chapin, C. S. Fuller and G. L. Pearson, "A New Silicon p-n Junction Photocell for Converting Solar Radiation into Electrical Power," *Journal of Applied Physics,* vol. 25, no. 5, pp. 676-677, 1954.

[5] K. Jäger, O. Isabella, A. H. M. Smets, R. A. C. M. M. Swaaij van and M. Zeman, Solar Energy: Fundamentals, Technology, and Systems, The Netherlands: Delft University of Technology, 2014.

[6] K. Tate, "Space," 04 October 2012. [Online]. Available: https://www.space.com/17888-first-satellite-sputnik-1-explained-infographic.html. [Accessed 23 May 2019].

[7] C. Frewin, "Renewable Energy," Student Energy, [Online]. Available: https://www.studentenergy.org/topics/renewable-energy#reference-1. [Accessed 11 12 2019].

[8] "Global Atlas," IRENA - International Renewable Energy Agency, [Online]. Available: https://irena.masdar.ac.ae/gallery/#tool/9. [Accessed 11 12 2019].

[9] C. Kittel, Introduction to Solid State Physics, 8 ed., New York: John Wiley & Sons, Inc., 2005, p. 211.

[10] S. Bensalem, M. Chegaar and A. Herguth, "Band gap dependence with temperature of semiconductors from solar cells electrical parameters," *Current Applied Physics,* vol. 17, pp. 57-58, 2017.

[11] A. Goetzberger, J. Knobloch, B. Voß and R. Waddington, Crystalline Silicon Solar Cells, West Sussex: John Wiley & Sons Ltd., 1998.

[12] S. M. Sze and K. K. Ng, Physics of Semiconductor Devices, Hoboken: John Wiley & Sons, Inc., 2007.

[13] Editors of Encyclopædia Brittanica, "Encyclopædia Brittanica," 15 August 2018. [Online]. Available: https://www.britannica.com/science/astronomical-unit. [Accessed 31 May 2019].

[14] "PVLighthouse," 2014 January 2014. [Online]. Available: https://www2.pvlighthouse.com.au/resources/optics/spectrum%20library/spectrum%20library.aspx. [Accessed 5 June 2010].

[15] K. Yoshikawa, H. Kawasaki, W. Yoshida, T. Irie, K. Konishi, K. Nakano, T. Uto, D. Adachi, M. Kanematsu, H. Uzu and K. Yamamoto, "Silicon Heterojunction Solar Cell with Interdigitated Back Contacts for a Photoconversion Efficiency over 26%," *Nature Energy,* vol. 2, 2017.

[16] M. Dayah, "Ptable," 2017. [Online]. Available: https://www.ptable.com/. [Accessed 28 May 2019].

[17] C. Honsberg and S. Bowden, "PVEducation," 2019. [Online]. Available: https://www.pveducation.org/pvcdrom/design-of-silicon-cells/anti-reflection-coatings. [Accessed 05 12 2019].

[18] W. Shockley and H. J. Queisser, "Detailed Balance Limit of Efficiency of p-n Junction Solar Cells," *Journal of Applied Physics,* vol. 32, no. 3, pp. 510-519, 1961.

[19] K. H. Kim, C. S. Park, J. D. Lee, J. Y. Lim, J. M. Yeon, I. H. Kim, E. J. Lee and Y. H. Cho, "Record high efficiency of screen-printed silicon aluminum back surface field solar cell: 20.29%," *Japanese Journal of Applied Physics,* vol. 56, pp. 1-4, 2017.

[20] T. Niewelt, J. Schön, W. Warta, S. W. Glunz and M. C. Schubert, "Degradation of Crystalline Silicon Due to Boron–Oxygen Defects," *IEEE Journal of Photovoltaics,* vol. 7, no. 1, pp. 383-398, 2017.

[21] C. Sun, D. Chen, F. Rougieux, R. Basnet, B. Hallam and D. Macdonald, "Kinetics and dynamics of the regeneration of boron-oxygen defects in compensated n-type silicon," *Solar Energy Materials and Solar Cells,* vol. 195, pp. 174-181, 2019.

[22] C. Walsh, "Solar Cell Efficiency: N-type v. P-type," CED Greentech, 2016. [Online]. Available: https://www.civicsolar.com/article/solar-cell-efficiency-n-type-v-p-type. [Accessed 2019 December 17].

[23] A. Blakers, "Development of the PERC Solar Cell," *IEEE Journal of Photovoltaics,* vol. 9, no. 3, pp. 629-635, 2019.

[24] M. A. Green, A. W. Blakers, J. Zhao, A. M. Milne, A. Wang and X. Dai, "Characterization of 23-Percent Efficient Silicon Solar Cells," *IEEE Transactions on Electron Devices,* vol. 37, no. 2, pp. 331-336, 1990.

[25] G. J. M. Janssen, K. C. J. Tool, E. J. Kossen, B. B. Van Aken, A. J. Carr and I. G. Romijn, "Aspects of bifacial cell effciency," *Energy Procedia,* vol. 124, pp. 76-83, 2017.

[26] Y. Schiele, N. Brinkmann, G. Hahn and B. Terheiden, "Comparison of Bifacial and Monofacial Large-Area n-Type Si Solar Cells from 100 µm Thin Wire-Sawn Wafers," in *31st European Photovoltaic Solar Energy Conference and Exhibition*, Hamburg, 2015.

[27] K. Pickerel, "Solar Power World," 28 May 2019. [Online]. Available: https://www.solarpowerworldonline.com/2019/05/trina-solar-bifacial-topcon-solar-cell-hits-24-58-efficiency/. [Accessed 2019 December 17].

[28] P. J. Verlinden, "High-Efficiency Back-Contact Silicon Solar Cells for One-Sun and Concentrator Applications," in *McEvoy's Handbook of Photovoltaics Fundamentals and Application*, London, Elsevier, 2018, pp. 473-499.

[29] E. Lohmüller, S. Werner, S. Maus, A. Brand, U. Jäger and F. Clement, "20% efficient n-type Cz-Si MWT solar cells with adjustable reverse behavior," *Physica Status Solidi A,* vol. 213, no. 6, pp. 1598-1601, 2016.

[30] N. Guillevin, B. J. B. Heurtault, L. J. Geerligs and A. W. Weeber, "Development towards 20% efficient si MWT solar cells for low-cost industrial production," *Energy Procedia,* vol. 8, pp. 9-16, 2011.

[31] F. Kiefer, C. Ulzhöfer, T. Brendemühl, N.-P. Harder, R. Brendel, V. Mertens, S. Bordihn, C. Peters and J. W. Müller, "High Efficiency n-Type Emitter-Wrap-Through Silicon Solar Cells," *IEEE Journal of Photovoltaics,* vol. 1, no. 1, pp. 49-53, 2011.

[32] G. Paternoster, M. Nicolai, G. de Ceglia, M. Zanuccoli, P. Bellutti, L. Ferrario, E. Sangiorgi and C. Fiegna, "Fabrication, Simulation, and Experimental Characterization of EWT Solar Cells With Deep Grooved Base Contact," *IEEE Journal of Photovoltaics*, vol. 6, no. 5, pp. 1072-1079, 2016.

[33] A. Fallisch, D. Stüwe, R. Neubauer, D. Wagenmann, R. Keding, J. Nekarda, R. Preu and D. Biro, "Inkjet Structured EWT Silicon Solar Cells with Evaporated Aluminum Metallization and Laser-Fired Contacts," *2010 35th IEEE Photovoltaic Specialists COnference,* pp. 3125-3130, 2010.

[34] P. Spinelli, P. Danzl, N. Guillevin, A. Mewe, S. Sawallich, A. Vlooswijk, B. van de Loo, E. Kessels, M. Nagel and I. Cesar, "High resolution sheet resistance mapping to unveil edge effects in industrial IBC solar cells," *Energy Procedia,* vol. 92, pp. 218-224, 2016.

[35] G. Galbiati, V. D. Mihailetchi, A. Halm, R. Roescu and R. Kopecek, "Results on n-type IBC solar cells using industrial optimized techniques in the fabrication processing," *Energy Procedia,* vol. 8, pp. 421-426, 2011.

[36] T. Buck, R. Kopecek, J. Libal, A. Herguth, K. Peter, I. Röver, K. Wambach and B. Geerligs, "Industrial Screen Printed n-type Silicon Solar Cells with Front Boron Emitter and Efficiencies Exceeding 17%," 2006. [Online]. Available: https://www.researchgate.net/publication/268059463_Industrial_screen_printed_n-type_silicon_solar_cells_with_front_boron_emitter_and_efficiencies_exceeding_17. [Accessed 05 03 2019].

[37] P.-Y. Hsin, Y.-W. Peng and J.-Y. Gan, "High-Efficiency Screen-Printed p-Si Interdigitated Back Contact Cells: Fabrication and Analytical Characterization," *IEEE Journal of Photovoltaics,* vol. 7, no. 5, pp. 1284-1291, 2017.

[38] A. Ingenito, O. Isabella and M. Zeman, "Simplified process for high efficiency,self-aligned IBC c-Si solar cells combining ion implantation and epitaxial growth: Design and fabrication," *Solar Energy Materials & Solar Cells,* vol. 157, pp. 354-365, 2016.

[39] M. G. Kang, J.-H. Lee, H. Boo, S. J. Tark, H. C. Hwang, W. J. Hwang, H. O. Kang and D. Kim, "Effects of annealing on ion-implanted Si for interdigitated back contact solar cell," *Current Applied Physics,* vol. 12, pp. 1615-1618, 2012.

[40] G. Masmitja, P. Ortega, I. Martín, G. López, C. Voz and R. Alcubilla, "IBC c-Si(n) solar cells based on laser doping processing for selective emitter and base contact formation," *Energy Procedia,* vol. 92, pp. 956-961, 2016.

[41] Y. Chen, Y. Yang, G. Xu, J. K. Marmon, Z. Feng and H. Shen, "Optimization of micron size passivated contact and doping level for high efficiency interdigitated back contact solar cells," *Solar Energy,* vol. 178, pp. 308-313, 2019.

[42] J. Salami, B. Cruz and A. Shaikh, "Diffusion Paste Development for Printable IBC and Bifacial Silicon Solar Cells," *2006 IEEE 4th World Conference on Photovoltaic Energy Conference,* pp. 1323-1325, 2006.

[43] C. Hollemann, F. Haase, S. Schäfer, J. Krügener, R. Brendel and R. Peibst, "26.1%- efficient POLO- IBC cells: Quantification of electrical and optical loss mechanisms," *Progress in Photovoltaics,* pp. 1-9, 2019.

[44] D. D. Smith, G. Reich, M. Baldrias, M. Reich, N. Boitnott and G. Bunea, "Silicon Solar Cells with total area efficiency above 25%," *IEEE,* pp. 3351-3355, 2016.

[45] E. Franklin, K. Fong, K. McIntosh, A. Fell, A. Blakers, T. Kho, D. Walter, D. Wang, N. Zin, M. Stocks, E.-C. Wang, N. Grant, Y. Wan, Y. Yang, X. Zhang, Z. Feng and P. J. Verlinden, "Design, fabrication and characterisation of a 24.4% efficient interdigitated back contact solar cell," *Progress in Photovoltaics: Research and Applications,* vol. 24, pp. 411-427, 2016.

[46] S. Singh, B. O'Sullivan, M. R. Payo, A. U. De Castro, M. Debucquoy, J. Szlufcik and J. Poortmans, "Process Development on Photolithography Free IBC Solar Cells," in *29th European Photovoltaic Solar Energy Conference and Exhibition*, Amsterdam, 2014.

[47] "Thin Film - Solar Panel Photovoltaic," 20 12 2013. [Online]. Available: http://solarpanelsphotovoltaic.net/types-of-solar-panels/thin-film/. [Accessed 30 11 2019].

[48] NREL, "NREL - Best Research-Cell Efficiencies," 06 11 2019. [Online]. Available: https://www.nrel.gov/pv/assets/pdfs/best-research-cell-efficiencies.20191106.pdf. [Accessed 06 12 2019].

[49] M. Punčochář, "Chemical Equations Online," [Online]. Available: https://chemequations.com/en/?s=Si+%2B+KOH+%2B+H2O+%3D+K2SiO3+%2B+H2. [Accessed 05 12 2019].

[50] "MicroChemicals," [Online]. Available: https://www.microchemicals.eu/technical_information/silicon_etching.pdf. [Accessed 05 12 2019].

[51] R. Monna, V. Sanzone, J. Diaz and Y. Veschetti, "Influence of the BCl3 diffusion process homogeneity on the surface passivation of n-type PERT solar cells," *Energy Procedia*, vol. 92, pp. 479-485, 2016.

[52] E. Arai, H. Nakamura and Y. Terunuma, "Interface Reactions of B 2 O 3 - Si System and Boron Diffusion into Silicon," *Journal of The Electrochemical Society*, vol. 120, no. 7, pp. 980-987, 1973.

[53] S. W. Jones, "Diffusion in Silicon," in *Silicon Integrated Circuit Process Technology*, IC Knowledge, 2000, pp. 1-68.

[54] G. Tuttle, "Diffusion," [Online]. Available: http://tuttle.merc.iastate.edu/ee432/topics/doping/diffusion_details.pdf. [Accessed 19 12 2019].

[55] S. Wolf and R. N. Tauber, Silicon Processing for the VLSI Era, California: Lattice Press, 1980.

[56] J. D. Plummer, M. D. Deal and P. B. Griffin, Silicon VLSI Technology, Upper Saddle River, New Jersey: Prentice Hall, 2000.

[57] D. K. Schroder, Semiconductor Material and Device Characterization, Hoboken, New Jersey: John Wiley & Sons, Inc., 2006.

[58] R. A. Sinton, A. Cuevas and M. Stuckings, "Quasi-steady-state photoconductance, a new method for solar cell material and device characterization," *IEEE*, pp. 457-460, 1996.

[59] "Sheet Resistance: A Guide to Theory," Ossila, [Online]. Available: https://www.ossila.com/pages/sheet-resistance-theory. [Accessed 03 July 2019].

[60] G. Scardera, D. Inns, G. Wang, S. Dugan, J. Dee, T. Dang, K. Bendimerad, F. Lemmi and H. Antoniadis, "All-screen-printed dopant paste interdigitated back contact solar cell," *Energy Procedia,* vol. 77, pp. 271-278, 2015.

[61] G. D. Robertson, Jr., D. M. Mason and W. H. Corcoran, "The Kinematics of the Thermal Decomposition of Nitric Acid in the Liquid Phase," *Journal of Physical Chemistry,* vol. 59, no. 8, pp. 683-690, 1955.

[62] R. Brendel and B. Lim, "ISFH," 29 January 2018. [Online]. Available: https://isfh.de/wp-content/uploads/2018/02/180129_ISFH_Brendel_TUV_ModTechForum_2018.pdf. [Accessed 28 May 2019].

[63] M. A. Green, Y. Hishikawa, E. D. Dunlop, D. H. Levi, J. Hohl-Ebinger, M. Yoshita and A. W. Ho-Baillie, "Solar cell efficiency tables (Version 54)," *Progress in Photovoltaics: Research and Applications,* vol. 27, no. 7, pp. 565-575, 2019.

[64] T. Fellmeth, M. Menkoe, F. Clement, D. Biro and R. Preu, "Highly efficient industrially feasible metal wrap through (MWT) silicon solar cells," *Solar Energy Materials & Solar Cells,* vol. 94, pp. 1996-2001, 2010.

[65] C. Honsberg and S. Bowden, "PVEducation," [Online]. Available: https://www.pveducation.org/pvcdrom/detailed-balance. [Accessed 2019 December 17].

INDEX

"Scientia Dux Vitae Certissimus"

M. Kemal ATATÜRK (1881-193∞)